The Nucleon-Nucleon Interaction in Chiral Effective Field Theory up to 5th Order (N4LO)

A Dissertation
Presented in Partial Fulfilment of the Requirements for the
Degree of Doctorate of Philosophy
with a
Major in Physics
in the
College of Graduate Studies
University of Idaho
by
Yevgen O. Nosyk

Major Professor: Ruprecht Machleidt, Ph.D.
Committee Members: Francesca Sammarruca, Ph.D.; Bernhard Stumpf, Ph.D.;
Lyudmyla Barannyk, Ph.D.
Department Administrator: Ray von Wandruszka, Ph. D.

August 2017

Authorization to Submit Dissertation

This dissertation of Yevgen O. Nosyk, submitted for the degree of Doctorate of Philosophy with a major in Physics and titled "The Nucleon-Nucleon Interaction in Chiral Effective Field Theory up to 5th Order (N4LO)," has been reviewed in final form. Permission, as indicated by the signatures and dates given below, is now granted to submit final copies to the College of Graduate Studies for approval.

Major Professor: ______________________________Date______________
Ruprecht Machleidt, Ph.D.

Committee
Members: ______________________________Date______________
Francesca Sammarruca, Ph.D.

______________________________Date______________
Bernhard Stumpf, Ph.D.

______________________________Date______________
Lyudmyla Barannyk, Ph.D.

Department
Administrator: ______________________________Date______________
Ray von Wandruszka, Ph.D.

Abstract

While attempts to solve the equations of Quantum Chromodynamics (QCD) numerically in the low energy limit are increasingly successful (”lattice QCD”), Chiral Effective Field Theory (ChEFT) remains a potent alternative method for deriving nuclear force potentials. Previous calculations within framework of ChEFT up to 4th order (next-to-next-to-next-to-leading order, N^3LO) show generally good agreement with experiment. However, some persistent problems with N^3LO potentials as well as the question of order-by-order convergence of ChEFT require calculations up to higher orders. In this work, I present calculations of pion exchange contributions to nucleon-nucleon potentials up to 5th and 6th order (N^4LO and N^5LO). N^4LO calculations solve some of the previous persistent problems and improve the agreement with nucleon-nucleon (NN) scattering experiments in peripheral partial waves. N^5LO contributions further improve the agreement with experiment and also turn out to be smaller compared to N^4LO, thus showing the trend for convergence. Finally, I present the full NN potential at N^4LO, which shows excellent agreement with experimental data in all partial waves and can be applied further in nuclear structure calculations. Since a modified power counting scheme is used for N^4LO potential, full NN potentials at NLO, NNLO and N^3LO are also recalculated using the modified scheme. This allows for systematic truncation error estimation when applying potentials to calculations of nuclear structure and reactions.

Acknowledgements

I am thankful to my my academic advisor, R. Machleidt, as well as my committee members, F. Sammarruca, B. Stumpf, L. Barannyk, and our research group collaborators N. Kaiser and D. R. Entem. I am also thankful to Physics Department for supporting my graduate studies academically and financially. Finally, my work with R. Machleidt was supported in part by a grant from the U.S. Department of Energy.

Table of Contents

List of Tables

List of Figures

CHAPTER 1
Introduction

The quest for a practically feasible, and yet fundamental, theory of hadronic interactions at low energy (where QCD is non-perturbative) has spanned several decades. At the present time, there exists a general consensus that chiral effective field theory (chiral EFT) may provide the best answer to the quest. By its nature, chiral EFT is a model-independent approach with firm roots in QCD, due to the fact that interactions are subjected to the constraints of the broken chiral symmetry of low-energy QCD. Moreover, the approach is systematic in the sense that the various contributions to a particular dynamical process can be arranged as an expansion in terms of powers of a suitable "parameter", $(Q/\Lambda_\chi)^\nu$. Here, Q is the soft scale of the theory, represented by a typical external momentum of the nucleon or pion, or a pion mass; Λ_χ is the chiral symmetry breaking scale (≈ 1 GeV, hard scale). Recent comprehensive reviews on the subject can be found in Refs. [1, 2].

In its early stages, chiral perturbation theory (ChPT) was applied mostly to $\pi\pi$ [3] and πN [4] dynamics, because, due to the Goldstone-boson nature of the pion, these are the most natural scenarios for a perturbative expansion to exist. In the meantime, though, chiral EFT has been applied in nucleonic systems by numerous groups [1, 2, 5, 6, 7, 8, 9, 10, 11, 12, 13, 14, 15, 16, 17, 18, 19, 20, 21, 22, 23, 24, 25, 26]. Derivations of the nucleon-nucleon (NN) interaction up to fourth order (next-to-next-to-next-to-leading order, N^{3}LO) can be found in Refs. [7, 9, 10, 12, 13, 15], with quantitative NN potentials making their appearance in the early 2000's [16, 17].

Since then, a wealth of applications of N^{3}LO NN potentials together with chiral three-nucleon forces (3NFs) have been reported. These investigations include few-nucleon reactions, structure of light- and medium-mass nuclei, and infinite matter. Although satisfactory predictions have been obtained in many cases, persistent problems continue to pose serious challenges, such as the well-known 'A_y puzzle' of nucleon-deuteron scattering [27]. Naturally, one would invoke 3NFs as the most likely mechanism to solve this problem. Unfortunately, the chiral 3NF at NNLO does only very little to improve the situation with nucleon-deuteron scattering [28, 29], while inclusion of the N^{3}LO 3NF produces an effect in the wrong direction [30]. The next step is then to proceed systematically in the expansion, namely to look at N^{4}LO (or fifth order). This order is interesting for diverse reasons. From studies of some of the 3NF topologies at N^{4}LO [31, 32], we know that a complete set of isospin-spin-momentum 3NF structures (a total of 20) are present at this order [33] and that contributions can be of substantial size. Even more promising, at this order a new set of 3NF contact interactions appears, which has recently been derived by the Pisa group [34]. Contact terms are relatively easy to work with and, most importantly, come with free coefficients and, thus, provide larger flexibility and a great likelihood to solve persistent problems such as the A_y puzzle as well as other issues (like, the "radius problem" [35] and the overbinding of intermediate-mass nuclei [36]).

A principle of all EFTs is that, for meaningful predictions, it is necessary to include *all* contributions that appear at the order at which the calculation is conducted. Thus, when nuclear structure problems require for their solution the inclusion of 3NFs at N^{4}LO, then also the two-nucleon force involved in the calculation has to be of order N^{4}LO. This is the main motivation for this study. We derived the N^{4}LO two-pion exchange (2PE) and three-pion exchange (3PE) contributions to the NN interaction and tested them in peripheral partial waves [37]. Then, we developed a complete N^{4}LO NN potentials that also include the lower partial waves which receive contributions from contact interactions [38].

It should be also mentioned that pion-exchange contributions are the only ones responsible for long-range force and the πN coupling constants can be determined independently from πN scattering experiments. Therefore, predictions for NN scattering results in peripheral partial waves is a crucial test of how well the theory works, since behavior of peripheral waves is determined by the long-range force.

In Ref. [37], we also demonstrated that the next-to-next-to-leading order (NNLO), the N^{3}LO, and the N^{4}LO contributions to the NN interaction are all of about the same size, thus, not showing much of a trend towards convergence. Therefore, in Ref. [39] we calculated the N^{5}LO (sixth order) contribution which, indeed, turned out to be small. The latter result implies that the NN interaction is essentially converged at N^{4}LO. This adds to the significance of order N^{4}LO.

Besides the above, we are faced with another set of convergence issues: The convergence of the predictions for the properties of nuclear few- and many-body systems, in which also chiral many-body forces are involved. To investigate these issues, one needs (besides those many-body forces) NN potentials at all orders of chiral EFT, ranging from leading order (LO) to N^{4}LO, and constructed consistently, i. e., using the same power-counting scheme, consistent LECs, etc..

For that reason, we present in this work NN potentials through five orders from LO to N^{4}LO, constructed with the above-stated consistencies and with a reproduction of the NN data of the maximum quality possible at the respective orders. These potentials will allow for systematic investigations of nuclear few- and many-body systems with clear implications for convergence and uncertainty quantifications (truncation errors).

CHAPTER 2

Overview of Chiral EFT formalism

2.1 An effective field theory of low energy QCD

Our current fundamental theory of Strong interaction is Quantum Chromodynamics (QCD), which is a part of Standard model of Particle Physics. According to this theory, Strong interactions are interactions between color-charged quarks and gluons. Certain mathematical features of QCD result in interaction between colored objects being weak at short distances, which corresponds to high energies of interaction; conversely, interaction is strong at long distances ($\gtrsim 1$ fm), i.e. at low energies. The latter results in confinement of colored quarks into colorless composite particles, hadrons. Thus, within the framework of QCD, the force between nucleons is a residual strong interaction between colored objects within nucleons. This is qualitatively similar to van der Waals force being a residual electromagnetic interaction between protons and electrons of neutral atoms or molecules.

Since the Strong interaction is weak at high energies, the same perturbative analytical methods work here as for Quantum Electrodynamics. However, at low energies typical of nuclear physics QCD becomes non-perturbative. Therefore, deriving the nuclear force from QCD becomes a very complex problem.

One approach here would be solving equations of QCD numerically, which is known as lattice QCD. Recent attempts to use this method are increasingly successful. But it is too computationally expensive. And so far only systems of few quarks were calculated. For typical nuclear physics applications, a more efficient approach is needed.

Such an approach is offered by effective field theory (EFT). Based upon Weinberg's 'folk theorem' [40], we summarize the following prescription to construct the theory:

1. Identify the soft and hard scales, and the degrees of freedom appropriate for (low-energy) nuclear physics.

2. Identify the relevant symmetries of low-energy QCD and investigate if and how they are broken.

3. Construct the most general Lagrangian consistent with those symmetries and symmetry breakings.

4. Design an organizational scheme that can distinguish between more and less important con-

tributions: a low-momentum expansion.

5. Guided by the expansion, calculate Feynman diagrams for the problem under consideration to the desired accuracy.

To deal with first item on the list, we can point out that there exists a large gap between the masses of the pions and the masses of the vector mesons, like $\rho(770)$ and $\omega(782)$. Thus, it is natural to assume that the pion mass sets the soft scale, $Q \sim m_\pi$, and the rho mass the hard scale, $\Lambda_\chi \sim m_\rho$, also known as the chiral symmetry breaking scale. This is suggestive of considering an expansion in terms of the soft scale over the hard scale, Q/Λ_χ. As for the relevant degrees of freedom, it is reasonable to pick colorless nucleons and pions as low energy degrees of freedom instead of quarks and gluons.

It may be helpful to mention how this situation is qualitatively similar to the approach for deriving Lennard-Jones potential used to model van der Waals forces. Strictly speaking, one should derive the force between the gas particles by considering the motion of individual electrons and nuclei of the atoms. However, this is not a very trivial task. On the other hand, around room temperature (low energies), molecules and atoms are usually not ionized and their electron shells are not excited. The electron excitation energy of the molecule can be thought of as hard scale here. Therefore, rather than thinking in terms of charged electrons and nuclei, it is more convenient to think in terms of neutral gas particles, i.e. effective degrees of freedom. Then, the long range attration term $\sim 1/r^6$ of the Lennard-Jones potential is easily derived as a force between induced dipole moments of the gas particles. The artificial $\sim 1/r^{12}$ term is introduced to model short range repulsion between overlapping electron shells of the atoms. Similarly, the long range force between nucleons is successfully derived in Chiral EFT in terms of nucleons exchanging pions. Short range force due to overlap of nucleons is taken care of by introducing nucleon-nucleon contact terms.

The second item on the list above requires our EFT to observe all relevant symmetries of QCD. In particular, chiral symmetry (and its breaking) is of great importance here. This provides the firm link with underlying QCD and ensures that Chiral EFT is not just another phenomenology.

It should be pointed out, that the first successful theory of nuclear force by Yukawa also involved nucleons exchanging pions. However, certain multi-pion-exchange diagrams caused problems in the theory. Chiral symmetry that transpired in QCD provides additional constraints and makes the contributions of these diagrams reasonable.

We proceed to deal with the last three items on the list in subsequent chapters.

2.2 Expansion of the NN potential

2.2.1 Effective Langrangians

In the Δ-less version of chiral EFT, which is the one we are pursuing here, the relevant degrees of freedom are pions (Goldstone bosons) and nucleons. Since the interactions of Goldstone bosons must vanish at zero momentum transfer and in the chiral limit ($m_\pi \to 0$), the low-energy expansion of the effective Lagrangian is arranged in powers of derivatives and pion masses. This effective Lagrangian is subdivided into the following pieces,

$$\mathcal{L}_{\text{eff}} = \mathcal{L}_{\pi\pi} + \mathcal{L}_{\pi N} + \mathcal{L}_{NN} + \ \ldots\ , \tag{2.1}$$

where $\mathcal{L}_{\pi\pi}$ deals with the dynamics among pions, $\mathcal{L}_{\pi N}$ describes the interaction between pions and a nucleon, and $\mathcal{L}_{NN}$ contains two-nucleon contact interactions which consist of four nucleon-fields (four nucleon legs) and no meson fields. The ellipsis stands for terms that involve two nucleons plus pions and three or more nucleons with or without pions, relevant for nuclear many-body forces. The individual Lagrangians are organized in terms of increasing orders:

$$\mathcal{L}_{\pi\pi} = \mathcal{L}^{(2)}_{\pi\pi} + \mathcal{L}^{(4)}_{\pi\pi} + \ldots\ , \tag{2.2}$$

$$\mathcal{L}_{\pi N} = \mathcal{L}^{(1)}_{\pi N} + \mathcal{L}^{(2)}_{\pi N} + \mathcal{L}^{(3)}_{\pi N} + \mathcal{L}^{(4)}_{\pi N} + \ldots, \tag{2.3}$$

$$\mathcal{L}_{NN} = \mathcal{L}^{(0)}_{NN} + \mathcal{L}^{(2)}_{NN} + \mathcal{L}^{(4)}_{NN} + \ldots\ , \tag{2.4}$$

where the superscript refers to the number of derivatives or pion mass insertions (chiral dimension) and the ellipses stand for terms of higher dimensions. We use the heavy-baryon formulation of the Lagrangians, the explicit expressions of which can be found in Refs. [1, 31].

2.2.2 Power counting

Based upon the above Langrangians, an infinite number of diagrams contributing to the interactions among nucleons can be drawn. Nuclear potentials are defined by the irreducible types of these graphs. By definition, an irreducible graph is a diagram that cannot be separated into two by cutting only nucleon lines. These graphs are then analyzed in terms of powers of small external momenta over the large scale: $(Q/\Lambda_\chi)^\nu$, where Q is generic for a momentum (nucleon three-momentum or pion four-momentum) or a pion mass and $\Lambda_\chi \sim 1$ GeV is the chiral symmetry breaking scale (hardronic scale, hard scale). Determining the power ν has become know as power counting.

Following the Feynman rules of covariant perturbation theory, a nucleon propagator is Q^{-1}, a pion propagator Q^{-2}, each derivative in any interaction is Q, and each four-momentum integration Q^4. This is also known as naive dimensional analysis or Weinberg counting.

Since we use the heavy-baryon formalism, we encounter terms which include factors of Q/M_N, where M_N denotes the nucleon mass. We count the order of such terms by the rule $Q/M_N \sim (Q/\Lambda_\chi)^2$, for reasons explained in Ref. [5].

Applying some topological identities, one obtains for the power of a connected irreducible diagram involving A nucleons [1, 5]

$$\nu = -2 + 2A - 2C + 2L + \sum_i \Delta_i \,, \tag{2.5}$$

with

$$\Delta_i \equiv d_i + \frac{n_i}{2} - 2 \,, \tag{2.6}$$

where L denotes the number of loops in the diagram; d_i is the number of derivatives or pion-mass insertions and n_i the number of nucleon fields (nucleon legs) involved in vertex i; the sum runs over all vertexes i contained in the connected diagram under consideration. Note that $\Delta_i \geq 0$ for all interactions allowed by chiral symmetry.

An important observation from power counting is that the powers are bounded from below and, specifically, $\nu \geq 0$. This fact is crucial for the convergence of the low-momentum expansion.

Furthermore, the power formula Eq. (2.5) allows to predict the leading orders of connected multi-nucleon forces. Consider a m-nucleon irreducibly connected diagram (m-nucleon force) in an A-nucleon system ($m \leq A$). The number of separately connected pieces is $C = A - m + 1$. Inserting this into Eq. (2.5) together with $L = 0$ and $\sum_i \Delta_i = 0$ yields $\nu = 2m - 4$. Thus, two-nucleon forces ($m = 2$) appear at $\nu = 0$, three-nucleon forces ($m = 3$) at $\nu = 2$ (but they happen to cancel at that order), and four-nucleon forces at $\nu = 4$ (they don't cancel).

For an irreducible NN diagram ($A = 2$, $C = 1$), the power formula collapses to the very simple expression

$$\nu = 2L + \sum_i \Delta_i \,. \tag{2.7}$$

In summary, the chief point of the ChPT expansion of the potential is that, at a given order

ν, there exists only a finite number of graphs. This is what makes the theory calculable. The expression $(Q/\Lambda_\chi)^{\nu+1}$ provides an estimate of the relative size of the contributions left out and, thus, of the uncertainty at order ν. The ability to calculate observables (in principle) to any degree of accuracy gives the theory its predictive power.

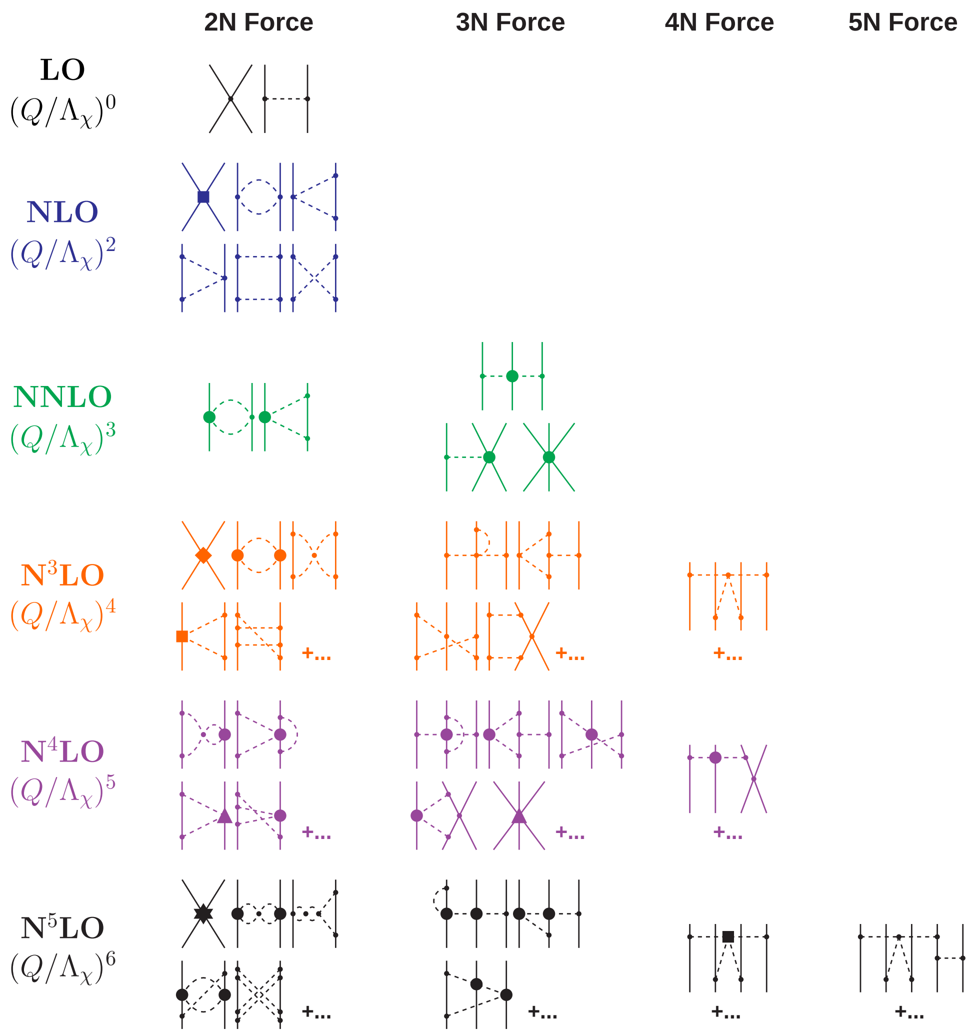

Figure 2.1: Hierarchy of nuclear forces in ChPT. Solid lines represent nucleons and dashed lines pions. Small dots, large solid dots, solid squares, triangles, diamonds, and stars denote vertexes of index Δ_i = 0, 1, 2, 3, 4, and 6, respectively. Further explanations are given in the text.

Chiral perturbation theory and power counting imply that nuclear forces evolve as a hierarchy controlled by the power ν, see Fig. 2.1 for an overview. In what follows, we will focus on the two-nucleon force (2NF).

2.2.3 The long-range NN potential

The long-range part of the NN potential is built up from pion exchanges, which are ruled by chiral symmetry. The various pion-exchange contributions may be analyzed according to the number of pions being exchanged between the two nucleons:

$$V = V_{1\pi} + V_{2\pi} + V_{3\pi} + \ldots , \tag{2.8}$$

where the meaning of the subscripts is obvious and the ellipsis represents 4π and higher pion exchanges. For each of the above terms, we have a low-momentum expansion:

$$\begin{aligned}
V_{1\pi} &= V_{1\pi}^{(0)} + V_{1\pi}^{(2)} + V_{1\pi}^{(3)} + V_{1\pi}^{(4)} + V_{1\pi}^{(5)} + \ldots && (2.9)\\
V_{2\pi} &= V_{2\pi}^{(2)} + V_{2\pi}^{(3)} + V_{2\pi}^{(4)} + V_{2\pi}^{(5)} + \ldots && (2.10)\\
V_{3\pi} &= V_{3\pi}^{(4)} + V_{3\pi}^{(5)} + \ldots , && (2.11)
\end{aligned}$$

where the superscript denotes the order ν of the expansion.

Order by order, the long-range NN potential builds up as follows:

$$\begin{aligned}
V_{\mathrm{LO}} &\equiv V^{(0)} = V_{1\pi}^{(0)} && (2.12)\\
V_{\mathrm{NLO}} &\equiv V^{(2)} = V_{\mathrm{LO}} + V_{1\pi}^{(2)} + V_{2\pi}^{(2)} && (2.13)\\
V_{\mathrm{NNLO}} &\equiv V^{(3)} = V_{\mathrm{NLO}} + V_{1\pi}^{(3)} + V_{2\pi}^{(3)} && (2.14)\\
V_{\mathrm{N3LO}} &\equiv V^{(4)} = V_{\mathrm{NNLO}} + V_{1\pi}^{(4)} + V_{2\pi}^{(4)} + V_{3\pi}^{(4)} && (2.15)\\
V_{\mathrm{N4LO}} &\equiv V^{(5)} = V_{\mathrm{N3LO}} + V_{1\pi}^{(5)} + V_{2\pi}^{(5)} + V_{3\pi}^{(5)} && (2.16)
\end{aligned}$$

where LO stands for leading order, NLO for next-to-leading order, etc..

General form of pion exchanges

At leading order, there is only the 1π-exchange contribution (see appendix A.1 for details). Two-pion exchange starts at NLO and continues through all higher orders. In Fig. 2.1, the corresponding diagrams are show completely up to NNLO. Beyond that order, the number of diagrams increases so dramatically that we show only a few symbolic graphs. The situation is similar for the 3PE contributions which start at N^{3}LO. Also the mathematical formulas are getting increasingly involved. Note, that pion-exchange contributions at LO through N^{3}LO have been derived in previous works, and are not the subject of this study. We omit them from the main part of the paper. A complete collection of all formulas concerning the 1PE, 2PE and 3PE contributions through all orders from LO to N^{3}LO is given in Appendix A, as summarized in Ref. [37]. N^{4}LO and N^{5}LO contributions are presented further in Chapters 3 and 4. In all 2PE and 3PE contributions, we use the average pion mass, $\bar{m}_\pi = 138.039$ MeV. The charge-dependence caused by pion-mass splitting in 2PE has been found to be negligible in all partial waves with $L > 0$ [41]. The small effect in $^1S_0$ is absorbed into the charge-dependence of the zeroth-order contact parameter $\widetilde{C}_{^1S_0}$, see below.

The results in Chapters 3 and 4 will be stated in terms of contributions to the momentum-space NN amplitudes in the center-of-mass system (CMS), which arise from the following general decomposition:

$$
\begin{aligned}
V(\vec{p}\,', \vec{p}) \; = \;& V_C \; + \boldsymbol{\tau}_1 \cdot \boldsymbol{\tau}_2 \, W_C \\
& + [\, V_S \; + \boldsymbol{\tau}_1 \cdot \boldsymbol{\tau}_2 \, W_S \;\,] \; \vec{\sigma}_1 \cdot \vec{\sigma}_2 \\
+ \;& [\, V_{LS} + \boldsymbol{\tau}_1 \cdot \boldsymbol{\tau}_2 \, W_{LS}] \left(-i \vec{S} \cdot (\vec{q} \times \vec{k}) \right) \\
+ \;& [\, V_T \; + \boldsymbol{\tau}_1 \cdot \boldsymbol{\tau}_2 \, W_T \;\,] \; \vec{\sigma}_1 \cdot \vec{q} \, \vec{\sigma}_2 \cdot \vec{q} \\
+ \;& [\, V_{\sigma L} + \boldsymbol{\tau}_1 \cdot \boldsymbol{\tau}_2 \, W_{\sigma L} \,] \; \vec{\sigma}_1 \cdot (\vec{q} \times \vec{k}\,) \; \vec{\sigma}_2 \cdot (\vec{q} \times \vec{k}\,) \, ,
\end{aligned}
\tag{2.17}
$$

where $\vec{p}\,'$ and $\vec{p}$ denote the final and initial nucleon momenta in the CMS, respectively. Moreover, $\vec{q} = \vec{p}\,' - \vec{p}$ is the momentum transfer, $\vec{k} = (\vec{p}\,' + \vec{p})/2$ the average momentum, and $\vec{S} = (\vec{\sigma}_1 + \vec{\sigma}_2)/2$ the total spin, with $\vec{\sigma}_{1,2}$ and $\boldsymbol{\tau}_{1,2}$ the spin and isospin operators, of nucleon 1 and 2, respectively. For on-shell scattering, V_α and W_α ($\alpha = C, S, LS, T, \sigma L$) can be expressed as functions of $q = |\vec{q}\,|$ and $p = |\vec{p}\,'| = |\vec{p}\,|$, only. Note that the one-pion exchange contribution in Eq. (2.9) is of the form $W_T^{(1\pi)} = -(g_{\pi N}/2M_N)^2(m_\pi^2 + q^2)^{-1}$ with physical values of the coupling constant $g_{\pi N}$ and nucleon and pion masses M_N and m_π. This expression fixes at the same time our sign-convention for $V(\vec{p}\,', \vec{p})$.

We consider loop contributions in terms of their spectral functions, from which the momentum-space amplitudes $V_\alpha(q)$ and $W_\alpha(q)$ are obtained via the subtracted dispersion integrals:

$$
\begin{aligned}
V_{C,S}(q) &= -\frac{2q^6}{\pi} \int_{nm_\pi}^{\tilde{\Lambda}} d\mu \, \frac{\mathrm{Im}\, V_{C,S}(i\mu)}{\mu^5(\mu^2 + q^2)} \, , \\
V_{T,LS}(q) &= \frac{2q^4}{\pi} \int_{nm_\pi}^{\tilde{\Lambda}} d\mu \, \frac{\mathrm{Im}\, V_{T,LS}(i\mu)}{\mu^3(\mu^2 + q^2)} \, ,
\end{aligned}
\tag{2.18}
$$

Table 2.1: The πN LECs as determined in the Roy-Steiner-equation analysis of πN scattering conducted in Ref. [44]. The given orders of the chiral expansion refer to the NN system. Note that the orders, at which the LECs are extracted from the πN system, are always lower by one order as compared of the NN system in which the LECs are applied. The c_i, $\bar{d}_i$, and $\bar{e}_i$ are the LECs of the second, third, and fourth order πN Lagrangian [31] and are in units of GeV^{-1}, GeV^{-2}, and GeV^{-3}, respectively. The uncertainties in the last digits are given in parentheses after the values.

	NNLO	N^{3}LO	N^{4}LO
c_1	–0.74(2)	–1.07(2)	–1.10(3)
c_2	—	3.20(3)	3.57(4)
c_3	–3.61(5)	–5.32(5)	–5.54(6)
c_4	2.44(3)	3.56(3)	4.17(4)
$\bar{d}_1 + \bar{d}_2$	—	1.04(6)	6.18(8)
$\bar{d}_3$	—	–0.48(2)	–8.91(9)
$\bar{d}_5$	—	0.14(5)	0.86(5)
$\bar{d}_{14} - \bar{d}_{15}$	—	–1.90(6)	–12.18(12)
$\bar{e}_{14}$	—	—	1.18(4)
$\bar{e}_{17}$	—	—	–0.18(6)

up to N^{4}LO and

$$\begin{aligned} V_{C,S}(q) &= \frac{2q^8}{\pi} \int_{nm_\pi}^{\tilde{\Lambda}} d\mu \, \frac{\operatorname{Im} V_{C,S}(i\mu)}{\mu^7(\mu^2+q^2)} \,, \\ V_T(q) &= -\frac{2q^6}{\pi} \int_{nm_\pi}^{\tilde{\Lambda}} d\mu \, \frac{\operatorname{Im} V_T(i\mu)}{\mu^5(\mu^2+q^2)} \,, \end{aligned} \tag{2.19}$$

at N^{5}LO. Similar equations are used for $W_{C,S,T,LS}$. The thresholds are given by $n = 2$ for two-pion exchange and $n = 3$ for three-pion exchange. For $\tilde{\Lambda} \to \infty$ the above dispersion integrals yield the results of dimensional regularization, while for finite $\tilde{\Lambda} \geq nm_\pi$ we employ the method known as spectral-function regularization (SFR) [42]. The purpose of the finite scale $\tilde{\Lambda}$ is to constrain the imaginary parts to the low-momentum region where chiral effective field theory is applicable. Thus, a reasonable choice for $\tilde{\Lambda}$ is to keep it below the masses of the vector mesons $\rho(770)$ and $\omega(782)$, but above the $f_0(500)$ [also know as $\sigma(500)$] [43]. This suggests that the region 600-700 MeV is appropriate for $\tilde{\Lambda}$. Consequently, we use $\tilde{\Lambda} = 650$ MeV in all orders, except for N^{4}LO where we apply 700 MeV. (Note, that a slightly different cutoff range is used for the study of peripheral partial waves, as explained in sections 5.3 and 5.4.)

Table 2.2: Basic constants used throughout this work [43].

Quantity	Value
Axial-vector coupling constant g_A	1.29
Pion-decay constant f_π	92.4 MeV
Charged-pion mass $m_{\pi^\pm}$	139.5702 MeV
Neutral-pion mass m_{π^0}	134.9766 MeV
Average pion-mass $\bar{m}_\pi$	138.0390 MeV
Proton mass M_p	938.2720 MeV
Neutron mass M_n	939.5654 MeV
Average nucleon-mass $\bar{M}_N$	938.9183 MeV

The pion-nucleon low-energy constants

Chiral symmetry establishes a link between the dynamics in the πN-system and the NN-system through common low-energy constants. Therefore, consistency requires that we use the LECs for subleading πN-couplings as determined in analysis of low-energy πN-scattering. Over the years, there have been many such determinations of questionable reliability. Fortunately, that has changed recently with the analysis by Hoferichter and Ruiz de Elvira *et al.* [44], in which the Roy-Steiner (RS) equations are applied. The RS equations are a set of coupled partial-wave dispersion relations constraint by analyticity, unitarity, and crossing symmetry. In the work of Ref. [44], they are used to extract the LECs from the subthreshold point in πN scattering instead of the physical region. This is the preferred method for LECs to be applied in chiral potentials where, e. g., a one-loop πN amplitude leads to a two-loop contribution in NN. Such diagrams are best evaluated by means of Cutkosky rules [12, 37, 39]. The πN amplitude that enters the dispersion integrals is weighted much closer to subthreshold kinematics than to the threshold point. The LECs determined in Ref. [44] carry very small uncertainties (cf. Table 2.1) for, essentially, two reasons: first, because of the constraints built into the RS equations; second, because of the use of the high-accuracy πN scattering lengths extracted from pionic atoms. In fact, the uncertainties are so small that they are negligible for our purposes. This makes the variation of the πN LECs in NN potential construction obsolete and reduces the error budget in applications of these potentials. For the potentials constructed in this paper, the central values of Table 2.1 are applied.

Other constants

Finally, we also summarize other constants related to pion-nucleon interaction in Table 2.2.

2.2.4 The short-range NN potential

The short-range NN potential is described by contributions of the contact type, which are constrained by parity, time-reversal, and the usual invariances, but not by chiral symmetry. Terms that include a factor $\boldsymbol{\tau}_1 \cdot \boldsymbol{\tau}_2$ (owing to isospin invariance) can be left out due to Fierz ambiguity. Because of parity and time-reversal only even powers of momentum are allowed. Thus, the expansion of the contact potential is formally written as

$$V_{\rm ct} = V_{\rm ct}^{(0)} + V_{\rm ct}^{(2)} + V_{\rm ct}^{(4)} + V_{\rm ct}^{(6)} + \dots \;, \tag{2.20}$$

where the superscript denotes the power or order.

The zeroth order (leading order, LO) contact potential is given by

$$V_{\rm ct}^{(0)}(\vec{p}\,', \vec{p}) = C_S + C_T\, \vec{\sigma}_1 \cdot \vec{\sigma}_2 \tag{2.21}$$

and, in terms of partial waves,

$$\begin{aligned} V_{\rm ct}^{(0)}(^1S_0) &= \widetilde{C}_{^1S_0} = 4\pi\,(C_S - 3\,C_T) & (2.22)\\ V_{\rm ct}^{(0)}(^3S_1) &= \widetilde{C}_{^3S_1} = 4\pi\,(C_S + C_T)\,. & (2.23)\end{aligned}$$

To deal with the isospin breaking in the $^1S_0$ state, we treat $\widetilde{C}_{^1S_0}$ in a charge-dependent way. Thus, we will distinguish between $\widetilde{C}^{\rm pp}_{^1S_0}$, $\widetilde{C}^{\rm np}_{^1S_0}$, and $\widetilde{C}^{\rm nn}_{^1S_0}$.

At second order (NLO), we have

$$\begin{aligned} V_{\rm ct}^{(2)}(\vec{p}\,', \vec{p}) &= C_1\, q^2 + C_2\, k^2 \\ &+ \left(C_3\, q^2 + C_4\, k^2\right) \vec{\sigma}_1 \cdot \vec{\sigma}_2 \\ &+ C_5 \left(-i\vec{S} \cdot (\vec{q} \times \vec{k})\right) \\ &+ C_6\, (\vec{\sigma}_1 \cdot \vec{q})\, (\vec{\sigma}_2 \cdot \vec{q}) \\ &+ C_7\, (\vec{\sigma}_1 \cdot \vec{k})\, (\vec{\sigma}_2 \cdot \vec{k})\,, \end{aligned} \tag{2.24}$$

and partial-wave decomposition yields

$$
\begin{aligned}
V_{\rm ct}^{(2)}(^1S_0) &= C_{^1S_0}(p^2+{p'}^2) \\
V_{\rm ct}^{(2)}(^3P_0) &= C_{^3P_0}\, pp' \\
V_{\rm ct}^{(2)}(^1P_1) &= C_{^1P_1}\, pp' \\
V_{\rm ct}^{(2)}(^3P_1) &= C_{^3P_1}\, pp' \\
V_{\rm ct}^{(2)}(^3S_1) &= C_{^3S_1}(p^2+{p'}^2) \\
V_{\rm ct}^{(2)}(^3S_1-^3D_1) &= C_{^3S_1-^3D_1}p^2 \\
V_{\rm ct}^{(2)}(^3D_1-^3S_1) &= C_{^3S_1-^3D_1}{p'}^2 \\
V_{\rm ct}^{(2)}(^3P_2) &= C_{^3P_2}\, pp'\,.
\end{aligned}
\tag{2.25}
$$

The relationship between the $C_{(2S+1)L_J}$ and the C_i can be found in Ref. [1].

The fourth order (N^{3}LO) contacts are

$$
\begin{aligned}
V_{\rm ct}^{(4)}(\vec{p'},\vec{p}) &= D_1\,q^4 + D_2\,k^4 + D_3\,q^2k^2 + D_4\,(\vec{q}\times\vec{k})^2 \\
&+ \Big(D_5\,q^4 + D_6\,k^4 + D_7\,q^2k^2 + D_8\,(\vec{q}\times\vec{k})^2\Big)\,\vec{\sigma}_1\cdot\vec{\sigma}_2 \\
&+ \left(D_9\,q^2 + D_{10}\,k^2\right)\Big(-i\vec{S}\cdot(\vec{q}\times\vec{k})\Big) \\
&+ \left(D_{11}\,q^2 + D_{12}\,k^2\right)(\vec{\sigma}_1\cdot\vec{q})\,(\vec{\sigma}_2\cdot\vec{q}) \\
&+ \left(D_{13}\,q^2 + D_{14}\,k^2\right)(\vec{\sigma}_1\cdot\vec{k})\,(\vec{\sigma}_2\cdot\vec{k}) \\
&+ D_{15}\Big(\vec{\sigma}_1\cdot(\vec{q}\times\vec{k})\;\vec{\sigma}_2\cdot(\vec{q}\times\vec{k})\Big)\;,
\end{aligned}
\tag{2.26}
$$

with contributions by partial waves,

$$
\begin{aligned}
V_{\rm ct}^{(4)}(^1S_0) &= \widehat{D}_{^1S_0}({p'}^4 + p^4) + D_{^1S_0}{p'}^2p^2 \\
V_{\rm ct}^{(4)}(^3P_0) &= D_{^3P_0}({p'}^3p + p'p^3) \\
V_{\rm ct}^{(4)}(^1P_1) &= D_{^1P_1}({p'}^3p + p'p^3) \\
V_{\rm ct}^{(4)}(^3P_1) &= D_{^3P_1}({p'}^3p + p'p^3) \\
V_{\rm ct}^{(4)}(^3S_1) &= \widehat{D}_{^3S_1}({p'}^4 + p^4) + D_{^3S_1}{p'}^2p^2 \\
V_{\rm ct}^{(4)}(^3D_1) &= D_{^3D_1}{p'}^2p^2 \\
V_{\rm ct}^{(4)}(^3S_1 -^3 D_1) &= \widehat{D}_{^3S_1-^3D_1}p^4 + D_{^3S_1-^3D_1}{p'}^2p^2 \\
V_{\rm ct}^{(4)}(^3D_1 -^3 S_1) &= \widehat{D}_{^3S_1-^3D_1}{p'}^4 + D_{^3S_1-^3D_1}{p'}^2p^2 \\
V_{\rm ct}^{(4)}(^1D_2) &= D_{^1D_2}{p'}^2p^2 \\
V_{\rm ct}^{(4)}(^3D_2) &= D_{^3D_2}{p'}^2p^2 \\
V_{\rm ct}^{(4)}(^3P_2) &= D_{^3P_2}({p'}^3p + p'p^3) \\
V_{\rm ct}^{(4)}(^3P_2 -^3 F_2) &= D_{^3P_2-^3F_2}p'p^3 \\
V_{\rm ct}^{(4)}(^3F_2 -^3 P_2) &= D_{^3P_2-^3F_2}{p'}^3p \\
V_{\rm ct}^{(4)}(^3D_3) &= D_{^3D_3}{p'}^2p^2 \,.
\end{aligned}
\tag{2.27}
$$

Reference [1] provides formulas that relate the $D_{^{(2S+1)}L_J}$ to the D_i.

The next higher order is sixth order (N^{5}LO) at which, finally, also F-waves are affected in the following way:

$$
\begin{aligned}
V_{\rm ct}^{(6)}(^3F_2) &= E_{^3F_2}{p'}^3p^3 \\
V_{\rm ct}^{(6)}(^1F_3) &= E_{^1F_3}{p'}^3p^3 \\
V_{\rm ct}^{(6)}(^3F_3) &= E_{^3F_3}{p'}^3p^3 \\
V_{\rm ct}^{(6)}(^3F_4) &= E_{^3F_4}{p'}^3p^3 \,.
\end{aligned}
\tag{2.28}
$$

To obtain an optimal fit of the NN data at the highest order we consider in this paper, we include the above F-wave contacts in our N^{4}LO potentials.

2.2.5 Charge dependence

This is to summarize what charge-dependence we include. Through all orders, we take the charge-dependence of the 1PE due to pion-mass splitting into account, Eqs. (A.2) and (A.3). Charge-dependence is seen most prominently in the $^1S_0$ state at low energies, particularly, in the $^1S_0$ scattering lengths. Charge-dependent 1PE cannot explain it all. The remainder is accounted for by treating the $^1S_0$ LO contact parameter, $\widetilde{C}_{^1S_0}$, Eq. (2.22), in a charge-dependent way. Thus, we will distinguish between $\widetilde{C}^{\rm pp}_{^1S_0}$, $\widetilde{C}^{\rm np}_{^1S_0}$, and $\widetilde{C}^{\rm nn}_{^1S_0}$. For pp scattering at any order, we include the relativistic Coulomb potential [45, 46]. Finally, at N^{3}LO and N^{4}LO, we take into account irreducible π-γ exchange [47], which affects only the np potential. We also take nucleon-mass splitting into account, or in other words, we always apply the correct values for the masses of the nucleons involved in the various charge-dependent NN potentials.

For a comprehensive discussion of all possible sources for the charge-dependence of the NN interaction, see Ref. [1].

2.2.6 The full potential

The sum of long-range [Eqs. (2.12)-(2.16)] plus short-range potentials [Eq. (2.20)] results in:

$$V_{\rm LO} \equiv V^{(0)} = V_{1\pi} + V_{\rm ct}^{(0)} \tag{2.29}$$

$$V_{\rm NLO} \equiv V^{(2)} = V_{\rm LO} + V_{2\pi}^{(2)} + V_{\rm ct}^{(2)} \tag{2.30}$$

$$V_{\rm NNLO} \equiv V^{(3)} = V_{\rm NLO} + V_{2\pi}^{(3)} \tag{2.31}$$

$$V_{\rm N3LO} \equiv V^{(4)} = V_{\rm NNLO} + V_{2\pi}^{(4)} + V_{3\pi}^{(4)} + V_{\rm ct}^{(4)} \tag{2.32}$$

$$V_{\rm N4LO} \equiv V^{(5)} = V_{\rm N3LO} + V_{2\pi}^{(5)} + V_{3\pi}^{(5)}\,, \tag{2.33}$$

where we left out the higher order corrections to the 1PE because, as discussed, they are absorbed by mass and coupling constant renormalizations (appendix A.1). It is also understood that the charge-dependence discussed in the previous subsection is included.

In our systematic potential construction, we follow the above scheme, except for two physically motivated modifications. We add to $V_{\rm N3LO}$ the $1/M_N$ correction of the NNLO 2PE proportional to c_i. This correction is proportional to c_i/M_N and appears nominally at fifth order, because we count $Q/M_N \sim (Q/\Lambda_\chi)^2$. This contribution is given in Eqs. (2.19)-(2.23) of Ref. [37] and we denote it by $V^{(5)}_{2\pi,c_i/M_N}$. In short, in Eq. (2.32), we replace

$$V_{\rm N3LO} \longmapsto V_{\rm N3LO} + V^{(5)}_{2\pi,c_i/M_N} \,. \tag{2.34}$$

As demonstrated in Ref. [15], the 2PE bubble diagram proportional to c_i^2 that appears at N^{3}LO is unrealistically attractive, while the c_i/M_N correction is large and repulsive. Therefore, it makes sense to group these diagrams together to arrive at a more realistic intermediate attraction at N^{3}LO.

The second modification consists of adding to $V_{\rm N4LO}$ the four F-wave contacts listed in Eq. (2.28) to ensure an optimal fit of the NN data for the potential of the highest order constructed in this work.

The potential V is, in principle, an invariant amplitude (with relativity taken into account perturbatively) and, thus, satisfies a relativistic scattering equation, like, e. g., the Blankenbeclar-Sugar (BbS) equation [48], which reads explicitly,

$$T(\vec{p}\,',\vec{p}) = V(\vec{p}\,',\vec{p}) + \int \frac{d^3p''}{(2\pi)^3}\, V(\vec{p}\,',\vec{p}\,'')\, \frac{M_N^2}{E_{p''}}\, \frac{1}{p^2-p''^2+i\epsilon}\, T(\vec{p}\,'',\vec{p}) \tag{2.35}$$

with $E_{p''} \equiv \sqrt{M_N^2+p''^2}$ and M_N the nucleon mass. The advantage of using a relativistic scattering equation is that it automatically includes relativistic kinematical corrections to all orders. Thus, in the scattering equation, no propagator modifications are necessary when moving up to higher orders.

Defining

$$\widehat{V}(\vec{p}\,',\vec{p}) \equiv \frac{1}{(2\pi)^3}\sqrt{\frac{M_N}{E_{p'}}}\, V(\vec{p}\,',\vec{p})\, \sqrt{\frac{M_N}{E_p}} \tag{2.36}$$

and

$$\widehat{T}(\vec{p}\,',\vec{p}) \equiv \frac{1}{(2\pi)^3}\sqrt{\frac{M_N}{E_{p'}}}\, T(\vec{p}\,',\vec{p})\, \sqrt{\frac{M_N}{E_p}}\,, \tag{2.37}$$

where the factor $1/(2\pi)^3$ is added for convenience, the BbS equation collapses into the usual, nonrelativistic Lippmann-Schwinger (LS) equation,

$$\widehat{T}(\vec{p}\,',\vec{p}) = \widehat{V}(\vec{p}\,',\vec{p}) + \int d^3p''\, \widehat{V}(\vec{p}\,',\vec{p}\,'')\, \frac{M_N}{p^2-p''^2+i\epsilon}\, \widehat{T}(\vec{p}\,'',\vec{p})\,. \tag{2.38}$$

Since $\widehat{V}$ satisfies Eq. (2.38), it may be regarded as a nonrelativistic potential. By the same token, $\widehat{T}$

may be considered as the nonrelativistic T-matrix. All technical aspects associated with the solution of the LS equation can be found in Appendix A of Ref. [49], including specific formulas for the calculation of the np and pp phase shifts (with Coulomb). Additional details concerning the relevant operators and their decompositions are given in section 4 of Ref. [50]. Finally, computational methods to solve the LS equation are found in Ref. [51].

2.2.7 Regularization and non-perturbative renormalization

Iteration of $\widehat{V}$ in the LS equation, Eq. (2.38), requires cutting $\widehat{V}$ off for high momenta to avoid infinities. This is consistent with the fact that ChPT is a low-momentum expansion which is valid only for momenta $Q < \Lambda_\chi \approx 1$ GeV. Therefore, the potential $\widehat{V}$ is multiplied with the regulator function $f(p', p)$,

$$\widehat{V}(\vec{p}\,', \vec{p}) \longmapsto \widehat{V}(\vec{p}\,', \vec{p})\, f(p', p) \tag{2.39}$$

with

$$f(p', p) = \exp[-(p'/\Lambda)^{2n} - (p/\Lambda)^{2n}]\,, \tag{2.40}$$

such that

$$\widehat{V}(\vec{p}\,', \vec{p})\, f(p', p) \approx \widehat{V}(\vec{p}\,', \vec{p}) \left\{ 1 - \left[\left(\frac{p'}{\Lambda}\right)^{2n} + \left(\frac{p}{\Lambda}\right)^{2n} \right] + \ldots \right\}. \tag{2.41}$$

For the cutoff parameter Λ, we apply three different values, namely, 450, 500, and 550 MeV.

Equation (2.41) provides an indication of the fact that the exponential cutoff does not necessarily affect the given order at which the calculation is conducted. For sufficiently large n, the regulator introduces contributions that are beyond the given order. Assuming a good rate of convergence of the chiral expansion, such orders are small as compared to the given order and, thus, do not affect the accuracy at the given order. Thus, we use $n = 2$ for 3PE and 2PE and $n = 4$ for 1PE (except in LO and NLO, where we use $n = 2$ for 1PE). For contacts of order ν, n is chosen such that $2n > \nu$.

In our calculations, we apply, of course, the exponential form, Eq. (2.40), and not the expansion Eq. (2.41). On a similar note, we also do not expand the square-root factors in Eqs. (2.36-2.37) because they are kinematical factors which guarantee relativistic elastic unitarity.

It is pretty obvious that results for the T-matrix may depend sensitively on the regulator and its cutoff parameter. The removal of such regulator dependence is known as renormalization. Proper renormalization of the chiral NN interaction is a controversial issue, see Section 4.5 of Ref. [1] for a more comprehensive discussion.

For a successful EFT (in its domain of validity), one must be able to claim independence of the predictions on the regulator within the theoretical error. Also, truncation errors must decrease as we go to higher and higher orders. These are precisely the goals of renormalization.

Lepage [52] has stressed that the cutoff independence should be examined for cutoffs below the hard scale and not beyond. Ranges of cutoff independence within the theoretical error are to be identified using Lepage plots [52]. A systematic investigation of this kind has been conducted in Ref. [53]. In that work, the error of the predictions was quantified by calculating the χ^2/datum for the reproduction of the np elastic scattering data as a function of the cutoff parameter Λ of the regulator function Eq. (2.40). Predictions by chiral np potentials at order NLO and NNLO were investigated applying Weinberg counting for the counter terms (NN contact terms). It is found that the reproduction of the np data at lab. energies below 200 MeV is generally poor at NLO, while at NNLO the χ^2/datum assumes acceptable values (a clear demonstration of order-by-order improvement). Moreover, at NNLO, a "plateau" of constant low χ^2 for cutoff parameters ranging from about 450 to 850 MeV can be identified. This may be perceived as cutoff independence (and, thus, successful renormalization) for the relevant range of cutoff parameters.

CHAPTER 3

Pion exchange contributions at N4LO

In the following chapter, the N^{4}LO contributions are summarized according to definitions made in section 2.2.3. These calculations were carried out in Ref. [37].

3.1 Two-pion exchange contributions at N4LO

The 2π-exchange contributions that occur at N^{4}LO are displayed graphically in Fig. 3.1. We present now the corresponding analytical expressions separately for each class.

3.1.1 Spectral functions for class (a)

The N^{4}LO 2π-exchange two-loop contributions of class (a) are shown in Fig. 3.1(a). For this class the spectral functions are obtained by integrating the product of the leading one-loop πN amplitude and the chiral $\pi\pi NN$ vertex proportional to c_i over the Lorentz-invariant 2π-phase space. In the $\pi\pi$ center-of-mass frame this integral can be expressed as an angular integral $\int_{-1}^{1} dx$ [12]. The results for the non-vanishing spectral functions read:

$$
\begin{aligned}
\mathrm{Im}V_C \;=\;& -\frac{m_\pi^5}{(4f_\pi)^6\pi^2}\Bigg\{ g_A^2\sqrt{u^2-4}\left(5-2u^2-\frac{2}{u^2}\right)\Big[24c_1+c_2(u^2-4)+6c_3(u^2-2)\Big]\ln\frac{u+2}{u-2} \\
&+\frac{8}{u}\Big[3\big(4c_1+c_3(u^2-2)\big)(4g_A^4u^2-10g_A^4+1)+c_2(6g_A^4u^2-10g_A^4-3)\Big]B(u) \\
&+\sqrt{u^2-4}\,\Bigg[3(2-u^2)\big(4c_1+c_3(u^2-2)\big)+c_2(7u^2-6-u^4)+\frac{4g_A^2}{u}(2u^2-1) \\
&\times\Big[4(6c_1-c_2-3c_3)+(c_2+6c_3)u^2\Big]+4g_A^4\Bigg(\frac{32}{u+2}(2c_1+c_3)+\frac{64}{3u}(6c_1+c_2-3c_3) \\
&+14c_3-5c_2-92c_1+\frac{8u}{3}(18c_3-5c_2)+\frac{u^2}{6}(36c_1+13c_2-156c_3) \\
&+\frac{u^4}{6}(2c_2+9c_3)\Bigg)\Bigg]\Bigg\}\,,
\end{aligned}
\tag{3.1}
$$

$$
\begin{aligned}
\mathrm{Im}W_S \;=\;& \mu^2\,\mathrm{Im}W_T=\frac{c_4\,g_A^2m_\pi^5}{(4f_\pi)^6\pi^2}\Bigg\{8g_A^2u(5-u^2)B(u)+\frac{1}{3}(u^2-4)^{5/2}\ln\frac{u+2}{u-2} \\
&+\frac{u}{3}\sqrt{u^2-4}\,\Big[g_A^2(30u-u^3-64)-4u^2+16\Big]\Bigg\}\,,
\end{aligned}
\tag{3.2}
$$

with the dimensionless variable $u=\mu/m_\pi>2$ and the logarithmic function

$$
B(u)=\ln\frac{u+\sqrt{u^2-4}}{2}\,. \tag{3.3}
$$

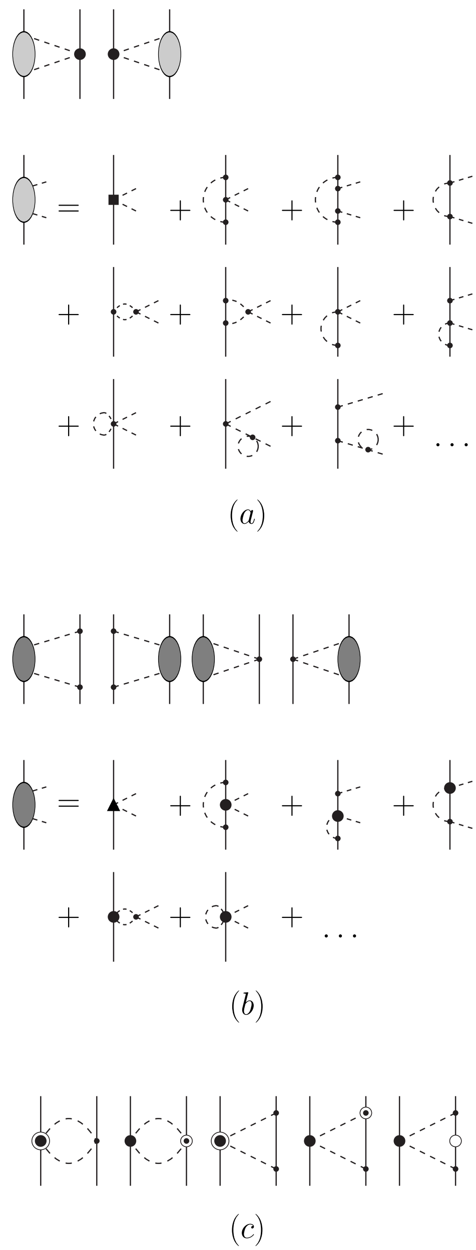

Figure 3.1: Two-pion-exchange contributions at N^{4}LO. (a) The leading one-loop πN amplitude is folded with the chiral $\pi\pi NN$ vertices proportional to c_i. (b) The one-loop πN amplitude proportional to c_i is folded with the leading order chiral πN amplitude. (c) Relativistic corrections of NNLO diagrams. Solid lines represent nucleons and dashed lines pions. Small dots, large solid dots, solid squares, and triangles denote vertices of index $d_i + n_i/2 - 2 = 0$, 1, 2, and 3, respectively. Open circles are relativistic $1/M_N$ corrections.

3.1.2 Spectral functions for class (b)

The N^{4}LO 2π-exchange two-loop contributions of class (b) are displayed in Fig. 3.1(b). For this class, the product of the one-loop πN amplitude proportional to c_i (see Ref. [31] for details) and the leading order chiral πN amplitude is integrated over the 2π-phase space. We obtain:

$$\mathrm{Im}V_S = \mu^2\,\mathrm{Im}V_T = \frac{g_A^4 m_\pi^5 (c_3-c_4)u}{(4f_\pi)^6\pi^2}\Big\{\sqrt{u^2-4}\,(u^3-30u+64)+24(u^2-5)B(u)\Big\}\,, \tag{3.4}$$

$$\begin{aligned}\mathrm{Im}W_S &= \mu^2\,\mathrm{Im}W_T = \frac{g_A^2 m_\pi^5}{(4f_\pi)^6\pi^2}(4-u^2)\Bigg\{\frac{c_4}{3}\Bigg[\sqrt{u^2-4}\,(2u^2-8)B(u)\\ &+4u(2+9g_A^2)-\frac{5u^3}{3}\Bigg]+2\bar{e}_{17}(8\pi f_\pi)^2(u^3-2u)\Bigg\}\,,\end{aligned} \tag{3.5}$$

$$\begin{aligned}\mathrm{Im}V_C &= \frac{g_A^2 m_\pi^5}{(4f_\pi)^6\pi^2}(u^2-2)\left(\frac{1}{u^2}-2\right)\Bigg\{2\sqrt{u^2-4}\Big[24c_1+c_2(u^2-4)+6c_3(u^2-2)\Big]B(u)\\ &+u\left[c_2\left(8-\frac{5u^2}{3}\right)+6c_3(2-u^2)-24c_1\right]\Bigg\}+\frac{3g_A^2 m_\pi^5}{(2f_\pi)^4 u}(2-u^2)^3\,\bar{e}_{14}\,,\end{aligned} \tag{3.6}$$

$$\begin{aligned}\mathrm{Im}W_C &= -\frac{c_1 m_\pi^5}{(2f_\pi)^6\pi^2}\Bigg\{\frac{3g_A^2+1}{8}\sqrt{u^2-4}\,(2-u^2)+\left(\frac{3g_A^2+1}{u}-2g_A^2\,u\right)B(u)\Bigg\}\\ &-\frac{c_2 m_\pi^5}{(2f_\pi)^6\pi^2}\\ &\times\Bigg\{\frac{1}{96}\sqrt{u^2-4}\,\Big[7u^2-6-u^4+g_A^2(5u^2-6-2u^4)\Big]+\frac{1}{4u}(g_A^2u^2-1-g_A^2)B(u)\Bigg\}\\ &-\frac{c_3 m_\pi^5}{(4f_\pi)^6\pi^2}\Bigg\{\frac{2}{9}\sqrt{u^2-4}\Bigg[3(7u^2-6-u^4)+4g_A^2\left(\frac{32}{u}-12-20u+7u^2-u^4\right)\\ &+g_A^4\left(114-\frac{512}{u}+368u-169u^2+7u^4+\frac{192}{u+2}\right)\Bigg]\\ &+\frac{16}{3u}\Big[g_A^4(6u^4-30u^2+35)+g_A^2(6u^2-8)-3\Big]B(u)\Bigg\}\\ &-\frac{c_4 g_A^2 m_\pi^5}{(4f_\pi)^6\pi^2}\Bigg\{\frac{2}{9}\sqrt{u^2-4}\,\Bigg[30-\frac{128}{u}+80u-13u^2-2u^4+g_A^2\left(\frac{512}{u}-114-368u\right.\\ &\left.+169u^2-7u^4-\frac{192}{u+2}\right)\Bigg]+\frac{16}{3u}\Big[5-3u^2+g_A^2(30u^2-35-6u^4)\Big]B(u)\Bigg\}\,.\end{aligned} \tag{3.7}$$

Consistent with the calculation of the πN amplitude in Ref. [31], we applied relations between LECs, such that only $\bar{e}_{14}$ and $\bar{e}_{17}$ remain in the final result.

3.1.3 Relativistic corrections

This group consists of diagrams with one vertex proportional to c_i and one $1/M_N$ correction. A few representative graphs are shown in Fig. 3.1(c). Since in this investigation we count $Q/M_N \sim (Q/\Lambda_\chi)^2$, these relativistic corrections are formally of order N^{4}LO. The result for this group of diagrams read in our sign-convention [12]:

$$\begin{aligned}
V_C &= \frac{g_A^2\, L(\tilde{\Lambda}; q)}{32\pi^2 M_N f_\pi^4}\big[(6c_3 - c_2)q^4 + 4(3c_3 - c_2 - 6c_1)q^2 m_\pi^2 \\
&\quad +6(2c_3 - c_2)m_\pi^4 - 24(2c_1 + c_3)m_\pi^6 w^{-2}\big]\,, \qquad (3.8)\\
W_C &= -\frac{c_4}{192\pi^2 M_N f_\pi^4}\left[g_A^2(8m_\pi^2 + 5q^2) + w^2\right] q^2\, L(\tilde{\Lambda}; q)\,, \qquad (3.9)\\
W_T &= -\frac{1}{q^2} W_S = \frac{c_4}{192\pi^2 M_N f_\pi^4}\left[w^2 - g_A^2(16m_\pi^2 + 7q^2)\right] L(\tilde{\Lambda}; q)\,, \qquad (3.10)\\
V_{LS} &= \frac{c_2\, g_A^2}{8\pi^2 M_N f_\pi^4}\, w^2 L(\tilde{\Lambda}; q)\,, \qquad (3.11)\\
W_{LS} &= -\frac{c_4}{48\pi^2 M_N f_\pi^4}\left[g_A^2(8m_\pi^2 + 5q^2) + w^2\right] L(\tilde{\Lambda}; q)\,, \qquad (3.12)
\end{aligned}$$

where the (regularized) logarithmic loop function is given by:

$$L(\tilde{\Lambda}; q) = \frac{w}{2q} \ln \frac{\tilde{\Lambda}^2(2m_\pi^2 + q^2) - 2m_\pi^2 q^2 + \tilde{\Lambda}\sqrt{\tilde{\Lambda}^2 - 4m_\pi^2}\, q\, w}{2m_\pi^2(\tilde{\Lambda}^2 + q^2)} \qquad (3.13)$$

with $w = \sqrt{4m_\pi^2 + q^2}$. Note that

$$\lim_{\tilde{\Lambda}\to\infty} L(\tilde{\Lambda}; q) = \frac{w}{q} \ln \frac{w + q}{2m_\pi}\,, \qquad (3.14)$$

is the logarithmic loop function of dimensional regularization.

3.2 Three-pion exchange contributions at N4LO

The 3π-exchange of order N^{4}LO is shown in Fig. 3.2. The spectral functions for these diagrams have been calculated in Ref. [11]. We use here the classification scheme introduced in that reference and note that class XI vanishes. Moreover, we find that the class X and part of class XIV make only negligible contributions. Thus, we include in our calculations only class XII and XIII, and the V_S contribution of class XIV. In Ref. [11] the spectral functions were presented in terms of an integral over the invariant mass of a pion pair. We have solved these integrals analytically and

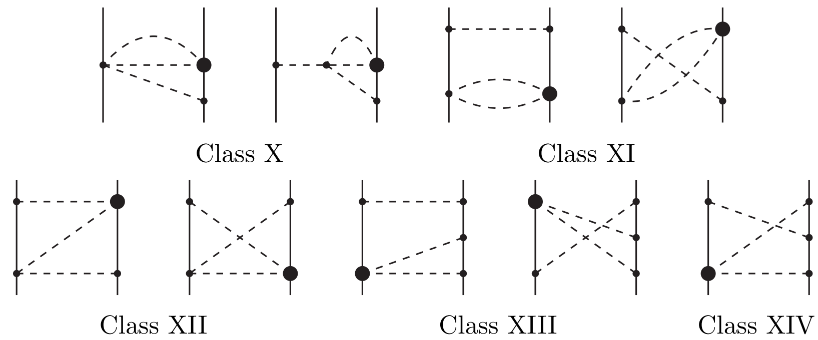

Figure 3.2: Three-pion exchange contributions at N^{4}LO. The classification scheme of Ref. [11] is used. Notation as in Fig. 3.1.

obtain the following spectral functions for the non-negligible cases:

$$\begin{aligned}
\mathrm{Im}\, V_S^{(\mathrm{XII})} &= -\frac{g_A^2 c_4 m_\pi^5}{(4f_\pi)^6 \pi^2 u^3} \bigg[\frac{y}{12}(u-1)(100u^3 - 27 - 50u - 151u^2 + 185u^4 - 14u^5 - 7u^6) \\
&\quad + 4\, D(u)\, (2 + 10u^2 - 9u^4) \bigg] , \qquad (3.15) \\
\mathrm{Im}\, V_T^{(\mathrm{XII})} &= \frac{1}{\mu^2}\, \mathrm{Im}\, V_S^{(\mathrm{XII})} - \frac{g_A^2 c_4 m_\pi^3}{(4f_\pi)^6 \pi^2 u^5} \bigg[\frac{y}{6}(u-1)(u^6 + 2u^5 - 39u^4 - 12u^3 + 65u^2 - 50u - 27) \\
&\quad + 8\, D(u)\, (3u^4 - 10u^2 + 2) \bigg] , \qquad (3.16) \\
\mathrm{Im}\, W_S^{(\mathrm{XII})} &= -\frac{g_A^2 m_\pi^5}{(4f_\pi)^6 \pi^2 u^3} \bigg\{ y\,(u-1) \bigg[\frac{4c_1 u}{3} \Big(u^3 + 2u^2 - u + 4 \Big) \\
&\quad + \frac{c_2}{72} \Big(u^6 + 2u^5 - 39u^4 - 12u^3 + 65u^2 - 50u - 27 \Big) \\
&\quad + \frac{c_3}{12} \Big(u^6 + 2u^5 - 31u^4 + 4u^3 + 57u^2 - 18u - 27 \Big) \\
&\quad + \frac{c_4}{72} \Big(7u^6 + 14u^5 - 185u^4 - 100u^3 + 151u^2 + 50u + 27 \Big) \bigg] \\
&\quad + D(u) \bigg[16c_1(4u^2 - 1 - u^4) + \frac{2c_2}{3} \Big(2 - 10u^2 + 3u^4 \Big) \\
&\quad + 4c_3 u^2 (u^2 - 2) + \frac{2c_4}{3} \Big(9u^4 - 10u^2 - 2 \Big) \bigg] \bigg\} , \qquad (3.17)
\end{aligned}$$

$$
\begin{aligned}
\mathrm{Im}\, W_T^{(\mathrm{XII})} &= \frac{1}{\mu^2}\,\mathrm{Im}\, W_S^{(\mathrm{XII})} - \frac{g_A^2 m_\pi^3}{(4f_\pi)^6 \pi^2 u^5}\Bigg\{ y\,(u-1)\Bigg[\frac{16c_1 u}{3}\Bigg(2+u-2u^2-u^3\Bigg) \\
&+\frac{c_2}{36}\Bigg(73u^4-6u^5-3u^6+44u^3-43u^2-50u-27\Bigg) \\
&+\frac{c_3}{2}\Bigg(19u^4-2u^5-u^6+4u^3-9u^2-6u-9\Bigg) \\
&+\frac{c_4}{36}\Bigg(39u^4-2u^5-u^6+12u^3-65u^2+50u+27\Bigg)\Bigg] \\
&+4\,D(u)\left[8c_1(u^4-1)+c_2\left(\frac{2}{3}-u^4\right)-2c_3u^4+\frac{c_4}{3}\left(10u^2-2-3u^4\right)\right]\Bigg\}\,, \qquad (3.18)
\end{aligned}
$$

$$
\mathrm{Im}\, W_C^{(\mathrm{XIII})} = -\frac{g_A^4 c_4 m_\pi^5}{(4f_\pi)^6\pi^2}\left[\frac{8y}{3}(u-1)(u-4-2u^2-u^3)+32\,D(u)\left(u^3-4u+\frac{1}{u}\right)\right], \qquad (3.19)
$$

$$
\begin{aligned}
\mathrm{Im}\, V_S^{(\mathrm{XIII})} &= -\frac{g_A^4 c_4 m_\pi^5}{(4f_\pi)^6\pi^2 u^3}\Bigg[\frac{y}{24}(u-1)(37u^6+74u^5-251u^4-268u^3+349u^2-58u-135) \\
&+2\,D(u)\,(39u^4-2-52u^2-6u^6)\Bigg]\,, \qquad (3.20)
\end{aligned}
$$

$$
\begin{aligned}
\mathrm{Im}\, V_T^{(\mathrm{XIII})} &= \frac{1}{\mu^2}\,\mathrm{Im}\, V_S^{(\mathrm{XIII})} - \frac{g_A^4 c_4 m_\pi^3}{(4f_\pi)^6\pi^2 u^5}\Bigg[\frac{y}{12}(u-1)(5u^6+10u^5-3u^4-252u^3-443u^2 \\
&-58u-135)+4\,D(u)\,(3u^4+22u^2-2)\Bigg]\,, \qquad (3.21)
\end{aligned}
$$

$$
\begin{aligned}
\mathrm{Im}\, W_S^{(\mathrm{XIII})} &= -\frac{g_A^4 m_\pi^5}{(4f_\pi)^6\pi^2 u^3}\Bigg\{ y\,(u-1)\Bigg[2c_1u(5u^3+10u^2-5u-4) \\
&+\frac{c_2}{48}\Bigg(135+58u-277u^2-36u^3+147u^4-10u^5-5u^6\Bigg) \\
&+\frac{c_3}{8}\Bigg(7u^6+14u^5-145u^4-20u^3+111u^2+18u+27\Bigg) \\
&+\frac{c_4}{6}\Bigg(44u^3+37u^4-14u^5-7u^6-3u^2-18u-27\Bigg)\Bigg] \\
&+D(u)\Bigg[24c_1(1+4u^2-3u^4)+c_2(2+2u^2-3u^4) \\
&+6c_3u^2(3u^2-2)+8c_4u^2(u^4-5u^2+5)\Bigg]\Bigg\}\,, \qquad (3.22)
\end{aligned}
$$

$$\begin{aligned}
\mathrm{Im}\, W_T^{(\mathrm{XIII})} &= \frac{1}{\mu^2}\,\mathrm{Im}\, W_S^{(\mathrm{XIII})} - \frac{g_A^4 m_\pi^3}{(4f_\pi)^6 \pi^2 u^5}\Bigg\{ y\,(u-1)\bigg[4c_1 u(5u^3+10u^2+7u-4) \\
&+\frac{c_2}{24}\bigg(135+58u+227u^2+204u^3+27u^4-10u^5-5u^6\bigg) \\
&+\frac{c_3}{4}\bigg(27+18u-9u^2-68u^3-121u^4+14u^5+7u^6\bigg) \\
&+c_4(4u^3+19u^4-2u^5-u^6-9u^2-6u-9)\bigg] \\
&+2\,D(u)\,\bigg[24c_1(1-3u^4)+c_2(2-10u^2-3u^4) \\
&+6c_3u^2(3u^2+2)-8c_4u^4\bigg]\Bigg\}\,, \qquad (3.23) \\
\mathrm{Im}\, V_S^{(\mathrm{XIV})} &= -\frac{g_A^4 c_4 m_\pi^5}{(4f_\pi)^6 \pi^2 u^3}\bigg[\frac{y}{24}(u-1)(637u^2-58u-135+116u^3-491u^4-22u^5-11u^6) \\
&+2\,D(u)\,(6u^6-9u^4+8u^2-2)\bigg]\,, \qquad (3.24)
\end{aligned}$$

where $y=\sqrt{(u-3)(u+1)}$ and $D(u)=\ln[(u-1+\,y)/2]$ with $u=\mu/m_\pi>3$.

CHAPTER 4

Dominant pion exchange contributions at N5LO

In the following chapter, the N^{5}LO contributions are summarized according to definitions made in section 2.2.3. These calculations were carried out in Ref. [39].

4.1 Two-pion exchange contributions at N5LO

The 2π-exchange contributions that occur at N^{5}LO are displayed graphically in Fig. 4.1. We will now discuss each class separately.

4.1.1 Spectral functions for 2π-exchange class (a)

The N^{5}LO 2π-exchange two-loop contributions, denoted by class (a), are shown in Fig. 4.1(a). For this class the spectral functions are obtained by integrating the product of the subleading one-loop πN-amplitude (see Ref. [31] for details) and the chiral $\pi\pi NN$-vertex proportional to c_i over the Lorentz-invariant 2π-phase space. In the $\pi\pi$ center-of-mass frame this integral can be expressed as an angular integral $\int_{-1}^{1} dx$ [12]. Altogether, the results for the non-vanishing spectral functions read:

$$\begin{aligned}
\mathrm{Im} V_C \; = \; & \frac{m_\pi^6 \sqrt{u^2-4}}{(8\pi f_\pi^2)^3}\left(\frac{1}{u^2}-2\right)\Big[(c_2+6c_3)u^2+4(6c_1-c_2-3c_3)\Big]\bigg\{2c_1 u+\frac{c_2 u}{36}(5u^2-24) \\
& +\frac{c_3 u}{2}(u^2-2)+\Big[c_3(2-u^2)+\frac{c_2}{6}(4-u^2)-4c_1\Big]\sqrt{u^2-4}\,B(u)\bigg\} \\
& +\frac{m_\pi^6\sqrt{u^2-4}}{8\pi f_\pi^4 u}\bigg\{\Big[4c_1+c_3(u^2-2)\Big]\Big[\bar{e}_{15}(u^4-6u^2+8)+6\bar{e}_{14}(u^2-2)^2+\frac{3\bar{e}_{16}}{10}(u^2-4)^2\Big] \\
& +c_2(u^2-4)\Big[\frac{3\bar{e}_{15}}{10}(u^4-6u^2+8)+\bar{e}_{14}(u^2-2)^2+\frac{3\bar{e}_{16}}{28}(u^2-4)^2\Big]\bigg\}\,, \qquad (4.1)
\end{aligned}$$

$$\begin{aligned}
\mathrm{Im} W_S \; = \; & \frac{c_4^2 m_\pi^6 (u^2-4)}{9(8\pi f_\pi^2)^3}\bigg\{u\sqrt{u^2-4}\Big[\frac{5u^2}{6}-4+\frac{2g_A^2}{15}(2u^2-23)\Big]-(u^2-4)^2 B(u) \\
& +6g_A^2 u\int_0^1 dx\left(x-\frac{1}{x}\right)\Big[4+(u^2-4)x^2\Big]^{3/2}\ln\frac{x\sqrt{u^2-4}+\sqrt{4+(u^2-4)x^2}}{2}\bigg\} \\
& +\frac{c_4 m_\pi^6 u(u^2-4)^{3/2}}{240\pi f_\pi^4}\Big[10\bar{e}_{17}(2-u^2)+\bar{e}_{18}(4-u^2)\Big]=\mu^2\,\mathrm{Im} W_T\,, \qquad (4.2)
\end{aligned}$$

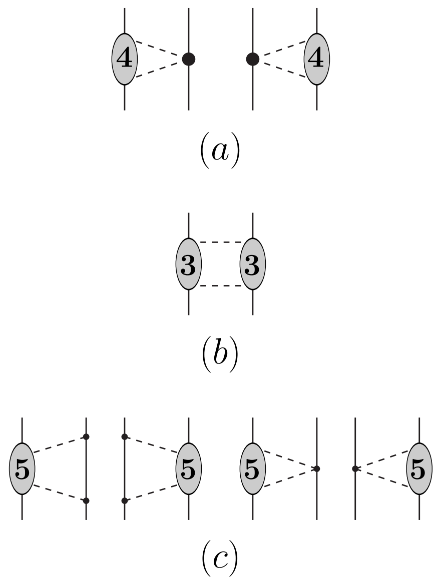

Figure 4.1: Two-pion-exchange contributions to the NN-interaction at N^{5}LO. (a) The subleading one-loop πN-amplitude is folded with the chiral $\pi\pi NN$-vertices proportional to c_i. (b) The leading one-loop πN-amplitude is folded with itself. (c) The leading two-loop πN-amplitude is folded with the tree-level πN-amplitude. Solid lines represent nucleons and dashed lines pions. Small dots and large solid dots denote vertices of chiral order one and two, respectively. Shaded ovals represent complete πN-scattering amplitudes with their order specified by the number in the oval.

with the dimensionless variable $u = \mu/m_\pi > 2$ and the logarithmic function

$$B(u) = \ln \frac{u + \sqrt{u^2 - 4}}{2} \,. \tag{4.3}$$

Consistent with the calculation of the πN-amplitude in Ref. [31], we utilized the relations between the fourth-order LECs, such that only $\bar{e}_{14}$ to $\bar{e}_{18}$ remain in the final result.

4.1.2 Spectral functions for 2π-exchange class (b)

A first set of 2π-exchange contributions at three-loop order, denoted by class (b), is displayed in Fig. 4.1(b). For this class of diagrams, the leading one-loop πN-scattering amplitude is multiplied with itself and integrated over the 2π-phase space. Including also the symmetry factor 1/2, one gets for the spectral-functions:

$$\begin{aligned}
\mathrm{Im} V_C \;=\; & \frac{m_\pi^6 \sqrt{u^2-4}}{(4f_\pi)^8 \pi^3 u} \Bigg\{ -\frac{3}{70}(5u^2+8)(u^2-4)^2 + 3g_A^2(1-2u^2)\left[1 + \frac{2-u^2}{4u} \ln \frac{u+2}{u-2}\right] \\
& \times \left[u - \frac{u^3}{2} + \frac{4B(u)}{\sqrt{u^2-4}}\right] + g_A^4 \Bigg[\frac{32(3-2u^2)}{\sqrt{u^2-4}} B(u) + 3(2u^2-1)^2 \Bigg(\frac{u^2-2}{u} \ln \frac{u+2}{u-2} \\
& + \frac{(u^2-2)^2}{8u^2}\left(\pi^2 - \ln^2 \frac{u+2}{u-2}\right)\Bigg) - \frac{2258}{35} + 24u + \frac{5336u^2}{105} - 12u^3 - \frac{2216u^4}{105} + \frac{18u^6}{35}\Bigg] \\
& + g_A^6(2u^2-1)\left(1 + \frac{2-u^2}{4u} \ln \frac{u+2}{u-2}\right)\left[46u - 3u^3 - 96 + \frac{64}{u+2} + \frac{24(5-2u^2)}{\sqrt{u^2-4}} B(u)\right] \\
& + \frac{64 g_A^8}{9}\Bigg[\frac{3119u^2}{70} - \frac{71u^6}{1120} - \frac{197u^4}{70} - \frac{85u^3}{8} + \frac{97u}{4} - \frac{582}{7} - \frac{16}{u+2} + \frac{8}{(u+2)^2} \\
& + \frac{6u^4 - 60u^2 + 105}{\sqrt{u^2-4}} B(u)\Bigg]\Bigg\} ,
\end{aligned} \tag{4.4}$$

$$\begin{aligned}
\mathrm{Im} W_S \;=\; & \frac{g_A^4 m_\pi^6 \sqrt{u^2-4}}{(4f_\pi)^8 \pi^3 u} \Bigg\{ \frac{u^2-4}{48}\left[4u + (4-u^2) \ln \frac{u+2}{u-2}\right]^2 - \frac{\pi^2}{48}(u^2-4)^3 \\
& + g_A^2 u \left[(u^2-4) \ln \frac{u+2}{u-2} - 4u\right]\left[\frac{5u}{4} - \frac{u^3}{24} - \frac{8}{3} + \frac{5-u^2}{\sqrt{u^2-4}} B(u)\right] \\
& + \frac{32 g_A^4 u^2}{27}\left[\frac{u^4}{40} + \frac{13u^2}{10} + \frac{11u}{2} - \frac{118}{5} - \frac{8}{u+2} + \frac{3(10-u^2)}{\sqrt{u^2-4}} B(u)\right]\Bigg\} \\
= \;& \mu^2 \, \mathrm{Im} W_T \,,
\end{aligned} \tag{4.5}$$

$$
\begin{aligned}
\mathrm{Im}V_S &= \frac{g_A^8 m_\pi^6 u\sqrt{u^2-4}}{3(4f_\pi)^8\pi^5}\int_0^1 dx\,(x^2-1)\Bigg\{(u^2-4)x\left[\frac{48\pi^2 f_\pi^2}{g_A^4}(\bar{d}_{14}-\bar{d}_{15})-\frac{1}{6}\right]+\frac{4}{x}\\
&\quad -\frac{\left[4+(u^2-4)x^2\right]^{3/2}}{x^2\sqrt{u^2-4}}\ln\frac{x\sqrt{u^2-4}+\sqrt{4+(u^2-4)x^2}}{2}\Bigg\}^2 = \mu^2\mathrm{Im}V_T\,, \qquad (4.6)
\end{aligned}
$$

$$
\begin{aligned}
\mathrm{Im}W_C &= -\frac{m_\pi^6(u^2-4)^{5/2}}{(4f_\pi)^8(3\pi u)^3}\left[2+4g_A^2-\frac{u^2}{2}(1+5g_A^2)\right]^2+\frac{m_\pi^6(u^2-4)^{3/2}}{9(4f_\pi)^8\pi^5 u}\int_0^1 dx\,x^2\Bigg\{\frac{3x^2}{2}(4-u^2)\\
&\quad +3x\sqrt{u^2-4}\sqrt{4+(u^2-4)x^2}\ln\frac{x\sqrt{u^2-4}+\sqrt{4+(u^2-4)x^2}}{2}+g_A^4\Big[(4-u^2)x^2\\
&\quad +2u^2-4\Big]\left[\frac{5}{6}+\frac{4}{(u^2-4)x^2}-\left(1+\frac{4}{(u^2-4)x^2}\right)^{3/2}\ln\frac{x\sqrt{u^2-4}+\sqrt{4+(u^2-4)x^2}}{2}\right]\\
&\quad +\left[4(1+2g_A^2)-u^2(1+5g_A^2)\right]\sqrt{u^2-4}\,\frac{B(u)}{u}+\frac{u^2}{6}(5+13g_A^2)-4(1+2g_A^2)\\
&\quad +96\pi^2 f_\pi^2\left[(4-2u^2)(\bar{d}_1+\bar{d}_2)+(4-u^2)x^2\bar{d}_3+8\bar{d}_5\right]\Bigg\}^2\,. \qquad (4.7)
\end{aligned}
$$

Note the squared integrands in the last two equations. The parameters $\bar{d}_j$ belong to the $\pi\pi NN$-contact vertices of third chiral order.

4.1.3 2π class (c)

Further 2π-exchange three-loop contributions at N^{5}LO, denoted by class (c), are shown in Fig. 4.1(c). For these the two-loop πN-scattering amplitude (which is of order five) would have to be folded with the tree-level πN-amplitude. To our knowledge, the two-loop elastic πN-scattering amplitude has never been evaluated in some decent analytical form. Note that the loops involved in the class (c) contributions include only leading order chiral πN-vertices. According to our experience such contributions are typically small. For these reasons we omit class (c) in the present calculation.

4.1.4 Relativistic $1/M_N^2$-corrections

This group consists of the $1/M_N^2$-corrections to the chiral leading 2π-exchange diagrams. Representative graphs are shown in Fig. 4.2. Since we count $Q/M_N \sim (Q/\Lambda_\chi)^2$, these relativistic corrections are formally of sixth order (N^{5}LO). The expressions for the corresponding NN-amplitudes are adopted from Ref. [13]:

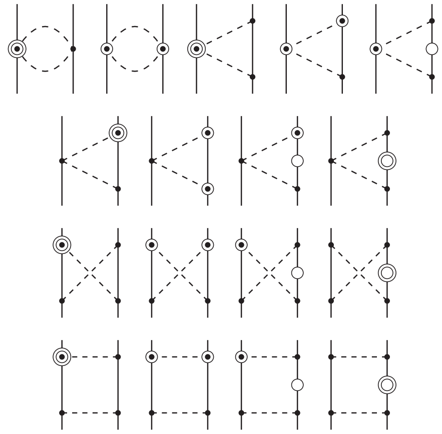

Figure 4.2: Relativistic $1/M_N^2$ corrections to 2π-exchange diagrams that are counted as order six. Notation as in Fig. 4.1. Open circles represent $1/M_N$-corrections.

$$V_C = \frac{g_A^4}{32\pi^2 M_N^2 f_\pi^4}\left[L(\tilde{\Lambda};q)\left(2m_\pi^4+q^4-8m_\pi^6 w^{-2}-2m_\pi^8 w^{-4}\right)-\frac{m_\pi^6}{2w^2}\right], \tag{4.8}$$

$$\begin{aligned} W_C = & \frac{1}{192\pi^2 M_N^2 f_\pi^4}\Bigg\{L(\tilde{\Lambda};q)\Bigg[g_A^2\left(2k^2(8m_\pi^2+5q^2)+12m_\pi^6 w^{-2}-3q^4-6m_\pi^2 q^2-6m_\pi^4\right) \\ & +g_A^4\Big(k^2(16m_\pi^4 w^{-2}-20m_\pi^2-7q^2)-16m_\pi^8 w^{-4}-12m_\pi^6 w^{-2}+4m_\pi^4 q^2 w^{-2}+5q^4 \\ & +6m_\pi^2 q^2+6m_\pi^4\Big)+k^2 w^2\Bigg]-\frac{4g_A^4 m_\pi^6}{w^2}\Bigg\}, \end{aligned} \tag{4.9}$$

$$V_T = -\frac{1}{q^2}V_S = \frac{g_A^4\, L(\tilde{\Lambda};q)}{32\pi^2 M_N^2 f_\pi^4}\left(k^2+\frac{5}{8}q^2+m_\pi^4 w^{-2}\right), \tag{4.10}$$

$$W_T = -\frac{1}{q^2}W_S = \frac{L(\tilde{\Lambda};q)}{1536\pi^2 M_N^2 f_\pi^4}\left[g_A^4\left(28m_\pi^2+17q^2+16m_\pi^4 w^{-2}\right)-2g_A^2(16m_\pi^2+7q^2)+w^2\right], \tag{4.11}$$

$$V_{LS} = \frac{g_A^4\, L(\tilde{\Lambda};q)}{128\pi^2 M_N^2 f_\pi^4}\left(11q^2+32m_\pi^4 w^{-2}\right), \tag{4.12}$$

$$W_{LS} = \frac{L(\tilde{\Lambda};q)}{256\pi^2 M_N^2 f_\pi^4}\left[2g_A^2(8m_\pi^2+3q^2)+\frac{g_A^4}{3}\left(16m_\pi^4 w^{-2}-11q^2-36m_\pi^2\right)-w^2\right], \tag{4.13}$$

$$V_{\sigma L} = \frac{g_A^4\, L(\tilde{\Lambda};q)}{32\pi^2 M_N^2 f_\pi^4}\,, \tag{4.14}$$

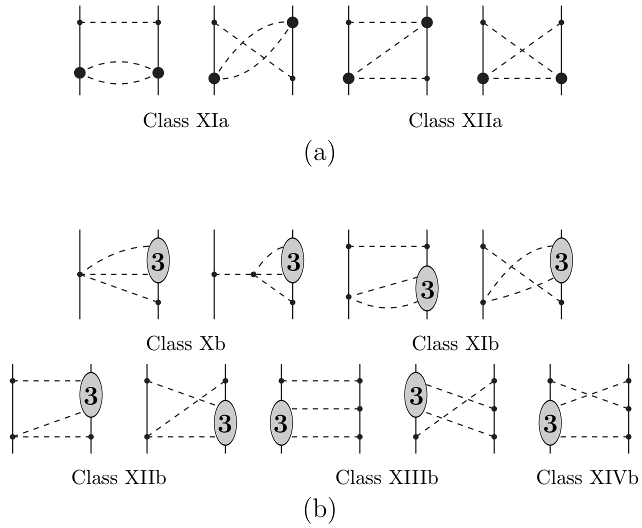

Figure 4.3: Three-pion exchange contributions at N^{5}LO. (a) Diagrams proportional to c_i^2. (b) Diagrams involving the one-loop πN-amplitude. Roman numerals refer to sub-classes following the scheme introduced in Refs. [11, 37]. Notation as in Fig. 4.1.

where the (regularized) logarithmic loop function is given by

$$L(\tilde{\Lambda}; q) = \frac{w}{2q} \ln \frac{\tilde{\Lambda}^2(2m_\pi^2 + q^2) - 2m_\pi^2 q^2 + \tilde{\Lambda}\sqrt{\tilde{\Lambda}^2 - 4m_\pi^2}\, q\, w}{2m_\pi^2(\tilde{\Lambda}^2 + q^2)}\,, \tag{4.15}$$

with the abbreviation $w = \sqrt{4m_\pi^2 + q^2}$.

4.2 Three-pion exchange contributions at N5LO

The 3π-exchange contributions of order N^{5}LO are shown in Fig. 4.3. We can distinguish between diagrams which are proportional to c_i^2 [Fig. 4.3(a)] and contributions that involve (parts of) the leading one-loop πN amplitude [Fig. 4.3(b)]. Below, we present the spectral functions for each class.

4.2.1 Spectral functions for 3π-exchange class (a)

This class consists of the diagrams displayed in Fig. 4.3(a). They are characterized by the presence of one subleading $\pi\pi NN$-vertex in each nucleon line. Using a notation introduced in Refs. [11, 37], we distinguish between the various sub-classes of diagrams by roman numerals.

Class XIa:

$$\mathrm{Im}W_C = \frac{g_A^2 c_4^2 m_\pi^6}{6(4\pi f_\pi^2)^3} \int_2^{u-1} dw\, (w^2-4)^{3/2} \sqrt{\lambda(w)}\,, \tag{4.16}$$

$$\begin{aligned}\mathrm{Im}V_S \;=\; & \frac{g_A^2 c_4^2 m_\pi^6}{6(8\pi f_\pi^2)^3} \int_2^{u-1} dw\, \frac{(w^2-4)^{3/2}}{u^4\sqrt{\lambda(w)}} \Big[w^8 - 4(1+u^2)w^6 + 2w^4(3+5u^2) \\ & +4w^2(2u^6-5u^4-2u^2-1) - (u^2-1)^3(5u^2+1)\Big]\,,\end{aligned} \tag{4.17}$$

$$\mathrm{Im}(\mu^2 V_T - V_S) = \frac{g_A^2 c_4^2 m_\pi^6}{6(8\pi f_\pi^2)^3} \int_2^{u-1} dw\, (w^2-4)^{3/2} \sqrt{\lambda(w)} \left[\frac{(w^2-1)^2}{u^4} + 1 - \frac{2}{u^2}(7w^2+1)\right], \tag{4.18}$$

with the kinematical function $\lambda(w) = w^4+u^4+1-2(w^2u^2+w^2+u^2)$. The dimensionless integration variable w is the invariant mass of a pion-pair divided by m_π.

Class XIIa:

$$\mathrm{Im}V_C = \frac{g_A^2 c_4^2 m_\pi^6}{8960\pi f_\pi^6}\, (u-3)^3 \left[u^3 + 9u^2 + 12u - 3 - \frac{3}{u}\right], \tag{4.19}$$

$$\mathrm{Im}W_C = \frac{2g_A^2 c_4^2 m_\pi^6 u^2}{(4\pi f_\pi^2)^3} \iint\limits_{z^2<1} d\omega_1 d\omega_2\, k_1 k_2 \sqrt{1-z^2}\, \arcsin(z)\,, \tag{4.20}$$

$$\begin{aligned}\mathrm{Im}V_S \;=\; & \frac{g_A^2 c_4^2 m_\pi^6}{(4\pi f_\pi^2)^3} \iint\limits_{z^2<1} d\omega_1 d\omega_2 \Big\{2\omega_1^2(\omega_2^2 - 9\omega_2 u + 9u^2+1) + 3\omega_1\big[\omega_2(1+8u^2) - 6u - 6u^3\big] \\ & +\frac{1}{4}(9u^4+18u^2+5) + \frac{2zk_2}{k_1}\Big[\omega_1^3(4u-\omega_2) + \omega_1^2(7\omega_2 u - 2 - 2u^2) - 2\omega_1(2u+\omega_2) \\ & +2+2u^2-4\omega_2 u\Big] + \frac{3\arcsin(z)}{k_1 k_2\sqrt{1-z^2}}\Big[2\omega_1^3 u(u^2+1-2\omega_2 u) + \omega_1^2\Big(\omega_2 u(7+11u^2) - 5\omega_2^2 u^2 \\ & -1-4u^2-3u^4\Big) + \frac{\omega_1}{4}\Big(6u^5+12u^3-2u-\omega_2(5+16u^2+15u^4)\Big) + \frac{(1-u^4)(u^2+3)}{8}\Big]\Big\}\,,\end{aligned} \tag{4.21}$$

$$\mathrm{Im}(\mu^2 V_T - V_S) = \frac{g_A^2 c_4^2 m_\pi^6}{(4\pi f_\pi^2)^3} \iint\limits_{z^2<1} d\omega_1 d\omega_2 \Big\{ 4\omega_1^2(\omega_2^2 + 6u^2 + 2 - 10\omega_2 u) + 6u^2(1+u^2)$$
$$+2\omega_1\big[3\omega_2(1+7u^2) - 18u^3 - 10u\big] + \frac{2zk_2}{k_1}\Big[\omega_1^3(7u - 2\omega_2) + u^2 - \omega_2 u$$
$$+\omega_1^2(13\omega_2 u - 3 - 10u^2) + \omega_1(2+3u^2)(u-2\omega_2)\Big] + \frac{3\arcsin(z)}{k_1 k_2\sqrt{1-z^2}}$$
$$\times(u^2 - 2\omega_1 u + 1)(u^2 - 2\omega_2 u + 1)\left[\frac{\omega_1}{2}(6u - 5\omega_2) - \frac{u^2}{2} - 2\omega_1^2\right]\Big\}, \qquad (4.22)$$

with the magnitudes of pion-momenta divided by m_π, and their scalar-product given by:

$$k_1 = \sqrt{\omega_1^2 - 1}\,, \qquad k_2 = \sqrt{\omega_2^2 - 1}\,, \qquad z\,k_1 k_2 = \omega_1\omega_2 - u(\omega_1 + \omega_2) + \frac{u^2+1}{2}\,. \qquad (4.23)$$

The upper/lower limits of the ω_2-integration are

$$\omega_2^\pm = \frac{1}{2}(u - \omega_1 \pm k_1\sqrt{u^2 - 2\omega_1 u - 3}/\sqrt{u^2 - 2\omega_1 u + 1}\,)$$

with ω_1 in the range $1 < \omega_1 < (u^2-3)/2u$.

The contributions to $\mathrm{Im}W_S$ and $\mathrm{Im}(\mu^2 W_T - W_S)$ are split into three pieces according to their dependence on the isoscalar/isovector low-energy constants $c_{1,3}$ and c_4:

$$\mathrm{Im}W_S = \frac{g_A^2 m_\pi^6 (u-3)^2}{2240\pi f_\pi^6}\Big\{7c_1^2\left(\frac{4}{3} + \frac{3}{u} - \frac{2}{3u^2} - \frac{1}{u^3}\right) + c_1 c_3\Big(\frac{2u^2}{3} + 4u - \frac{2}{3}$$
$$-\frac{5}{u} - \frac{2}{3u^2} - \frac{1}{u^3}\Big) + c_3^2\left(\frac{3u^2}{4} + \frac{u}{8} - \frac{5}{2} - \frac{3}{u} + \frac{19}{12u^2} + \frac{19}{8u^3}\right)\Big\}, \qquad (4.24)$$

$$\mathrm{Im}(\mu^2 W_T - W_S) = \frac{g_A^2 m_\pi^6 (u-3)}{1120\pi f_\pi^6}\Big\{7c_1^2\left(\frac{1}{3u} + \frac{1}{u^2} + \frac{3}{u^3} - 2u - 1\right) + c_1 c_3\Big(13u + 4 - 5u^2 - \frac{5u^3}{3}$$
$$+\frac{1}{3u} + \frac{1}{u^2} + \frac{3}{u^3}\Big) + \frac{c_3^2}{8}\left(23u^2 - \frac{u^5}{3} - u^4 - 4u^3 - 8u - 3 + \frac{8}{3u} - \frac{19}{u^2} - \frac{57}{u^3}\right)\Big\}, \qquad (4.25)$$

$$\mathrm{Im}W_S = \frac{g_A^2 c_4 m_\pi^6}{1120\pi f_\pi^6}(u-3)^2\Bigg\{c_1\left(u^2+6u-1-\frac{15}{2u}-\frac{1}{u^2}-\frac{3}{2u^3}\right) + \frac{c_3}{4}\left(\frac{2u^4}{9}+\frac{4u^3}{3}+\frac{u^2}{3}-\frac{25u}{6}+\frac{6}{u}+\frac{1}{u^2}+\frac{3}{2u^3}\right)\Bigg\}, \tag{4.26}$$

$$\mathrm{Im}(\mu^2 W_T - W_S) = \frac{g_A^2 c_4 m_\pi^6}{1120\pi f_\pi^6}(u-3)^3\Bigg\{c_1\left(\frac{1}{u^2}+\frac{1}{u^3}-\frac{u}{3}-3-\frac{4}{u}\right) + \frac{c_3}{4}\left(\frac{u^3}{9}+u^2+\frac{5u}{3}+\frac{8}{3}+\frac{11}{3u}-\frac{1}{u^2}-\frac{1}{u^3}\right)\Bigg\}, \tag{4.27}$$

$$\mathrm{Im}W_S = \frac{g_A^2 c_4^2 m_\pi^6}{8960\pi f_\pi^6}(u-3)^2\left(\frac{25u}{12}-\frac{u^4}{9}-\frac{2u^3}{3}-\frac{u^2}{6}-\frac{3}{u}-\frac{1}{2u^2}-\frac{3}{4u^3}\right), \tag{4.28}$$

$$\mathrm{Im}(\mu^2 W_T - W_S) = \frac{g_A^2 c_4^2 m_\pi^6}{8960\pi f_\pi^6}(u-3)^3\left(\frac{1}{2u^2}+\frac{1}{2u^3}-\frac{u^3}{18}-\frac{u^2}{2}-\frac{5u}{6}-\frac{4}{3}-\frac{11}{6u}\right). \tag{4.29}$$

4.2.2 Spectral functions for 3π-exchange class (b)

This class is displayed in Fig. 4.3(b). Each 3π-exchange diagram of this class includes the one-loop πN-amplitude (completed by the low-energy constants $\bar{d}_j$). Only those parts of the πN-scattering amplitude, which are either independent of the pion CMS-energy ω or depend on it linearly could be treated with the techniques available. The contributions are, in general, small. Below, we present only the larger portions within this class. The omitted pieces are about one order of magnitude smaller. To facilitate a better understanding, we have subdivided this class into sub-classes labeled by roman numerals, following Refs. [11, 37].

The auxiliary function

$$G(w) = \left[1+2g_A^2-\frac{w^2}{4}(1+5g_A^2)\right]\frac{\sqrt{w^2-4}}{w}\ln\frac{w+\sqrt{w^2-4}}{2} + \frac{w^2}{24}(5+13g_A^2)-1-2g_A^2+48\pi^2 f_\pi^2\left[(2-w^2)(\bar{d}_1+\bar{d}_2)+4\bar{d}_5\right], \tag{4.30}$$

arises from the part linear in ω of the isovector non-spin-flip πN-amplitude $g^-(\omega,t)$ with $t=(wm_\pi)^2$

(see e.g. Appendix B in Ref. [31]). The spectral functions derived from this selected set of 3π-exchange diagrams read as follows.

Class Xb:

$$\mathrm{Im}W_S = \frac{g_A^2 m_\pi^6}{(4f_\pi)^8\pi^5}\int_2^{u-1} dw\,\frac{4G(w)}{27w^2u^4}\Big[(w^2-4)\lambda(w)\Big]^{3/2}\,, \tag{4.31}$$

$$\mathrm{Im}(\mu^2 W_T - W_S) = \frac{g_A^2 m_\pi^6}{(4f_\pi)^8\pi^5}\int_2^{u-1} dw\,\frac{4G(w)}{9w^2u^4}(w^2-4)^{3/2}\sqrt{\lambda(w)}\,\frac{3u^2+1}{u^2-1}\Big[u^4-(w^2-1)^2\Big]\,. \tag{4.32}$$

Class XIb:

$$\mathrm{Im}W_S = \frac{g_A^2 m_\pi^6}{(4f_\pi)^8\pi^5}\int_2^{u-1} dw\,\frac{8G(w)}{27w^2u^4}(w^2-4)^{3/2}\sqrt{\lambda(w)}\,\Big[2u^2(1+7w^2)-u^4-(w^2-1)^2\Big]\,, \tag{4.33}$$

$$\mathrm{Im}(\mu^2 W_T - W_S) = \frac{g_A^2 m_\pi^6}{(4f_\pi)^8\pi^5}\int_2^{u-1} dw\,\frac{8G(w)}{9w^2u^4}\,\frac{(w^2-4)^{3/2}}{\sqrt{\lambda(w)}}\,(u^2+1-w^2)^2\Big[2w^2(1+3u^2)-w^4-(u^2-1)^2\Big]\,. \tag{4.34}$$

Class XIIb:

$$\mathrm{Im}W_S = \frac{g_A^2 m_\pi^6}{9f_\pi^8(4\pi)^5}\iint\limits_{z^2<1} d\omega_1 d\omega_2\, G(w)\Big[(\omega_1^2+\omega_2^2-2)(1-3z^2)-5k_1k_2z\Big]\,, \tag{4.35}$$

$$\mathrm{Im}(\mu^2 W_T - W_S) = -\frac{g_A^2 m_\pi^6}{3f_\pi^8(4\pi)^5}\iint\limits_{z^2<1} d\omega_1 d\omega_2\, G(w)\omega_1\omega_2\left[5+2z\left(\frac{k_1}{k_2}+\frac{k_2}{k_1}\right)\right]\,, \tag{4.36}$$

setting $w=\sqrt{1+u^2-2u\omega_1}$.

Class XIIIb:

$$\mathrm{Im}V_S = \frac{g_A^4 m_\pi^6}{(4f_\pi)^8\pi^3u^3}\int_2^{u-1} dw\,2G(w)\lambda(w)(2-w^2)\,, \tag{4.37}$$

$$\mathrm{Im}(\mu^2 V_T - V_S) = \frac{g_A^4 m_\pi^6}{(4f_\pi)^8\pi^3u^3}\int_2^{u-1} dw\,4G(w)(2-w^2)(1+u^2-w^2)^2\,, \tag{4.38}$$

$$\mathrm{Im}W_S = \frac{g_A^4 m_\pi^6}{3f_\pi^8(4\pi)^5} \iint\limits_{z^2<1} d\omega_1 d\omega_2\, G(w) \bigg\{ u(\omega_1+4\omega_2) - 2 - \frac{\omega_1^2+8\omega_2^2}{3} + z^2(\omega_1^2+4\omega_2^2-5)$$
$$+\frac{zk_2}{k_1}(4u\omega_1+\omega_1^2-5) + \frac{zk_1}{k_2}(u\omega_2+\omega_2^2-2)$$
$$+\frac{\arcsin(z)}{\sqrt{1-z^2}}\left[\frac{k_1}{k_2}(1-u\omega_2)+z(1-u\omega_1)\right]\bigg\}, \tag{4.39}$$

$$\mathrm{Im}(\mu^2 W_T - W_S) = \frac{g_A^4 m_\pi^6}{f_\pi^8(4\pi)^5} \iint\limits_{z^2<1} d\omega_1 d\omega_2 \frac{2\omega_1}{3} G(w) \bigg\{ \frac{2\omega_2}{k_1^2}\Big[\omega_1(u-\omega_2)-1\Big] + u + 2\omega_2$$
$$+\frac{zk_1\omega_2}{k_2} + \frac{zk_2}{k_1}(4u+\omega_1) + \omega_1\Big(\frac{2zk_2}{k_1}\Big)^2$$
$$+\frac{\arcsin(z)}{k_1k_2\sqrt{1-z^2}}\Big[(1+u^2)\Big(\omega_1+\omega_2-\frac{u}{2}\Big) - 2u\omega_1\omega_2\Big]\bigg\}, \tag{4.40}$$

setting again $w = \sqrt{1+u^2-2u\omega_1}$.

Class XIVb:

$$\mathrm{Im}V_S = \frac{g_A^4 m_\pi^6}{(4f_\pi)^8\pi^3u^3} \int_2^{u-1} dw\, \frac{G(w)}{2}\, \lambda(w)\Big[u^2+w^2+4(u^2-1)w^{-2}-5\Big], \tag{4.41}$$

$$\mathrm{Im}(\mu^2V_T - V_S) = \frac{g_A^4 m_\pi^6}{(4f_\pi)^8\pi^3u^3} \int_2^{u-1} dw\, G(w)(w^2-1-u^2)\Big[w^4-2w^2(3+u^2)+(u^2-1)^2(1+4w^{-2})\Big]. \tag{4.42}$$

4.3 Four-pion exchange at N5LO

The exchange of four pions between two nucleons occurs for the first time at N^{5}LO. The pertinent diagrams involve three loops and only leading order vertices, which explains the sixth power in small momenta. Three-pion exchange with just leading order vertices turned out to be negligibly small [9, 10], and so we expect four-pion exchange with leading order vertices to be even smaller. Therefore, we can safely neglect this contribution.

CHAPTER 5

Perturbative NN scattering in peripheral partial waves

5.1 Perturbative K-matrix and phase shifts

5.1.1 N4LO case

Nucleon-nucleon scattering in peripheral partial waves is of special interest—for several reasons. First, these partial waves probe the long- and intermediate-range of the nuclear force. Due to the centrifugal barrier, there is only small sensitivity to short-range contributions and, in fact, the contact terms up to and including order N^{4}LO make no contributions for orbital angular momenta $L \geq 3$. Thus, for F and higher waves and energies below the pion-production threshold, we have a window in which the NN interaction is governed by chiral symmetry alone (chiral one- and multi-pion exchanges), and we can conduct a relatively clean test of how well the theory works. Using values for the LECs from πN analysis, the NN predictions are even parameter free. Moreover, the smallness of the phase shifts in peripheral partial waves suggests that the calculation can be done perturbatively. This avoids the complications and possible model-dependence (e.g., cutoff dependence) that the non-perturbative treatment of the Lippmann-Schwinger equation, necessary for low partial waves, is beset with. A thorough investigation of this kind at N^{3}LO was conducted in Ref. [15]. Here, we will work at N^{4}LO.

The perturbative K-matrix for np scattering is calculated as follows:

$$K(\vec{p}\,',\vec{p}) \quad = \quad V_{1\pi}^{(np)}(\vec{p}\,',\vec{p}) + V_{2\pi,\mathrm{it}}^{(np)}(\vec{p}\,',\vec{p}) + V(\vec{p}\,',\vec{p}) \tag{5.1}$$

with $V_{1\pi}^{(np)}(\vec{p}\,',\vec{p})$ as in Eq. (A.3), and $V_{2\pi,\mathrm{it}}^{(np)}(\vec{p}\,',\vec{p})$ representing the once iterated one-pion exchange (1PE) given by

$$V_{2\pi,\mathrm{it}}^{(np)}(\vec{p}\,',\vec{p}) = \mathcal{P}\!\int d^3p''\, \frac{M_N^2}{E_{p''}}\, \frac{V_{1\pi}^{(np)}(\vec{p}\,',\vec{p}\,'')\, V_{1\pi}^{(np)}(\vec{p}\,'',\vec{p})}{p^2 - p''^2}\,, \tag{5.2}$$

where $\mathcal{P}$ denotes the principal value integral and $E_{p''} = \sqrt{M_N^2 + p''^2}$. A calculation at LO includes only the first term on the right hand side of Eq. (5.1), $V_{1\pi}^{(np)}(\vec{p}\,',\vec{p})$, while calculations at NLO or higher order also include the second term on the right hand side, $V_{2\pi,\mathrm{it}}^{(np)}(\vec{p}\,',\vec{p})$. At N^{3}LO and beyond, the twice iterated 1PE should be included, too. However, we found that the difference between the once iterated 1PE and the infinitely iterated 1PE is so small that it could not be identified on the scale of our phase shift figures. For that reason, we omit iterations of 1PE beyond what is contained in $V_{2\pi,\mathrm{it}}^{(np)}(\vec{p}\,',\vec{p})$.

Finally, the third term on the r.h.s. of Eq. (5.1), $V(\vec{p}\,',\vec{p})$, stands for the irreducible multi-pion exchange contributions that occur at the order at which the calculation is conducted. In multi-pion exchanges, we use the average pion mass $m_\pi = 138.039$ MeV and, thus, neglect the charge-dependence due to pion-mass splitting in irreducible multi-pion diagrams. The charge-dependence that emerges from irreducible 2π exchange was investigated in Ref. [41] and found to be negligible for partial waves with $L \geq 3$.

Throughout this paper, we use

$$M_N = \frac{2M_pM_n}{M_p + M_n} = 938.9182 \text{ MeV}. \tag{5.3}$$

Based upon relativistic kinematics, the CMS on-shell momentum p is related to the kinetic energy of the incident neutron in the laboratory system ("Lab. Energy"), T_{lab}, by

$$p^2 = \frac{M_p^2 T_{\text{lab}}(T_{\text{lab}} + 2M_n)}{(M_p + M_n)^2 + 2T_{\text{lab}}M_p}\,, \tag{5.4}$$

with $M_p = 938.2720$ MeV and $M_n = 939.5653$ MeV the proton and neutron masses, respectively.

The K-matrix, Eq. (5.1), is decomposed into partial waves following Ref. [50] and phase shifts are then calculated via

$$\tan \delta_L(T_{\text{lab}}) = -\frac{M_N^2 p}{16\pi^2 E_p}\, p\, K_L(p,p)\,. \tag{5.5}$$

For more details concerning the evaluation of phase shifts, including the case of coupled partial waves, see Ref. [51] or the appendix of [49]. All phase shifts shown in this paper are in terms of Stapp conventions [54].

5.1.2 N5LO case

Situation with scattering in peripheral partial waves at order N^{5}LO is rather similar to N^{4}LO case. However a few important differences should be pointed out.

First of all, at N^{5}LO new NN contact terms appear, which affect partial waves with orbital momentum $L = 3$. Therefore, predictions in F-waves are no longer parameter free. However, these new contact terms still don't affect G- and higher order partial waves. Thus, predictions in partial waves with $L \geq 4$ are still free of parameters.

Table 5.1: Low-energy constants as determined in Ref. [31]. The sets 'GW' and 'KH' are based upon the πN partial wave analyses of Refs. [55] and [56], respectively. The c_i, $\bar{d}_i$, and $\bar{e}_i$ are in units of GeV^{-1}, GeV^{-2}, and GeV^{-3}.

	GW	KH
c_1	–1.13	–0.75
c_2	3.69	3.49
c_3	–5.51	–4.77
c_4	3.71	3.34
$\bar{d}_1 + \bar{d}_2$	5.57	6.21
$\bar{d}_3$	–5.35	–6.83
$\bar{d}_5$	0.02	0.78
$\bar{d}_{14} - \bar{d}_{15}$	–10.26	–12.02
$\bar{e}_{14}$	1.75	1.52
$\bar{e}_{15}$	–5.80	–10.41
$\bar{e}_{16}$	1.76	6.08
$\bar{e}_{17}$	–0.58	–0.37
$\bar{e}_{18}$	0.96	3.26

Having more pion-exchange contributions at order 6, the K-matrix becomes:

$$K(\vec{p}\,',\vec{p}) = V_{1\pi}^{(np)}(\vec{p}\,',\vec{p}) + V_{2\pi,\mathrm{it}}^{(np)}(\vec{p}\,',\vec{p}) + V_{3\pi,\mathrm{it}}^{(np)}(\vec{p}\,',\vec{p}) + V(\vec{p}\,',\vec{p}) \tag{5.6}$$

where 1st, 2nd and 4th terms are as in section 5.1.1. The 3rd term, $V_{3\pi,\mathrm{it}}^{(np)}(\vec{p}\,',\vec{p})$ stands for terms where irreducible 2PE is iterated with 1PE. At third order and higher, we include the iteration of the NLO 2PE with 1PE and, at fourth order and up, we include the iteration of the NNLO 2PE with 1PE. We find 2PE of higher orders combined with iterative 1PE to be negligible.

5.2 Constants used for peripheral partial waves predictions

Chiral symmetry establishes a link between the dynamics in the πN-system and the NN-system (through common low-energy constants). In order to check the consistency, we use the LECs for subleading πN-couplings as determined in analyses of low-energy elastic πN-scattering. Thus predictions in peripheral partial waves, which are affected by pion-exchange only, should be free of parameters.

It should be noted, that at the time when the work on N^{4}LO and N^{5}LO pion-exchange contributions was done, the set of Roy-Steiner LECs (Table 2.1) did not exist yet. An older set of LECs was used at the time. Analyses from which those LECs were derived are contained in Refs. [31, 57], where πN-scattering has been calculated at 4th order using the same power-counting of relativistic

$1/M_N$-corrections as in the present work. Ref. [31] performed two fits, one to the GW [55] and one to the KH [56] partial wave analysis resulting in the two sets of LECs listed in Table 5.1. N^{4}LO predictions in this work were carried out with KH set of LECs, while GW set was used for N^{5}LO. Both 5th and 6th order predictions were later recalculated with Roy-Steiner LECs, when the latter became available, and the difference was found negligible. Therefore, in subsequent sections 5.3 and 5.3, the older version of results is presented as published in Refs. [37, 39].

Also, we absorb the Goldberger-Treiman discrepancy into an effective value of the nucleon axial-vector coupling constant $g_A = g_{\pi NN} f_\pi / M_N = 1.29$. Finally, the physical value of the pion-decay constant is $f_\pi = 92.4$ MeV (see Table 2.2).

5.3 Summary of N4LO results

As shown in Figs. 3.1 and 3.2 and derived in Ch. 3, the fifth order consists of several contributions. We will now demonstrate how the individual fifth-order contributions impact NN phase shifts in peripheral waves. For this purpose, we display in Fig. 5.1 phase shifts for six important peripheral partial waves, namely, $^1F_3$, $^3F_2$, $^3F_3$, $^3F_4$, $^1G_4$, and $^3G_5$. In each frame, the following curves are shown:

(1) N^{3}LO.

(2) The previous curve plus the c_i/M_N corrections (denoted by 'c/M'), Fig. 3.1(c) and Sec. 3.1.3.

(3) The previous curve plus the N^{4}LO 2π-exchange (2PE) two-loop contributions of class (a), Fig. 3.1(a) and Sec. 3.1.1.

(4) The previous curve plus the N^{4}LO 2PE two-loop contributions of class (b), Fig. 3.1(b) and Sec. 3.1.2.

(5) The previous curve plus the N^{4}LO 3π-exchange (3PE) contributions, Fig. 3.2 and Sec. 3.2.

In summary, the various curves add up successively the individual N^{4}LO contributions in the order indicated in the curve labels. The last curve in this series, curve (5), is the full N^{4}LO result. In these calculations, a SFR cutoff $\tilde{\Lambda} = 1.5$ GeV is applied [cf. Eq. (2.18)].

From Fig. 5.1, we make the following observations. In triplet F-waves, the c_i/M_N corrections as well as the 2PE two-loops, class (a) and (b), are all repulsive and of about the same strength. As a consequence, the problem of the excessive attraction, that N^{3}LO is beset with, is overcome.

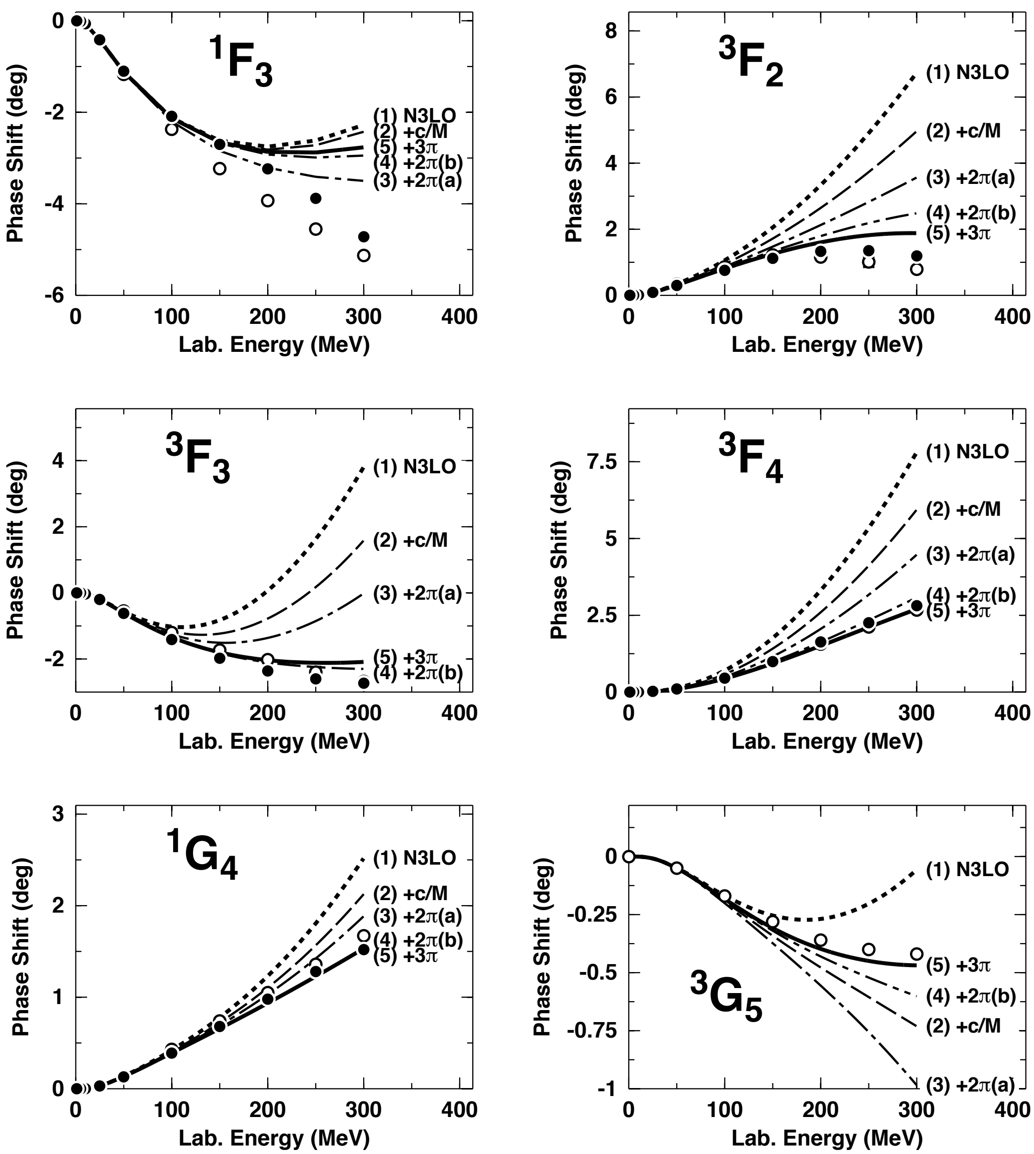

Figure 5.1: Effect of individual fifth-order contributions on the neutron-proton phase shifts of some selected peripheral partial waves. The individual contributions are added up successively in the order given in parenthesis next to each curve. Curve (1) is N3LO and curve (5) is the complete N4LO. The filled and open circles represent the results from the Nijmegan multi-energy *np* phase-shift analysis [58] and the VPI/GWU single-energy *np* analysis SM99 [59], respectively.

A similar trend is seen in ${}^1G_4$. An exception is ${}^1F_3$, where the class (b) contribution is attractive leading to phase shifts above the data for energies higher than 150 MeV.

Now turning to the N^{4}LO 3PE contributions [curve (5) in Fig. 5.1]: they are substantially smaller than the 2PE two-loop ones, in all peripheral partial waves. This can be interpreted as an indication of convergence with regard to the number of pions being exchanged between two nucleons—a trend that is very welcome. Further, note that the total 3PE contribution is a very comprehensive one, cf. Fig. 3.2. It is the sum of ten terms (cf. Sec. 3.2) which, individually, can be fairly large. However, destructive interference between them leads to the small net result.

For all F and G waves (except ${}^1F_3$), the final N^{4}LO result is in excellent agreement with the empirical phase shifts. Notice that this includes also ${}^3G_5$, which posed persistent problems at N^{3}LO [15].

On a historical note, we mention that in the construction of the Stony Brook [60, 61] and Paris [62, 63] NN potentials, which both include a 2PE contribution based upon dispersion theory, the dispersion integral, Eq. (2.18), is cutoff at $\mu^2 = 50\, m_\pi^2$, which is equivalent to a SFR cutoff $\tilde{\Lambda} = \sqrt{50}\, m_\pi \sim 1$ GeV. Not accidentally, this agrees well with the common assumption of $\Lambda_\chi \sim 1$ GeV and, thus, sets the scale for an appropriate choice of $\tilde{\Lambda}$. Consistent with this, $\tilde{\Lambda} = 1.5$ GeV was used for the results presented in Fig. 5.1. It is, however, also of interest to know how predictions change with variations of $\tilde{\Lambda}$ within a reasonable range. We have, therefore, varied $\tilde{\Lambda}$ between 0.7 and 1.5 GeV and show the predictions for all F and G waves in Figs. 5.2 and 5.3, respectively, in terms of shaded (colored) bands. It is seen that, at N^{3}LO, the variations of the predictions are very large and always too attractive while, at N^{4}LO, the variations are small and the predictions are close to the data or right on the data. Figs. 5.2 and 5.3 also include the lower orders (as defined in the Appendices) such that a comparison of the relative size of the order-by-order contributions is possible. We observe that there is not much of a convergence, since obviously the magnitudes of the NNLO, N^{3}LO, and N^{4}LO contributions are about the same. Therefore, to test convergence, one needs to calculate the effect of N^{5}LO explicitly, which is done in the subsequent section.

5.4 Summary of N5LO results

6th order corrections also consists of several contributions, as shown in Figs. 4.1 to 4.3 and derived in Ch. 4. We will now demonstrate how the individual sixth-order contributions impact NN-phase-shifts in peripheral waves. Note, that we have to start with G-waves, since F-waves are no longer parameter-free (see explanation of Eq. 2.28). We display in Fig. 5.4 phase-shifts for two peripheral

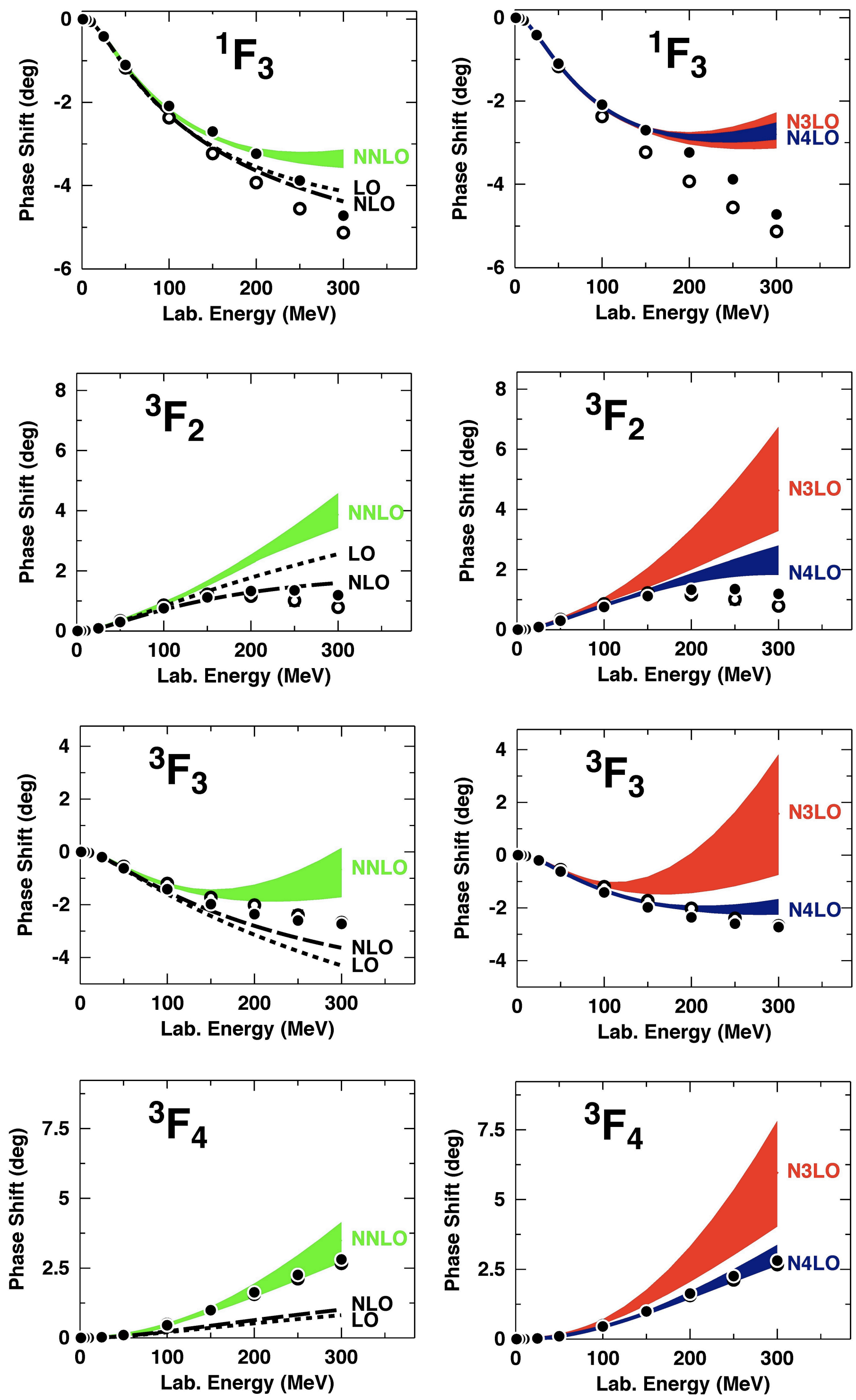

Figure 5.2: (Color online) Phase-shifts of neutron-proton scattering at various orders as denoted. The shaded (colored) bands show the variation of the predictions when the SFR cutoff $\tilde{\Lambda}$ is changed over the range 0.7 to 1.5 GeV. The filled and open circles represent the results from the Nijmegan multi-energy *np* phase-shift analysis [58] and the VPI/GWU single-energy *np* analysis SM99 [59], respectively.

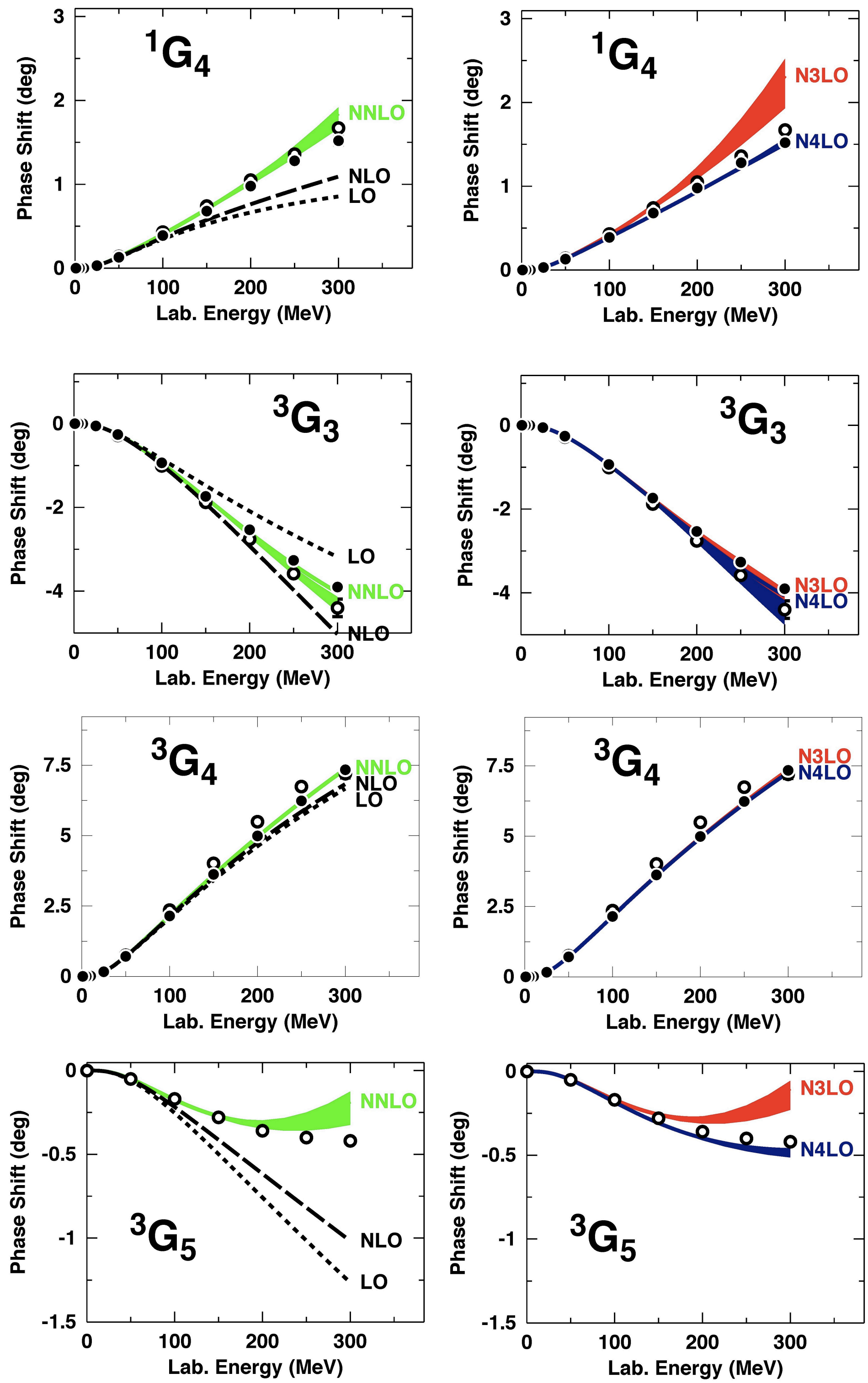

Figure 5.3: (Color online) Same as Fig. 5.2, but for G-waves.

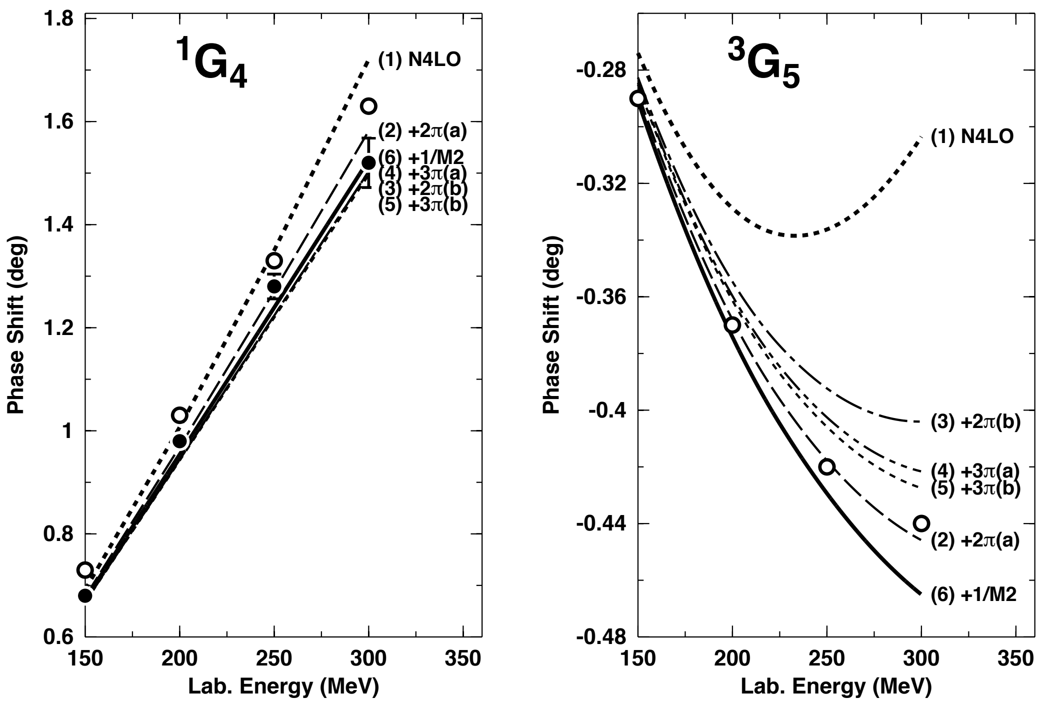

Figure 5.4: Effect of individual sixth-order contributions on the neutron-proton phase shifts of two G-waves. The individual contributions are added up successively in the order given in parentheses next to each curve. Curve (1) is N^{4}LO and curve (6) contains all N^{5}LO contributions calculated in this work. A SFR cutoff $\tilde{\Lambda} = 800$ MeV is applied. The filled and open circles represent the results from the Nijmegen multi-energy np phase-shift analysis [58] and the GWU np-analysis SP07 [64], respectively.

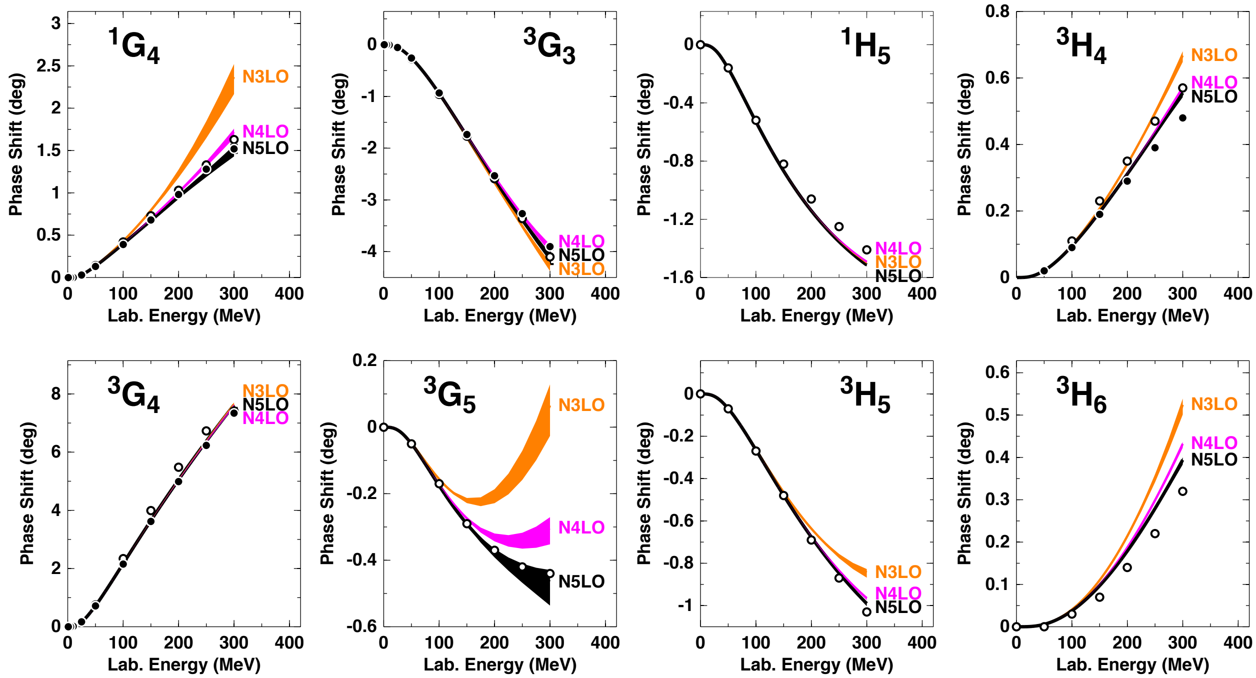

Figure 5.5: (Color online) Phase-shifts of neutron-proton scattering in G and H waves at various orders as denoted. The shaded (colored) bands show the variations of the predictions when the SFR cutoff $\tilde{\Lambda}$ is changed over the range 700 to 900 MeV. Empirical phase shifts are as in Fig. 5.4.

partial waves, namely, $^1G_4$, and $^3G_5$. In each frame, the following curves are shown:

(1) N^{4}LO (as defined in Ref. [37]).

(2) The previous curve plus the N^{5}LO 2π-exchange contributions of class (a), Fig. 4.1(a) and Sec. 4.1.1.

(3) The previous curve plus the N^{5}LO 2π-exchange contributions of class (b), Fig. 4.1(b) and Sec. 4.1.2.

(4) The previous curve plus the N^{5}LO 3π-exchange contributions of class (a), Fig. 4.3(a) and Sec. 4.2.1.

(5) The previous curve plus the N^{5}LO 3π-exchange contributions of class (b), Fig. 4.3(b) and Sec. 4.2.2.

(6) The previous curve plus the $1/M_N^2$-corrections (denoted by '1/M2'), Fig. 4.2 and Sec. 4.1.4.

In summary, the various curves add up successively the individual N^{5}LO contributions in the order indicated by the curve labels. The last curve in this series, curve (6), includes all N^{5}LO contributions calculated in this paper. For all curves of this figure a SFR cutoff $\tilde{\Lambda} = 800$ MeV [cf. Eq. (2.19)] is employed.

From Fig. 5.4, we make the following observations. The two-loop 2π-exchange class (a), Fig. 4.1(a), generates a strong repulsive central force through the spectral function Eq. (4.1), while the spin-spin and tensor forces provided by this class, Eq. (4.2), are negligible. The fact that this class produces a relatively large contribution is not unexpected, since it is proportional to c_i^2. The 2π-exchange contribution class (b), Fig. 4.1(b), creates a moderately repulsive central force as seen by its effect on $^1G_4$ and a noticeable tensor force as the impact on $^3G_5$ demonstrates. The 3π-exchange class (a), Fig. 4.3(a), is negligible in $^1G_4$, but noticeable in $^3G_5$ and, therefore, it should not be neglected. This contribution is proportional to c_i^2, which suggests a non-negligible size but it is typically smaller than the corresponding 2π-exchange contribution class (a). The 3π-exchange class (b) contribution, Fig. 4.3(b), turns out to be negligible [see the difference between curve (4) and (5) in Fig. 5.4]. This may not be unexpected since it is a three-loop contribution with only leading-order vertices. Finally the relativistic $1/M_N^2$-corrections to the leading 2π-exchange, Fig. 4.2, have a small but non-negligible impact, particularly in $^3G_5$.

The predictions for all G and H waves, are displayed in Fig. 5.5 in terms of shaded (colored) bands that are generated by varying the SFR cutoff $\tilde{\Lambda}$ [cf. Eq. (2.19)] between 700 and 900

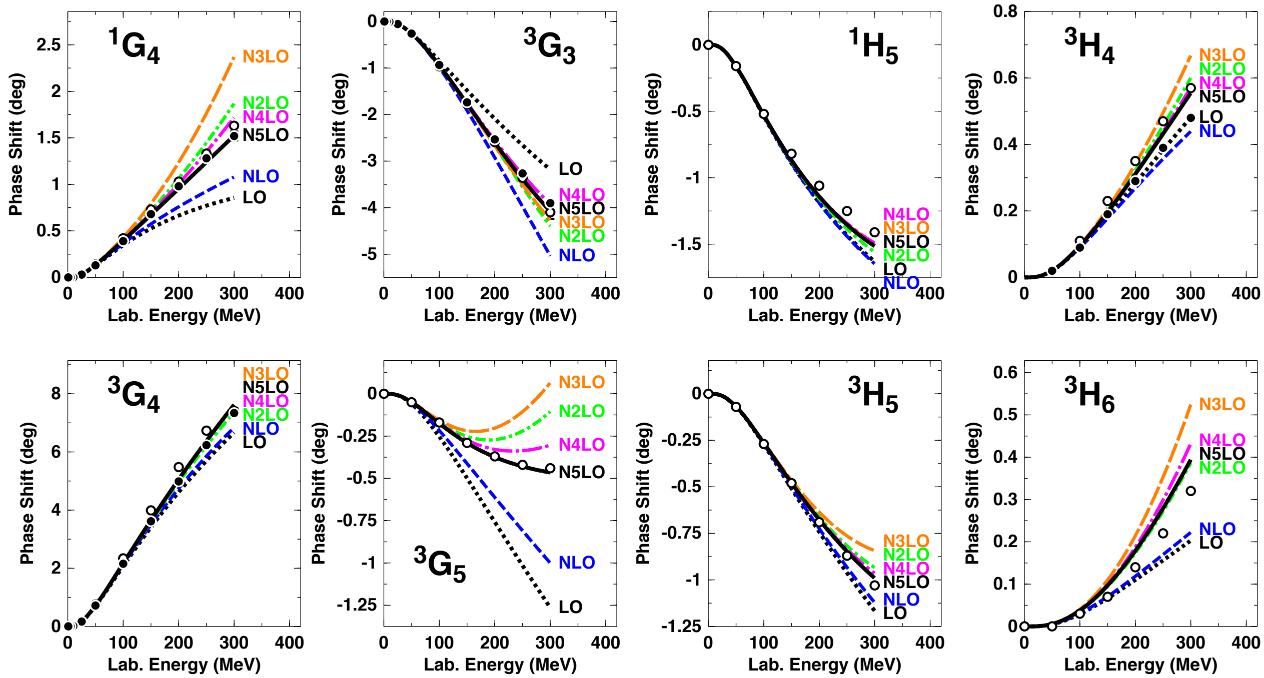

Figure 5.6: (Color online) Phase-shifts of neutron-proton scattering in G and H waves at all orders from LO to N^{5}LO. A SFR cutoff $\tilde{\Lambda} = 800$ MeV is used. Empirical phase shifts are as in Fig. 5.4.

MeV. The figure clearly reveals that, at N^{3}LO, the predictions are, in general, too attractive. As demonstrated in Ref. [37], the N^{4}LO contribution, essentially, compensates this attractive surplus. Now, let us turn to the new result at N^{5}LO: it shows a moderate repulsive contribution bringing the final prediction right onto the data (i.e. empirical phase-shifts). Moreover, the N^{5}LO contribution is, in general, substantially smaller than the one at N^{4}LO, thus, showing a signature of convergence of the chiral expansion.

Concerning the $^3G_5$ phase shifts, a comment is in place. From Fig. 5.5 , it may appear that in this case the order-by-order convergence pattern is poor and the spread as a function of $\tilde{\Lambda}$ rather large and not skrinking with increasing order. Notice, however, that we are talking here about very small numbers: the whole phase shift scale of the $^3G_5$ frame is 0.8 deg and the spread as a function of $\tilde{\Lambda}$ is about 0.1 deg in each order. Moreover, the $^3G_5$ is known to be exceptionally sensitive to dynamics at medium-to-short range. This has been noticed and discussed before, see, e.g., Ref. [15].

We also like to comment on the empirical phase shifts with which we compare our predictions in Figs. 5.4 to 5.7. We use the 1993 Nijmegen analysis [58] (represented by filled circles in the figures) and the GWU analysis from summer 2007 [64] (open circles). We have also considered

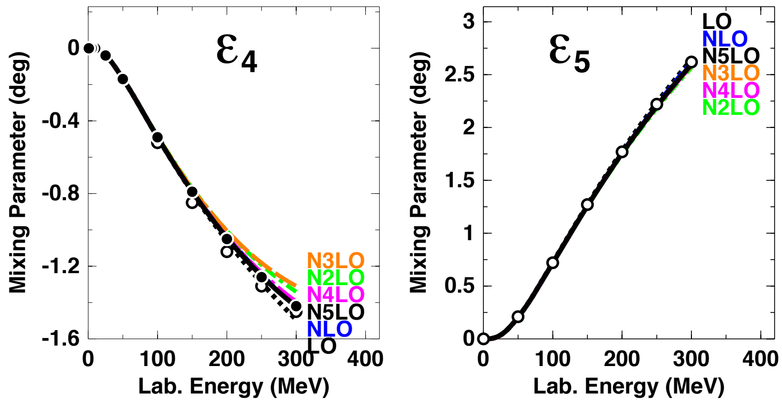

Figure 5.7: (Color online) Mixing angles for neutron-proton scattering for $J = 4, 5$ at all orders from LO to N^{5}LO. A SFR cutoff $\tilde{\Lambda} = 800$ MeV is used. Filled and open circles are as in Fig. 5.4.

the recent Granada NN-analysis [65]. However, it turned out that, in general, the Granada and Nijmegen analyses are so close to each other that it does not make sense to show them separately. Concerning a second analysis, we decided for GWU [64] for two reasons. The GWU analysis is truly alternative to Nijmegen (and Granada), because it is not performed with a cleaned-up data base; it uses the full NN-data base. Moreover, the GWU analysis provides empirical phase shifts also for partial waves with $J = 5, 6$, which we need. (The Nijmegen and Granada analyses stop at $J = 4$.)

Figure 5.5 includes only the three highest orders. However, a comparison between all orders is also of interest. Therefore, we show in Figs. 5.6 the contributions to phase shifts through all six chiral orders from LO to N^{5}LO (as defined in Ref. [37] and the present paper). Note that the difference between the LO prediction (one-pion-exchange, dotted line) and the data (filled and open circles) is to be provided by two- and three-pion exchanges, i.e. the intermediate-range part of the nuclear force. How well that is accomplished is a crucial test for any theory of nuclear forces. NLO produces only a small contribution, but N^{2}LO creates substantial intermediate-range attraction (most clearly seen in $^1G_4$, $^3G_5$, and $^3H_6$). In fact, N^{2}LO is the largest contribution among all orders. This is due to the one-loop 2π-exchange (2PE) triangle diagram which involves one $\pi\pi NN$-contact vertex proportional to c_i. This vertex represents correlated 2PE as well as intermediate $\Delta(1232)$-isobar excitation. It is well-known from the traditional meson theory of nuclear forces [66, 62, 63] that these two features are crucial for a realistic and quantitative 2PE model. Consequently, the one-loop 2π-exchange at N^{2}LO is attractive and assumes a realistic size describing the intermediate-range attraction of the nuclear force about right. At N^{3}LO, more one-loop 2PE is added by the bubble diagram with two c_i-vertices, a contribution that seemingly is overestimating the attraction. This attractive surplus is then compensated by the prevailingly repulsive two-loop 2π- and 3π-exchanges that occur at N^{4}LO and N^{5}LO.

In this context, it is worth to note that also in conventional meson theory [66] the one-loop models for the 2PE contribution always show some excess of attraction (cf. Figs. 7-9 of Ref. [15]). The same is true for the dispersion theoretic approach pursued by the Paris group [62, 63]. In conventional meson theory, the surplus attraction is reduced by heavy-meson exchange (ρ- and ω-exchange) which, however, has no place in chiral effective field theory (as a finite-range contribution). Instead, in the latter approach, two-loop 2π- and 3π-exchanges provide the corrective action.

We now turn to Figs. 5.7, where we show how the six chiral orders impact the mixing angles with $J = 4, 5$. Note that the mixing angles depend only on the tensor force (the quadratic spin-orbit term $V_{\sigma L}$ in Eq.(4.14) is very small). It is clearly seen that the 1π-exchange (LO) alone describes these mixing angles correctly and that the various higher orders make only negligible contributions, particularly, for $J = 5$. At any order in the chiral expansion, tensor forces are created, but obviously the tensor force contributions beyond LO are of shorter range such that they do not matter in peripheral waves with $L \geq 4$.

Finally, to summarize this section, it should be pointed out that according to presented calculations the contribution at N^{5}LO is substantially smaller than the one at N^{4}LO, thus, indicating a signature of convergence. Based on this and the fact that calculations at N^{4}LO already produce good agreement with experiment, one may argue that for practical purpose of constructing full NN potential calculations up to N^{4}LO should be enough. I proceed to summarize the results of this construction in the next chapter.

CHAPTER 6

Full nucleon-nucleon potential at N4LO

Based upon the formalism presented in chapter 2, we have constructed NN potentials through five orders of the chiral expansion, ranging from LO (Q^0) to N^{4}LO (Q^5). In each order, we consider three cutoffs, namely, $\Lambda = 450$, 500, and 550 MeV. Since we take charge-dependence into account, each NN potential comes in three versions: *pp*, *np*, and *nn*. The results from these potentials for NN scattering and the deuteron will be presented in this chapter (also see Ref [38]).

6.1 NN database

Since an important part of NN potential construction involves optimizing the reproduction of the NN data by the potential, we need to state, first, what NN database we are using.

Our database consists of all NN data below 350 MeV laboratory energy published in refereed physics journals between January 1955 and December 2016 that are not discarded when applying the Nijmegen rejection criteria [46]. We will refer to this as the "2016 database". This database was started by the Nijmegen group who critically checked and assembled the data published up to December 1992. This 1992 database consists of 1787 *pp* data (listed in Ref. [67]) and 2514 *np* data (tabulated in Ref. [58]), cf. Table 6.1. In Ref. [49], the database was then extended to include the data published up to December 1999 that survived the Nijmegen rejection criteria. This added 1145 *pp* and 544 *np* data (given in Tables XV and XVI of Ref. [49], respectively). Thus, the 1999 database includes 2932 *pp* and 3058 *np* data.

To get to the 2016 database, we have added to the 1999 database the data published between January 2000 and December 2016 that are not rejected by the Nijmegen criteria. We are aware of the fact that modified rejection criteria have been proposed [81] and applied in recent NN data analysis work [65]. But we continue to apply the classic Nijmegen criteria [46] to be consistent with

Table 6.1: Publication history of the NN data below 350 MeV laboratory energy and references for their listings. Only data that pass the Nijmegen acceptance criteria [46] are counted. 'Total' defines the 2016 database.

Publication date	No. of *pp* data	No. of *np* data	References
Jan. 1955 – Dec. 1992	1787	2514	[67, 58]
Jan. 1993 – Dec. 1999	1145	544	Tables XV and XVI of Ref. [49]
Jan. 2000 – Dec. 2016	140	511	Ref. [68] and Table 6.2 of present paper
Total	3072	3569	

Table 6.2: After-1999 np data below 350 MeV included in the 2016 np database. "Error" refers to the normalization error. This table contains 473 observables plus 38 normalizations resulting in a total of 511 data. For the observables, we use in general the notation of Hoshizaki [69], except for types which are undefined in the Hoshizaki formalism, where we use the Saclay notation [70].

T_{lab} (MeV)	No. type	Error (%)	Institution	Ref.
9.2–349.0	92 σ_{tot}	None	Los Alamos	[71]
10.0	6 σ	0.8	Ohio	[72]
95.0	10 σ	5.0	Uppsala	[73]
95.0	9 σ	4.0	Uppsala	[74]
96.0	11 σ	5.0	Uppsala	[75]
96.0	9 σ	3.0	Uppsala	[76]
96.0	12 σ	None	Uppsala	[77]
260.0	8 P	1.8	PSI	[78]
260.0	16 P	1.8	PSI	[78]
260.0	8 A_{yy}	3.9	PSI	[78]
260.0	16 A_{yy}	3.9	PSI	[78]
260.0	9 A_{zz}	7.2	PSI	[78]
260.0	5 D	2.4	PSI	[79]
260.0	8 D	Float	PSI	[79]
260.0	8 $D_{0s''0k}$	Float	PSI	[79]
260.0	5 D_t	2.4	PSI	[79]
260.0	4 A_t	2.4	PSI	[79]
260.0	8 A_t	2.4	PSI	[79]
260.0	4 R_t	2.4	PSI	[79]
260.0	8 R_t	2.4	PSI	[79]
260.0	8 N_{0nkk}	2.4	PSI	[79]
260.0	4 $N_{0s''kn}$	2.4	PSI	[79]
260.0	8 $N_{0s''kn}$	2.4	PSI	[79]
260.0	4 $N_{0s''sn}$	2.4	PSI	[79]
260.0	8 $N_{0s''sn}$	2.4	PSI	[79]
284.0	14 P	3.0	PSI	[80]
314.0	14 P	3.0	PSI	[80]
315.0	16 P	1.2	PSI	[78]
315.0	11 A_{yy}	3.7	PSI	[78]
315.0	16 A_{yy}	3.7	PSI	[78]
315.0	11 A_{zz}	7.1	PSI	[78]
315.0	6 D	Float	PSI	[79]
315.0	6 $D_{0s''0k}$	Float	PSI	[79]
315.0	8 $D_{0s''0k}$	Float	PSI	[79]
315.0	6 D_t	1.9	PSI	[79]
315.0	6 A_t	1.9	PSI	[79]
315.0	8 A_t	1.9	PSI	[79]
315.0	6 R_t	1.9	PSI	[79]
315.0	8 R_t	1.9	PSI	[79]
315.0	5 $N_{0s''kn}$	1.9	PSI	[79]
315.0	8 $N_{0s''kn}$	1.9	PSI	[79]
315.0	6 $N_{0s''sn}$	1.9	PSI	[79]
315.0	8 $N_{0s''sn}$	1.9	PSI	[79]
315.0	8 N_{0nkk}	1.9	PSI	[79]
344.0	14 P	3.0	PSI	[80]

Table 6.3: χ^2/datum for the fit of the 2016 NN data base by NN potentials at various orders of chiral EFT ($\Lambda = 500$ MeV in all cases).

T_{lab} bin (MeV)	No. of data	LO	NLO	NNLO	N^{3}LO	N^{4}LO
			proton-proton			
0–100	795	520	18.9	2.28	1.18	1.09
0–190	1206	430	43.6	4.64	1.69	1.12
0–290	2132	360	70.8	7.60	2.09	1.21
			neutron-proton			
0–100	1180	114	7.2	1.38	0.93	0.94
0–190	1697	96	23.1	2.29	1.10	1.06
0–290	2721	94	36.7	5.28	1.27	1.10
			pp **plus** ***np***			
0–100	1975	283	11.9	1.74	1.03	1.00
0–190	2903	235	31.6	3.27	1.35	1.08
0–290	4853	206	51.5	6.30	1.63	1.15

the pre-2000 part of the database.

Concerning after-1999 *pp* data, there exists only one set of 139 differential cross sections between 239.9 and 336.2 MeV measured by the EDDA group at COSY (Júlich, Germany) with an over-all uncertainty of 2.5% [68]. Thus, the total number of *pp* data contained in the 2016 database is 3072 (Table 6.1).

In contrast to *pp*, there have been many new *np* measurements after 1999. We list the datasets that survived the Nijmegen rejection criteria in Table 6.2. According to that list, the number of valid after-1999 *np* data is 511, bringing the total number of *np* data contained in the 2016 database to 3569 (Table 6.1).

For comparison, we mention that the 2013 Granada NN database [65] consists of 2996 *pp* and 3717 *np* data. The larger number of *pp* data in our base is mainly due to the inclusion of 140 *pp* data from Ref. [68] which are left out in the Granada base. On the other hand, the Granada base contains 148 more *np* data which is a consequence of the modified rejection criteria applied by the Granada group which allows for the survival of more *np* data. We believe that the small differences between our 2016 database and the Granada 2013 base will affect χ^2 calculations only to negligible degree.

Finally, we note that in the potential construction reported in this study, we make use of the 2016 database only up to 290 MeV laboratory energy (pion-production threshold). Between 0 and 290 MeV, the 2016 database contains 2132 *pp* data and 2721 *np* data (cf. Table 6.3).

Table 6.4: Scattering lengths (a) and effective ranges (r) in units of fm as predicted by NN potentials at various orders of chiral EFT ($\Lambda = 500$ MeV in all cases). (a^C_{pp} and r^C_{pp} refer to the pp parameters in the presence of the Coulomb force. a^N and r^N denote parameters determined from the nuclear force only and with all electromagnetic effects omitted.) a^N_{nn}, and a_{np} are fitted, all other quantities are predictions.

	LO	NLO	NNLO	N^{3}LO	N^{4}LO	Empirical
			$^1S_0$			
a^C_{pp}	−7.8153	−7.8128	−7.8140	−7.8155	−7.8160	−7.8196(26) [46]
						−7.8149(29) [82]
r^C_{pp}	1.886	2.678	2.758	2.772	2.774	2.790(14) [46]
						2.769(14) [82]
a^N_{pp}	—	−17.476	−17.762	−17.052	−17.123	—
r^N_{pp}	—	2.752	2.821	2.851	2.853	—
a^N_{nn}	−18.950	−18.950	−18.950	−18.950	−18.950	−18.95(40) [83, 84]
r^N_{nn}	1.857	2.726	2.800	2.812	2.816	2.75(11) [85]
a_{np}	−23.738	−23.738	−23.738	−23.738	−23.738	−23.740(20) [49]
r_{np}	1.764	2.620	2.687	2.700	2.704	[2.77(5)] [49]
			$^3S_1$			
a_t	5.255	5.415	5.418	5.420	5.420	5.419(7) [49]
r_t	1.521	1.755	1.752	1.754	1.753	1.753(8) [49]

Table 6.5: Two- and three-nucleon bound-state properties as predicted by NN potentials at various orders of chiral EFT ($\Lambda = 500$ MeV in all cases). (Deuteron: Binding energy B_d, asymptotic S state A_S, asymptotic D/S state η, structure radius r_{str}, quadrupole moment Q, D-state probability P_D; the predicted r_{str} and Q are without meson-exchange current contributions and relativistic corrections. Triton: Binding energy B_t.) B_d is fitted, all other quantities are predictions.

	LO	NLO	NNLO	N^{3}LO	N^{4}LO	Empirical[a]
Deuteron						
B_d (MeV)	2.224575	2.224575	2.224575	2.224575	2.224575	2.224575(9)
A_S (fm$^{-1/2}$)	0.8526	0.8828	0.8844	0.8853	0.8852	0.8846(9)
η	0.0302	0.0262	0.0257	0.0257	0.0258	0.0256(4)
r_{str} (fm)	1.911	1.971	1.968	1.970	1.973	1.97507(78)
Q (fm^2)	0.310	0.273	0.273	0.271	0.273	0.2859(3)
P_D (%)	7.29	3.40	4.49	4.15	4.10	—
Triton						
B_t (MeV)	11.02	8.31	8.21	8.09	8.08	8.48

[a] See Table XVIII of Ref. [49] for references; the empirical value for r_{str} is from Ref. [86].

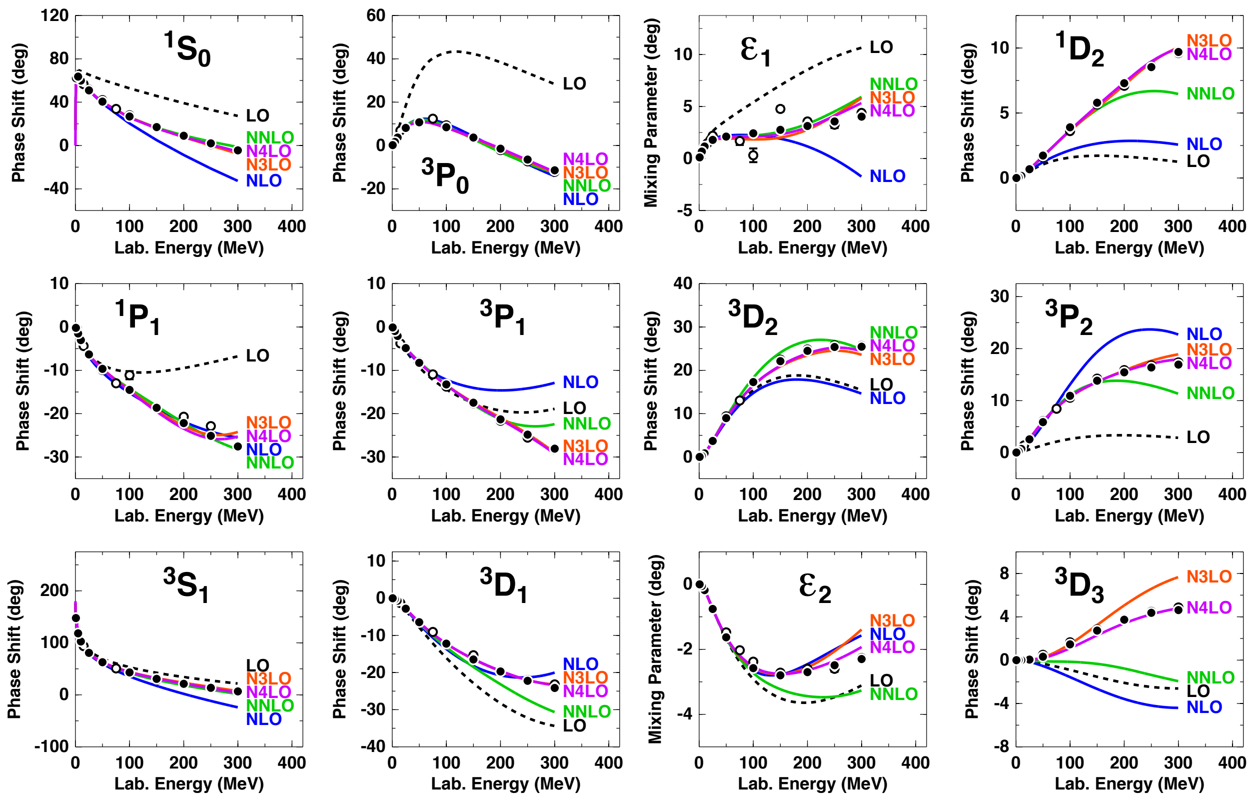

Figure 6.1: (Color online). Chiral expansion of neutron-proton scattering as represented by the phase shifts in S, P, and D waves and mixing parameters ϵ_1 and ϵ_2. Five orders ranging from LO to N^{4}LO are shown as denoted. A cutoff $\Lambda = 500$ MeV is applied in all cases. The filled and open circles represent the results from the Nijmegen multi-energy np phase-shift analysis [58] and the GWU single-energy np analysis SP07 [64], respectively.

6.2 Data fitting procedure

When we are talking about data fitting, we are referring to the adjustment of the NN contact parameters available at the respective order. Note that in our NN potential construction, the πN LECs are not fit-parameters. The πN LECs are held fixed at their values determined in the πN analysis of Ref. [44] displayed in Table 2.1 (we use the central values shown in that Table). Thus, the NN contacts (Sec. 2.2.4) are the only fit parameters used to optimize the reproduction of the NN data below 290 MeV laboratory energy. As discussed, those contact terms describe the short-range part of the NN potentials and adjust the lower partial waves.

In the construction of any NN potential, we always start with the pp version since the pp data are the most accurate ones. The fitting is done in three steps. In the first step, the pp potential is adjusted to reproduce as closely as possible the *pp* phase shifts of the Nijmegen multienergy *pp* phase shift analysis [58] up to 300 MeV laboratory energy. This is to ensure that phase shifts are in the right ballpark. In the second step, we make use of the Nijmegen *pp* error matrix [87] to minimize the χ^2 that results from it. The advantage of this step is that it is computationally very fast and easy. Finally, in the third and final step, the *pp* potential contact parameters are fine-tuned by minimizing the χ^2 that results from a direct comparison with the experimental *pp* data contained in the 2016 database below 290 MeV. For this we use a copy of the SAID software package which includes all electromagnetic contributions necessary for the calculation of NN observables at low energy. Since it turned out that the Nijmegen error matrix produces very accurate χ^2 for *pp* energies below 75 MeV, we use the values from this error matrix for the energies up to 75 MeV and the values from a direct confrontation with the data above that energy.

The $I = 1$ *np* potential is constructed by starting from the *pp* version, applying the charge-dependence discussed in Sec. 2.2.5, and adjusting the non-derivative $^1S_0$ contact such as to reproduce the $^1S_0$ *np* scattering length. This then yields the preliminary fit of the $I = 1$ *np* potential. The preliminary fit of the $I = 0$ *np* potential is obtained by a fit to the $I = 0$ *np* phase shifts of the Nijmegen multienergy *np* phase shift analysis [58] below 300 MeV. Starting from this preliminary *np* fit, the contact parameters are fine-tuned in a confrontation with the *np* data below 290 MeV, for which the χ^2 is minimized. We note that during this last step we have also allowed for minor changes of the $I = 1$ parameters (which also modifies the *pp* potential) to obtain an even lower χ^2 over-all.

Finally the *nn* potential is obtained by starting from the *pp* version, replacing the proton masses by neutron masses, leaving out Coulomb, and adjusting the non-derivative $^1S_0$ contact such as to reproduce the $^1S_0$ *nn* scattering length for which we assume the empirical value of -18.95 MeV[83, 84].

6.3 Numerical algorithms

A few words should be said about numerical optimization algorithms used for fitting NN contact parameters.

For the 1st and 2nd step in section 6.2, Levenberg-Marquardt (LM) algorithm was used [88, 89].

Due to some limitations of SAID code (use of single precision variables), Nelder-Mead (otherwise known as "downhill simplex" [90]) algorithm was chosen for step 3. While it may converge slower than LM algorithm, it does not require calculation of Jacobian of optimization target function.

This avoids problems with rounding errors, when using very small steps for numerical evaluation of the Jacobian with single precision. In practice, the rate of convergence of Nelder-Mead algorithm turned out to be acceptable.

It should be also mentioned, that while theoretically step one of pre-fitting parameters to phase shifts seems optional, in practice it's a rather crucial one. Most numerical optimization algorithms (including LM and Nelder-Mead) search for the local minimum of the target function. As may be expected, the 26-dimentional landscape of the target function of 25 variables (NN contact parameters) is quite complex. Therefore successfully picking initial guess point for all 25 parameters is virtually impossible. On the other hand, when doing pre-fitting of parameters to phase shifts, one only needs to fit a few parameters at a time (no more than 8, usually 4 or less). As a result one gets a good estimate for the starting point for 3rd step , when all 25 parameters are varied simultaneously. This is because the optimal data fit roughly corresponds to optimal fit of phase shifts.

6.4 Results for NN scattering

The χ^2/datum for the reproduction of the NN data at various orders of chiral EFT are shown in Table 6.3 for different energy intervals below 290 MeV laboratory energy (T_{lab}). The bottom line of Table 6.3 summarizes the essential results. For the close to 5000 *pp* plus *np* data below 290 MeV (pion-production threshold), the χ^2/datum is 51.4 at NLO and 6.3 at NNLO. Note that the number of NN contacts terms is the same for both orders. The improvement is entirely due to an improved description of the 2PE contribution, which is responsible for the crucial intermediate-range attraction of the nuclear force. At NLO, only the uncorrelated 2PE is taken into account which is insufficient. From the classic meson-theory of nuclear forces [66], it is wellknown that π-π correlations and nucleon resonances need to be taken into account for a realistic model of 2PE that provides a sufficient amount of intermediate attraction to properly bind nucleons in nuclei. In the chiral theory, these contributions are encoded in the subleading πN vertexes with LECs denoted by c_i. These enter at NNLO and are the reason for the substantial improvements we encounter at that order. This is the best proof that, starting at NNLO, the chiral approach to nuclear forces is getting the physics right.

To continue on the bottom line of Table 6.3, after NNLO, the χ^2/datum then further improves to 1.63 at N^{3}LO and, finally, reaches the almost perfect value of 1.15 at N^{4}LO—a fantastic convergence.

Corresponding *np* phase shifts are displayed in Fig. 6.1, which reflect what the χ^2 have already proven, namely, an excellent convergence when going from NNLO to N^{3}LO and, finally, to N^{4}LO. The phase shift plots also make it clear that the nuclear force at LO is very wrong and at NLO very poor, to say the least. This fact renders applications of the LO and NLO nuclear force useless for any realistic calculation (but they could be used to demonstrate truncation errors).

For order N^{4}LO (with $\Lambda = 500$ MeV), we also provide the numerical values for the phase shifts in Appendix B. Our *pp* phase shifts are the phase shifts of the nuclear plus relativistic Coulomb interaction with respect to Coulomb wave functions. Note, however, that for the calculation of observables (e.g., to obtain the χ^2 in regard to experimental data), we use electromagnetic phase shifts, as *necessary*, which we obtain by adding to the Coulomb phase shifts the effects from two-photon exchange, vacuum polarization, and magnetic moment interactions as calculated by the Nijmegen group [46, 91]. This is important for $^1S_0$ below 30 MeV and negligible otherwise. For *nn* and *np* scattering, our phase shifts are the ones from the nuclear interaction with respect to Riccati-Bessel functions. The technical details of our phase shift calculations can be found in appendix A3 of Ref. [49].

The low-energy scattering parameters, order by order, are shown in Table 6.4. For *nn* and *np*, the effective range expansion without any electromagnetic interaction is used. In the case of *pp* scattering, the quantities a^C_{pp} and r^C_{pp} are obtained by using the effective range expansion appropriate in the presence of the Coulomb force (cf. appendix A4 of Ref. [49]). Note that the empirical values for a^C_{pp} and r^C_{pp} in Table 6.4 were obtained by subtracting from the corresponding electromagnetic values the effects due to two-photon exchange and vacuum polarization. Thus, the comparison between theory and experiment for these two quantities is conducted correctly. a^N_{nn}, and a_{np} are fitted, all other quantities are predictions. Note that the $^3S_1$ effective range parameters a_t and r_t are not fitted. But the deuteron binding energy is fitted (cf. next subsection) and that essentially fixes a_t and r_t.

6.5 Deuteron and triton

Deuteron properties for all orders of chiral EFT are shown in Table 6.5. In all cases, we fit the deuteron binding energy to its empirical value of 2.224575 MeV using the non-derivative $^3S_1$ contact. All other deuteron properties are predictions. Already at NNLO, the deuteron has converged to its empirical properties and stays there through the higher orders.

At the bottom of Table 6.5, we also show the predictions for the triton binding as obtained in 34-channel charge-dependent Faddeev calculations using only 2NFs. The results show smooth and

Table 6.6: χ^2/datum for for the fit of the pp plus np data up to 190 MeV and two- and three-nucleon bound-state properties as produced by NN potentials at NNLO and N^{4}LO applying different values for the cutoff parameter Λ of the regulator function Eq. (2.40). For some of the notation, see Table 6.5, where also empirical information on the deuteron and triton can be found.

	NNLO			N^{4}LO		
Λ(MeV)	450	500	550	450	500	550
χ^2/datum *pp* & *np*						
0–190 MeV (2903 data)	4.12	3.27	3.32	1.17	1.08	1.25
Deuteron						
B_d (MeV)	2.224575	2.224575	2.224575	2.224575	2.224575	2.224575
A_S (fm$^{-1/2}$)	0.8847	0.8844	0.8843	0.8852	0.8852	0.8851
η	0.0255	0.0257	0.0258	0.0254	0.0258	0.0257
$r_{\rm str}$ (fm)	1.967	1.968	1.968	1.966	1.973	1.971
Q (fm^2)	0.269	0.273	0.275	0.269	0.273	0.271
P_D (%)	3.95	4.49	4.87	4.38	4.10	4.13
Triton						
B_t (MeV)	8.35	8.21	8.10	8.04	8.08	8.12

steady convergence, order by order, towards a value around 8.1 MeV that is reached at the highest orders shown. This contribution from the 2NF will require only a moderate 3NF. The relatively low deuteron D-state probabilities ($\approx 4.1\%$ at N^{3}LO and N^{4}LO) and the concomitant generous triton binding energy predictions are a reflection of the fact that our NN potentials are soft (which is, at least in part, due to their non-local character).

6.6 Cutoff variations

As noted before, besides the case $\Lambda = 500$ MeV, we have also constructed potentials with $\Lambda = 450$ and 550 MeV at each order, to allow for systematic studies of the cutoff dependence. In Fig. 6.2, we display the variations of the np phase shifts for different cutoffs at NNLO (left half of figure, green curves) and at N^{4}LO (right half of figure, purple curves). We do not show the cutoff variations of phase shifts at N^{3}LO, because they are about the same as at N^{4}LO. Similarly, the variations at NLO are of about the same size as at NNLO. Fig. 6.2 demonstrates nicely how cutoff dependence diminishes with increasing order—a reasonable trend. Another point that is evident from this figure is that $\Lambda = 450$ MeV should be considered as a lower limit for cutoffs, because obviously cutoff artifacts start showing up—above 200 MeV, particularly, in $^1D_2$ and $^3D_2$. Concerning the upper limit for the cutoff: It has been discussed and demonstrated in length in the literature (see, e.g., Ref. [22]) that for the NN interaction the breakdown scale occurs around $\Lambda_b \approx 600$ MeV. The motivation for our upper value of 550 MeV is to stay below Λ_b.

In Table 6.6, we show the cutoff dependence for three selected aspects that are of great interest: the χ^2 for the fit of the NN data below 190 MeV, the deuteron properties, and the triton binding energy. The χ^2 does not change substantially as a function of cutoff, and crucial deuteron properties, like A_S and η, stay within the empirical range, for both NNLO and N^{4}LO. Thus, we can make the interesting observation that the reproduction of NN observables is not much affected by the cutoff variations. However, the D-state probability of the deuteron, P_D, which is not an observable, changes substantially as a function of cutoff at NNLO (namely, by $\approx 1\%$) while it changes only by 0.25% at N^{4}LO. Note that P_D is intimately related to the off-shell behavior of a potential and so are the binding energies of few-body systems. Therefore, in tune with the P_D variations, the binding energy of the triton varies by 0.25 MeV at NNLO, while it changes only by 0.08 MeV at N^{4}LO.

Even though cutoff variations are, in general, not the most reliable way to estimate truncation errors, in the above case they seem to reflect closely what we expect to be the truncation error.

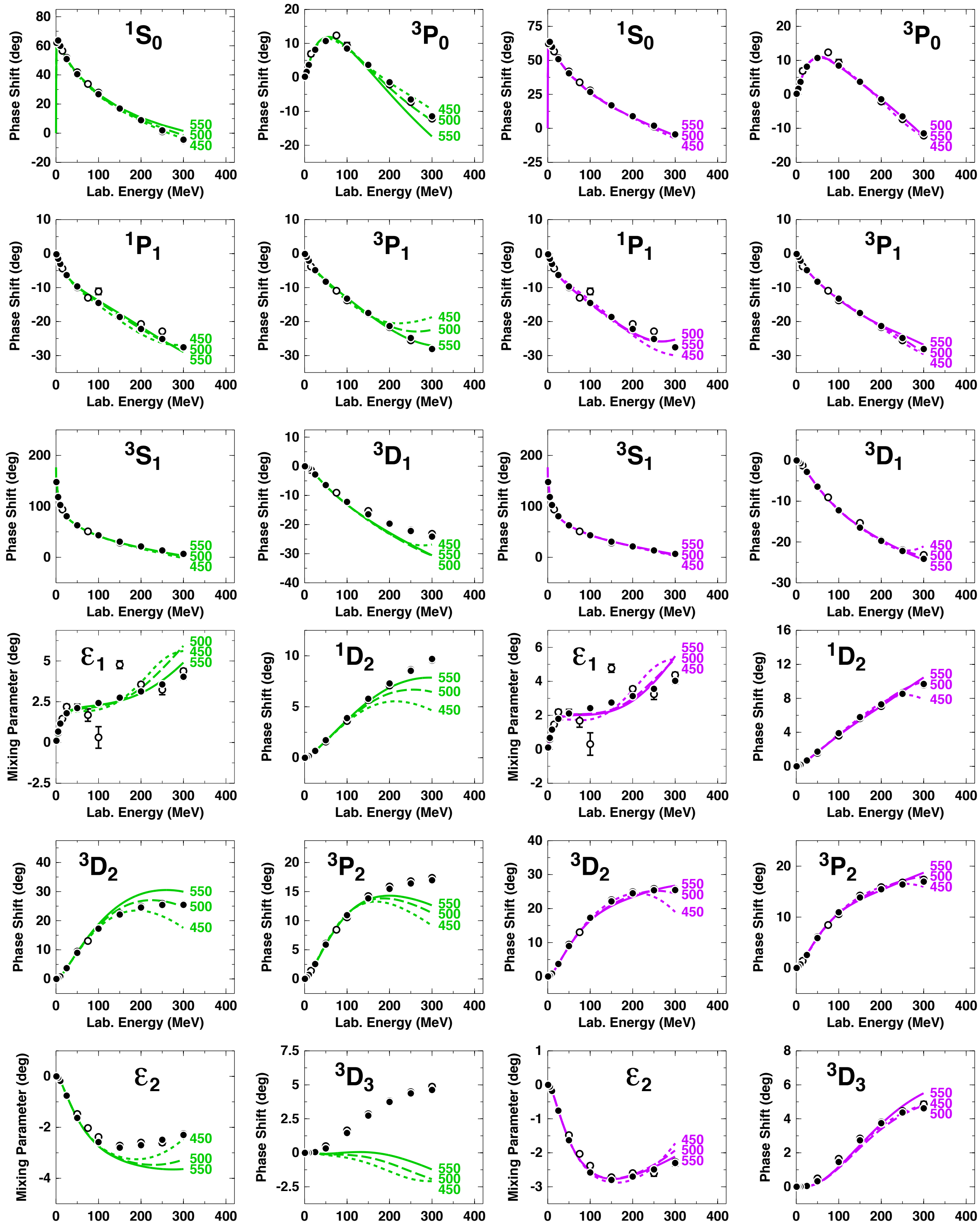

Figure 6.2: (Color online). Cutoff variations of the np phase shifts at NNLO (left side, green lines) and N^{4}LO (right side, purple lines). Dotted, dashed, and solid lines represent the results obtained with cutoff parameter Λ = 450, 500, and 550 MeV, respectively, as also indicated by the curve labels. Note that, at N^{4}LO, the cases 500 and 550 MeV cannot be distinguished on the scale of the figures for most partial waves. Filled and open circles as in Fig. 6.1.

CHAPTER 7
Conclusions

In the following sections, I once again summarize the important results derived in this study.

7.1 Pion exchange contributions at N4LO

We have calculated the one- and two-loop 2π-exchange (2PE) and two-loop 3π-exchange (3PE) contributions to the NN interaction which occur at N^{4}LO (fifth order) of the chiral low-momentum expansion. The calculations are based upon heavy-baryon chiral perturbation theory using the most general fourth order Lagrangian for pions and nucleons. We apply πN LECs, which were determined in an analysis of elastic pion-nucleon scattering to fourth order using the same power counting scheme as in the present work. The spectral functions, which determine the NN amplitudes via dispersion integrals, are regularized by a cutoff $\tilde{\Lambda}$ in the range 0.7 to 1.5 GeV (also known as spectral-function regularization). Besides the cutoff $\tilde{\Lambda}$, our calculations do not involve any adjustable parameters.

From past work on NN scattering in chiral perturbation theory (see, e.g., Ref. [15]), it is well-known that, at NNLO and N^{3}LO, chiral 2PE produces far too much attraction. The important result of this study is that the N^{4}LO 2PE contributions are prevailingly repulsive and, thus, compensate the excessive attraction of the lower orders. As a consequence, the phase-shift predictions in F and G waves are in very good agreement with the data, with the only exception of the $^1F_3$ wave. The net 3PE contribution turns out to be moderate pointing towards convergence in terms of the number of pions exchanged between two nucleons. On the other hand, the NNLO, N^{3}LO, and N^{4}LO contributions are all about of the same magnitude. This raises some questions about the convergence of the chiral expansion of the NN amplitude. Which is the reason why the N^{5}LO pion-exchange contributions were calculated as well.

7.2 Pion exchange contributions at N5LO

Dominant N^{5}LO 2π- and 3π-exchange contributions to the NN-interaction were calculated within the same framework as mentioned in previous section.

The spectral functions, which determine the NN-amplitudes via subtracted dispersion integrals, are regularized by a cutoff $\tilde{\Lambda}$ in the range 0.7 to 0.9 GeV. Again, besides the cutoff $\tilde{\Lambda}$, our calculations do not involve any adjustable parameters.

Our calculations show that the contribution at N^{5}LO is substantially smaller than the one at N^{4}LO, thus, indicating a signature of convergence. The two-loop 2π-exchange contribution is the largest, while the corresponding three-loop contribution is small, but not negligible. Three-pion exchange is generally small at this order. The phase-shift predictions in G and H waves, where only the non-polynomial terms governed by chiral symmetry contribute, are in excellent agreement with the data.

The smallness of N^{5}LO corrections compared to N^{4}LO as well as good agreement of N^{4}LO with experiment indicates that practical full NN potential needs to be calculated only up to 5th order (N^{4}LO)

7.3 Full NN potential at N4LO

We have constructed chiral NN potentials through five orders of chiral EFT ranging from LO to N^{4}LO. The construction may be perceived as consistent, because the same power counting scheme as well as the same cutoff procedures are applied in all orders. Moreover, the long-range part of these potentials are fixed by the very accurate πN LECs as determined in the Roy-Steiner equations analysis of Ref. [44]. In fact, the uncertainties of these LECs are so small that a variation within the errors leads to effects that are completely negligible at the current level of precision. Another aspect that has to do with precision is that, at least at the highest order (N^{4}LO), the NN data below pion-production threshold are reproduced with the outstanding χ^2/datum of 1.15. This is the highest precision ever accomplished with any chiral NN potential to date.

The NN potentials presented in this study may serve as a solid basis for systematic *ab initio* calculations of nuclear structure and reactions that allow for a comprehensive error analysis. In particular, the consistent order by order development of the potentials will make possible a reliable determination of the truncation error at each order.

Our family of potentials is non-local and, generally, of soft character. This feature is reflected in the fact that the predictions for the triton binding energy (from two-body forces only) converges to about 8.1 MeV at the highest orders. This leaves room for moderate three-nucleon forces.

These features of our potentials are in contrast to other families of chiral NN potentials of local or semi-local character that have recently enter the market [19, 20, 21, 22, 23]. Such potentials are less soft and, consequently, require stronger three-body force contributions.

The availability of families of chiral NN potentials of different character offers the opportunity for interesting systematic studies that may ultimately shed light on issues, like, the “radius problem" [35], the overbinding of intermediate-mass nuclei [36], and others.

Note that the differences between the above-mentioned families of potentials are in the off-shell character, which is not an observable. Thus, any off-shell behavior of a NN potential is legitimate. There is no wrong off-shell character. However, some off-shell behaviors may lead in a more efficient way to realistic results than others. That is of interest to the many-body practitioner. We are now in a position to systematically investigate this issue for chiral forces.

[1] R. Machleidt and D. R. Entem, Phys. Rep. **503**, 1 (2011).

[2] E. Epelbaum, H.-W. Hammer, and U.-G. Meißner, Rev. Mod. Phys. **81**, 1773 (2009).

[3] J. Gasser and H. Leutwyler, Ann. Phys. (N.Y.) **158**, 142 (1984).

[4] J. Gasser, M. E. Sainio, and A. Švarc, Nucl. Phys. **B307**, 779 (1988).

[5] S. Weinberg, Phys. Lett **B251**, 288 (1990); Nucl. Phys. **B363**, 3 (1991).

[6] C. Ordóñez, L. Ray, and U. van Kolck, Phys. Rev. Lett. **72**, 1982 (1994); Phys. Rev. C **53**, 2086 (1996).

[7] N. Kaiser, R. Brockmann, and W. Weise, Nucl. Phys. **A625**, 758 (1997).

[8] N. Kaiser, S. Gerstendörfer, and W. Weise, Nucl. Phys. **A637**, 395 (1998).

[9] N. Kaiser, Phys. Rev. C **61**, 014003 (2000).

[10] N. Kaiser, Phys. Rev. C **62**, 024001 (2000).

[11] N. Kaiser, Phys. Rev. C **63**, 044010 (2001).

[12] N. Kaiser, Phys. Rev. C **64**, 057001 (2001).

[13] N. Kaiser, Phys. Rev. C **65**, 017001 (2002).

[14] E. Epelbaum, W. Glöckle, and U.-G. Meißner, Nucl. Phys. **A637**, 107 (1998); **A671**, 295 (2000).

[15] D. R. Entem and R. Machleidt, Phys. Rev. C **66**, 014002 (2002).

[16] D. R. Entem and R. Machleidt, Phys. Rev. C **68**, 041001 (2003).

[17] E. Epelbaum, W. Glöckle, and U.-G. Meißner, Nucl. Phys. **A747**, 362 (2005).

[18] A. Ekstrőm, G. Baardsen, C. Forssen, G. Hagen, M. Hjorth-Jensen, G. R. Jansen, R. Machleidt, W. Nazarewicz, T. Papenbrock, J. Sarich, and S. M. Wild, Phys. Rev. Lett. **110**, 192502 (2013).

[19] A. Gezerlis, I. Tews, E. Epelbaum, M. Freunek, S. Gandolfi, K. Hebeler, A. Nogga, and A. Schwenk, Phys. Rev. C **90**, 054323 (2014).

[20] M. Piarulli, L. Girlanda, R. Schiavilla, R. Navarro Perez, J. E. Amaro and E. Ruiz Arriola, Phys. Rev. C **91**, 024003 (2015).

[21] M. Piarulli, L. Girlanda, R. Schiavilla, A. Kievsky, A. Lovato, L. E. Marcucci, Steven C. Pieper, M. Viviani, and R. B. Wiringa, Phys. Rev. C **94**, 054007 (2016).

[22] E. Epelbaum, H. Krebs, and Ulf-G. Meißner, Eur. Phys. J. A **51**, 53 (2015).

[23] E. Epelbaum, H. Krebs, and Ulf-G. Meißner, Phys. Rev. Lett. **115**, 122301 (2015).

[24] R. Navarro Pérez, J. E. Amaro, and E. Ruiz Arriola, Phys. Rev. C **91**, 054002 (2015), and more references to the *comprehensive* work by the Granada group therein.

[25] A. Ekstrőm *et al.*, Phys. Rev. C **91**, 051301 (2015).

[26] B. D. Carlsson *et al.*, Phys. Rev. X **6**, 011019 (2016).

[27] D. R. Entem, R. Machleidt, and H. Witala, Phys. Rev. C **65**, 064005 (2002).

[28] E. Epelbaum, A. Nogga, W. Gloeckle, H. Kamada, U. G. Meissner, and H. Witala, Phys. Rev. C **66**, 064001 (2002).

[29] M. Viviani, L. Girlanda, A. Kievsky, and L. E. Marcucci, Phys. Rev. Lett. **111**, 172302 (2013).

[30] J. Golak *et al.*, arXiv:1410.0756 [nucl-th].

[31] H. Krebs, A. Gasparyan, and E. Epelbaum, Phys. Rev. C **85**, 054006 (2012). We thank H. Krebs for pointing out and clarifying misprints in this paper.

[32] H. Krebs, A. Gasparyan, and E. Epelbaum, Phys. Rev. C **87**, 054007 (2013).

[33] E. Epelbaum, A. M. Gasparyan, H. Krebs, and C. Schat, Eur. Phys. J. A **51**, 26 (2015).

[34] L. Girlanda, A. Kievsky, M. Viviani, Phys. Rev. C **84**, 014001 (2011).

[35] V. Lapoux, V. Somà, C. Barbieri, H. Hergert, J. D. Holt, and S. R. Stroberg, Phys. Rev. Lett. **117**, 052501 (2016).

[36] S. Binder, J. Langhammer, A. Calci, and R. Roth, Phys. Lett. B **736**, 119 (2014).

[37] D. R. Entem, N. Kaiser, R. Machleidt, and Y. Nosyk, Phys. Rev. C **91**, 014002 (2015).

[38] D. R. Entem, R. Machleidt, Y. Nosyk, arXiv:1703.05454v1 [nucl-th].

[39] D. R. Entem, N. Kaiser, R. Machleidt, and Y. Nosyk, Phys. Rev. C **92**, 064001 (2015).

[40] S. Weinberg, Physica **96A**, 327 (1979)

[41] G. Q. Li and R. Machleidt, Phys. Rev. C **58** (1998) 3153.

[42] E. Epelbaum, W. Glöckle, and U.-G. Meißner, Eur. Phys. J. A **19**, 125 (2004).

[43] K. A. Olive *et al.* (Particle Data Group), Chin. Phys. C **38**, 090001 (2014).

[44] M. Hoferichter, J. Ruiz de Elvira, B. Kubis, and U.-G. Meißner, Phys. Rev. Lett. **115**, 192301 (2015); Phys. Rep. **625**, 1 (2016).

[45] G. J. M. Austin and J. J. de Swart, Phys. Rev. Lett. **50**, 2039 (1983).

[46] J. R. Bergervoet, P. C. van Campen, W. A. van der Sanden, and J. J. de Swart, Phys. Rev. C **38**, 15 (1988).

[47] U. van Kolck, M. C. M. Rentmeester, J. L. Friar, T. Goldman, and J. J. de Swart, Phys. Rev. Lett. **80**, 4386 (1998).

[48] R. Blankenbecler and R. Sugar, Phys. Rev. **142**, 1051 (1966).

[49] R. Machleidt, Phys. Rev. C **63** 024001 (2001).

[50] K. Erkelenz, R. Alzetta, and K. Holinde, Nucl. Phys. **A176**, 413 (1971); note that there is an error in equation (4.22) of this paper where it should read

$$^{-}W^{J}_{LS} = 2qq' \, \frac{J-1}{2J-1} \left[A^{J-2,(0)}_{LS} - A^{J(0)}_{LS} \right]$$

and

$$^{+}W^{J}_{LS} = 2qq' \, \frac{J+2}{2J+3} \left[A^{J+2,(0)}_{LS} - A^{J(0)}_{LS} \right] .$$

[51] R. Machleidt, in: *Computational Nuclear Physics 2 – Nuclear Reactions*, edited by K. Langanke, J.A. Maruhn, and S.E. Koonin (Springer, New York, 1993) p. 1.

[52] G. P. Lepage, *How to Renormalize the Schrödinger Equation*, arXiv:nucl-th/9706029.

[53] E. Marji *et al.*, Phys. Rev. C **88**, 054002 (2013).

[54] H. P. Stapp, T. J. Ypsilantis, and N. Metropolis, Phys. Rev. **105**, 302 (1957).

[55] R. A. Arndt, W. J. Briscoe, I. I. Strakovsky, and R. L. Workman, Phys. Rev. C **74**, 045205 (2006).

[56] R. Koch, Nucl. Phys. A **448**, 707 (1986).

[57] K. A. Wendt, B. D. Carlsson, and A. Ekstrőm, "Uncertainty Quantification of the Pion-Nucleon Low-Energy Coupling Constants up to Fourth Order in Chiral Perturbation Theory," arXiv:1410.0646 [nucl-th].

[58] V. G. J. Stoks, R. A. M. Klomp, M. C. M. Rentmeester, and J. J. de Swart, Phys. Rev. C **48**, 792 (1993).

[59] R. A. Arndt, I. I. Strakovsky, and R. L. Workman, SAID, Scattering Analysis Interactive Dial-in computer facility, George Washington University (formerly Virginia Polytechnic Institute), solution SM99 (Summer 1999); for more information see, e. g., R. A. Arndt, I. I. Strakovsky, and R. L. Workman, Phys. Rev. C **50**, 2731 (1994).

[60] A. D. Jackson, D. O. Riska, and B. Verwest, Nucl. Phys. **A249**, 397 (1975).

[61] G. E. Brown and A. D. Jackson, *The Nucleon-Nucleon Interaction* (North-Holland, Amsterdam, 1976).

[62] R. Vinh Mau, in: *Mesons in Nuclei*, Vol. I, edited by M. Rho and D. H. Wilkinson (North-Holland, Amsterdam, 1979), p. 151.

[63] M. Lacombe, B. Loiseau, J. M. Richard, R. Vinh Mau, J. Côté, P. Pires, and R. de Tourreil, Phys. Rev. C **21**, 861 (1980).

[64] W. J. Briscoe, I. I. Strakovsky, and R. L. Workman, SAID Partial-Wave Analysis Facility, Data Analysis Center, The George Washington University, solution SP07 (Spring 2007).

[65] R. Navarro Perez, J. E. Amaro and E. Ruiz Arriola, Phys. Rev. C **88**, 064002 (2013).

[66] R. Machleidt, K. Holinde, and Ch. Elster, Phys. Rep. **149** (1987) 1.

[67] J. R. Bergervoet, P. C. van Campen, R. A. M. Klomp, J.-L. de Kok, T. A. Rijken, V. G. J. Stoks, and J. J. de Swart, Phys. Rev. C **41**, 1435 (1990).

[68] D. Albers *et al.*, Eur. Phys. J. A **22**, 125 (2004).

[69] N. Hoshizaki, Prog. Theor. Phys. Suppl. **42**, 107 (1968).

[70] J. Bystricky, F. Lehar, and P. Winterschnitz, J. Phys. (Paris) **39**, 1 (1978).

[71] W. P. Abfalterer, F. B. Bateman, F. S. Dietrich, R. W. Finlay, R. C. Haight, and G. L. Morgan, Phys. Rev. C **63**, 044608 (2001).

[72] N. Boukharouba, F. B. Bateman, C. E. Brient, A. D. Carlson, S. M. Grimes, R. C. Haight, T. N. Massey, and O. A. Wasson, Phys. Rev. C **65**, 014004 (2002).

[73] P. Mermod *et al.*, Phys. Lett. B **597**, 243 (2004).

[74] P. Mermod *et al.*, Phys. Rev. C **72**, 061002 (2005).

[75] J. Klug *et al.*, Nucl. Instrum. Methods A **489**, 282 (2002).

[76] V. Blideanu *et al.*, Phys. Rev. C **70**, 014607 (2004).

[77] C. Johansson *et al.*, Phys. Rev. C **71**, 024002 (2005).

[78] J. Arnold *et al.*, Eur. Phys. J. C **17**, 67 (2000).

[79] J. Arnold *et al.*, Eur. Phys. J. C **17**, 83 (2000).

[80] M. Daum *et al.*, Eur. Phys. J. C **25**, 55 (2002).

[81] F. Gross and A. Stadler, Phys. Rev. C **78**, 014005 (2008).

[82] W. A. van der Sanden, A. H. Emmen, and J. J. de Swart, Report No. THEF-NYM-83.11, Nijmegen (1983), unpublished; quoted in Ref. [46].

[83] D. E. González Trotter *et al.*, Phys. Rev. C **73**, 034001 (2006).

[84] Q. Chen *et al.*, Phys. Rev. C **77**, 054002 (2008).

[85] G. A. Miller, M. K. Nefkens, and I. Slaus, Phys. Rep. **194**, 1 (1990).

[86] U. D. Jentschura, A. Matveev, C. G. Parthey, J. Alnis, R. Pohl, Th. Udem, N. Kolachevsky, and T. W. Hänsch, Phys. Rev. A **83**, 042505 (2011).

[87] V. Stoks and J. J. de Swart, Phys. Rev. C **47**, 761 (1993).

[88] K. Levenberg, Quarterly of Applied Mathematics. **2**, 164 (1944)

[89] D. Marquardt, SIAM Journal on Applied Mathematics. **11**(2), 431 (1963)

[90] J. Nelder, R. Mead, Computer Journal. **7**, 308 (1965)

[91] V. G. J. Stoks (private communication).

APPENDIX A

Pion exchange contributions up to N3LO

A.1 Leading order (LO)

At leading order, there is only the 1π-exchange contribution, cf. Fig. A.1. The charge-independent 1π-exchange is given by

$$V_{1\pi}^{(\mathrm{CI})}(\vec{p}\,',\vec{p}) = -\frac{g_A^2}{4f_\pi^2}\,\boldsymbol{\tau}_1\cdot\boldsymbol{\tau}_2\,\frac{\vec{\sigma}_1\cdot\vec{q}\,\vec{\sigma}_2\cdot\vec{q}}{q^2+m_\pi^2}\,. \tag{A.1}$$

Higher order corrections to the 1π-exchange are taken care of by mass and coupling constant renormalizations $g_A/f_\pi \to g_{\pi N}/M_N$. Note also that, on shell, there are no relativistic corrections. Thus, we apply 1π-exchange in the form Eq. (A.1) through all orders.

In this paper, we are specifically calculating neutron-proton (np) scattering and take the charge-dependence of the 1π-exchange into account. Thus, in proton-proton (pp) and neutron-neutron (nn) scattering, we use

$$V_{1\pi}^{(pp)}(\vec{p}\,',\vec{p}) = V_{1\pi}^{(nn)}(\vec{p}\,',\vec{p}) = V_{1\pi}(m_{\pi^0})\,, \tag{A.2}$$

and in neutron-proton (np) scattering, we apply

$$V_{1\pi}^{(np)}(\vec{p}\,',\vec{p}) = -V_{1\pi}(m_{\pi^0}) + (-1)^{I+1}\,2\,V_{1\pi}(m_{\pi^\pm})\,, \tag{A.3}$$

where $I=0,1$ denotes the total isospin of the two-nucleon system and

$$V_{1\pi}(m_\pi) \equiv -\frac{g_A^2}{4f_\pi^2}\,\frac{\vec{\sigma}_1\cdot\vec{q}\,\vec{\sigma}_2\cdot\vec{q}}{q^2+m_\pi^2}\,. \tag{A.4}$$

We use $m_{\pi^0} = 134.9766$ MeV and $m_{\pi^\pm} = 139.5702$ MeV. Formally speaking, the charge-dependence of the 1PE exchange is of order NLO [1], but we include it already at leading order to make the comparison with the np phase shifts more meaningful.

A.2 Next-to-leading order (NLO)

The NN diagrams that occur at NLO (cf. Fig. A.1) contribute in the following way [7]:

$$\begin{aligned} W_C &= \frac{L(\tilde{\Lambda};q)}{384\pi^2 f_\pi^4}\left[4m_\pi^2(1+4g_A^2-5g_A^4)+q^2(1+10g_A^2-23g_A^4)-\frac{48g_A^4m_\pi^4}{w^2}\right]\,, && \text{(A.5)}\\ V_T &= -\frac{1}{q^2}V_S \;=\; -\frac{3g_A^4}{64\pi^2 f_\pi^4}L(\tilde{\Lambda};q)\,. && \text{(A.6)} \end{aligned}$$

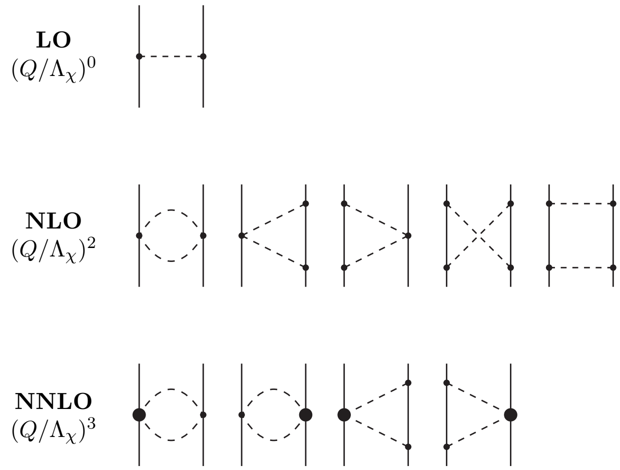

Figure A.1: LO, NLO, and NNLO contributions to the NN interaction. Notation as in Fig. 3.1.

A.3 Next-to-next-to-leading order (NNLO)

The NNLO contribution (lower row of Fig. A.1) is given by [7]:

$$V_C = \frac{3g_A^2}{16\pi f_\pi^4}\left[2m_\pi^2(c_3-2c_1)+c_3q^2\right](2m_\pi^2+q^2)A(\tilde{\Lambda};q)\,, \tag{A.7}$$

$$W_T = -\frac{1}{q^2}W_S = -\frac{g_A^2}{32\pi f_\pi^4}c_4 w^2 A(\tilde{\Lambda};q)\,. \tag{A.8}$$

The loop function that appears in the above expressions, regularized by spectral-function cut-off $\tilde{\Lambda}$, is

$$A(\tilde{\Lambda};q) = \frac{1}{2q}\arctan\frac{q(\tilde{\Lambda}-2m_\pi)}{q^2+2\tilde{\Lambda}m_\pi}\,. \tag{A.9}$$

Note that

$$\lim_{\tilde{\Lambda}\to\infty} A(\tilde{\Lambda};q) = \frac{1}{2q}\arctan\frac{q}{2m_\pi} \tag{A.10}$$

yields the loop function used in dimensional regularization.

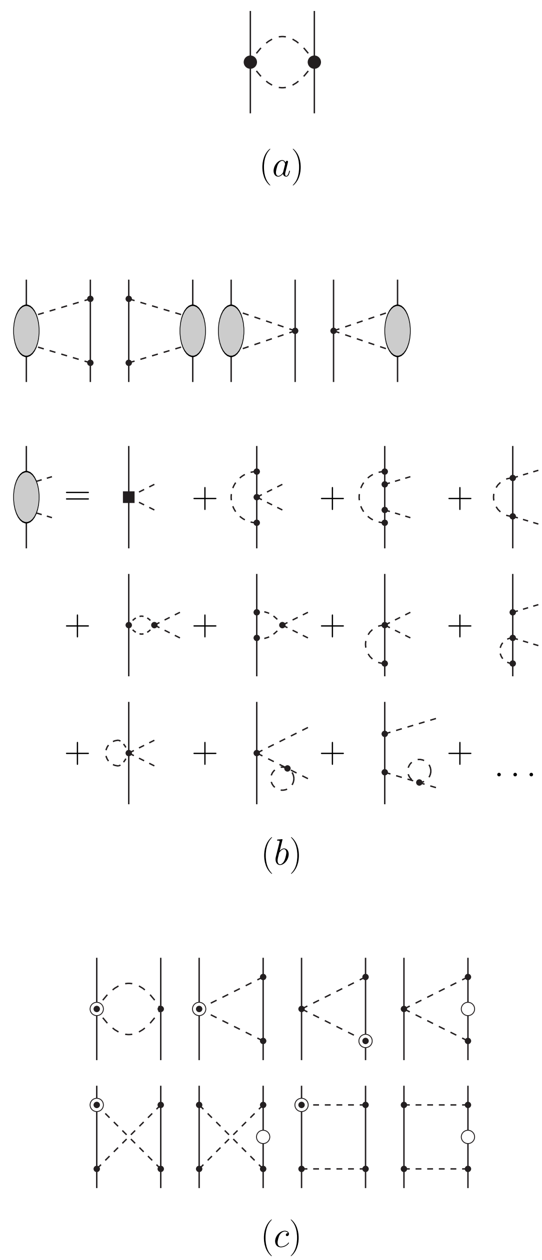

Figure A.2: Two-pion exchange contributions at N^{3}LO with (a) the N^{3}LO football diagram, (b) the leading 2PE two-loop contributions, and (c) the relativistic corrections of NLO diagrams. Notation as in Fig. 3.1.

A.4 Next-to-next-to-next-to-leading order (N3LO)

A.4.1 Football diagram at N3LO

The football diagram at N^{3}LO, Fig. A.2(a), generates [12]:

$$V_C = \frac{3}{16\pi^2 f_\pi^4}\left[\left(\frac{c_2}{6}w^2 + c_3(2m_\pi^2+q^2) - 4c_1 m_\pi^2\right)^2 + \frac{c_2^2}{45}w^4\right] L(\tilde{\Lambda};q)\,, \tag{A.11}$$

$$W_T = -\frac{1}{q^2}W_S = \frac{c_4^2}{96\pi^2 f_\pi^4} w^2 L(\tilde{\Lambda};q)\,. \tag{A.12}$$

A.4.2 Leading two-loop contributions

The leading order 2π-exchange two-loop diagrams are shown in Fig. A.2(b). In terms of spectral functions, the results are [12]:

$$\begin{aligned}
\mathrm{Im}\,V_C &= \frac{3g_A^4(2m_\pi^2-\mu^2)}{\pi\mu(4f_\pi)^6}\Big[(m_\pi^2-2\mu^2)\left(2m_\pi + \frac{2m_\pi^2-\mu^2}{2\mu}\ln\frac{\mu+2m_\pi}{\mu-2m_\pi}\right) \\
&\quad +4g_A^2 m_\pi(2m_\pi^2-\mu^2)\Big]\,, && \text{(A.13)}\\
\mathrm{Im}\,W_C &= \frac{2\kappa}{3\mu(8\pi f_\pi^2)^3}\int_0^1 dx\left[g_A^2(\mu^2-2m_\pi^2)+2(1-g_A^2)\kappa^2x^2\right] \\
&\quad \times\Bigg\{96\pi^2 f_\pi^2\left[(2m_\pi^2-\mu^2)(\bar{d}_1+\bar{d}_2)-2\kappa^2x^2\bar{d}_3+4m_\pi^2\bar{d}_5\right] \\
&\quad + \left[4m_\pi^2(1+2g_A^2)-\mu^2(1+5g_A^2)\right]\frac{\kappa}{\mu}\ln\frac{\mu+2\kappa}{2m_\pi} + \frac{\mu^2}{12}(5+13g_A^2)-2m_\pi^2(1+2g_A^2) \\
&\quad - 3\kappa^2x^2 + 6\kappa x\sqrt{m_\pi^2+\kappa^2x^2}\ln\frac{\kappa x+\sqrt{m_\pi^2+\kappa^2x^2}}{m_\pi} \\
&\quad + g_A^4\left(\mu^2-2\kappa^2x^2-2m_\pi^2\right) \\
&\quad \times\left[\frac{5}{6}+\frac{m_\pi^2}{\kappa^2x^2}-\left(1+\frac{m_\pi^2}{\kappa^2x^2}\right)^{3/2}\ln\frac{\kappa x+\sqrt{m_\pi^2+\kappa^2x^2}}{m_\pi}\right]\Bigg\}\,, && \text{(A.14)}\\
\mathrm{Im}\,V_S &= \mu^2\,\mathrm{Im}\,V_T = \frac{g_A^2\mu\kappa^3}{8\pi f_\pi^4}\left(\bar{d}_{15}-\bar{d}_{14}\right) + \frac{2g_A^6\mu\kappa^3}{(8\pi f_\pi^2)^3} \\
&\quad \times\int_0^1 dx(1-x^2)\left[\frac{1}{6}-\frac{m_\pi^2}{\kappa^2x^2}+\left(1+\frac{m_\pi^2}{\kappa^2x^2}\right)^{3/2}\ln\frac{\kappa x+\sqrt{m_\pi^2+\kappa^2x^2}}{m_\pi}\right]\,, && \text{(A.15)}\\
\mathrm{Im}\,W_S &= \mu^2\,\mathrm{Im}\,W_T(i\mu) = \frac{g_A^4(4m_\pi^2-\mu^2)}{\pi(4f_\pi)^6}\left[\left(m_\pi^2-\frac{\mu^2}{4}\right)\ln\frac{\mu+2m_\pi}{\mu-2m_\pi}+(1+2g_A^2)\mu m_\pi\right] && \text{(A.16)}
\end{aligned}$$

where $\kappa = \sqrt{\mu^2/4 - m_\pi^2}$.

The momentum space amplitudes $V_\alpha(q)$ and $W_\alpha(q)$ are obtained from the above expressions by means of the dispersion integrals shown in Eq. (2.18).

A.4.3 Leading relativistic corrections

The relativistic corrections of the NLO diagrams, which are shown in Fig. A.2(c), count as N^{3}LO and are given by [1]:

$$sV_C = \frac{3g_A^4}{128\pi f_\pi^4 M_N}\left[\frac{m_\pi^5}{2w^2} + (2m_\pi^2 + q^2)(q^2 - m_\pi^2)A(\tilde{\Lambda}; q)\right], \tag{A.17}$$

$$W_C = \frac{g_A^2}{64\pi f_\pi^4 M_N}\left\{\frac{3g_A^2 m_\pi^5}{2\omega^2} + \left[g_A^2(3m_\pi^2 + 2q^2) - 2m_\pi^2 - q^2\right](2m_\pi^2 + q^2)A(\tilde{\Lambda}; q)\right\}, \tag{A.18}$$

$$V_T = -\frac{1}{q^2}V_S = \frac{3g_A^4}{256\pi f_\pi^4 M_N}(5m_\pi^2 + 2q^2)A(\tilde{\Lambda}; q)\,, \tag{A.19}$$

$$W_T = -\frac{1}{q^2}W_S = \frac{g_A^2}{128\pi f_\pi^4 M_N}\left[g_A^2(3m_\pi^2 + q^2) - w^2\right]A(\tilde{\Lambda}; q)\,, \tag{A.20}$$

$$V_{LS} = \frac{3g_A^4}{32\pi f_\pi^4 M_N}\,(2m_\pi^2 + q^2)A(\tilde{\Lambda}; q)\,, \tag{A.21}$$

$$W_{LS} = \frac{g_A^2(1 - g_A^2)}{32\pi f_\pi^4 M_N}\,w^2 A(\tilde{\Lambda}; q)\,. \tag{A.22}$$

A.4.4 Leading three-pion exchange contributions

The leading 3π-exchange contributions that occur at N^{3}LO have been calculated in Refs. [9, 10] and are found to be negligible. We, therefore, omit them.

APPENDIX B

Phaseshift tables for full NN potential at N4LO

In this appendix, we show the phase shifts as predicted by the N^{4}LO potential with $\Lambda = 500$ MeV. Note that our *pp* phase shifts are the phase shifts of the nuclear plus relativistic Coulomb interaction with respect to Coulomb wave functions. For *nn* and *np* scattering, our phase shifts are the ones from the nuclear interaction with respect to Riccati-Bessel functions. For more technical details of our phase shift calculations, we refer the interested reader to the appendix A3 of Ref. [49].

Table B.1: *pp* phase shifts (in degrees) up to F-waves at N^{4}LO ($\Lambda = 500$ MeV).

$T_{\rm lab}$ (MeV)	$^1S_0$	$^3P_0$	$^3P_1$	$^1D_2$	$^3P_2$	$^3F_2$	ϵ_2	$^3F_3$	$^3F_4$
1	32.79	0.14	-0.08	0.00	0.01	0.00	0.00	0.00	0.00
5	54.84	1.61	-0.89	0.04	0.23	0.00	-0.05	0.00	0.00
10	55.20	3.79	-2.02	0.17	0.69	0.01	-0.20	-0.03	0.00
25	48.62	8.66	-4.84	0.69	2.57	0.11	-0.81	-0.23	0.02
50	38.84	11.42	-8.26	1.67	5.87	0.35	-1.69	-0.68	0.12
100	24.97	9.15	-13.48	3.61	10.70	0.83	-2.62	-1.46	0.51
150	15.04	4.55	-17.72	5.45	13.57	1.16	-2.83	-1.98	1.07
200	7.10	-0.47	-21.39	7.22	15.54	1.20	-2.71	-2.31	1.67
250	0.11	-5.89	-25.12	8.85	17.01	0.92	-2.42	-2.48	2.20
300	-6.43	-11.40	-29.35	9.91	17.84	0.35	-1.99	-2.46	2.59

Table B.2: nn phase shifts (in degrees) up to F-waves at N^{4}LO ($\Lambda = 500$ MeV).

T_{lab} (MeV)	$^1S_0$	$^3P_0$	$^3P_1$	$^1D_2$	$^3P_2$	$^3F_2$	ϵ_2	$^3F_3$	$^3F_4$
1	57.62	0.21	-0.12	0.00	0.02	0.00	0.00	0.00	0.00
5	61.01	1.88	-1.03	0.05	0.28	0.00	-0.06	-0.01	0.00
10	57.82	4.16	-2.21	0.18	0.78	0.01	-0.22	-0.04	0.00
25	49.11	9.01	-5.08	0.73	2.77	0.11	-0.84	-0.24	0.02
50	38.71	11.55	-8.52	1.72	6.15	0.36	-1.72	-0.70	0.13
100	24.65	9.06	-13.76	3.68	11.02	0.84	-2.62	-1.48	0.53
150	14.70	4.40	-17.98	5.52	13.92	1.16	-2.82	-2.00	1.09
200	6.74	-0.63	-21.62	7.28	15.94	1.20	-2.68	-2.32	1.70
250	-0.28	-6.02	-25.32	8.88	17.42	0.91	-2.36	-2.49	2.23
300	-6.87	-11.40	-29.48	9.87	18.24	0.32	-1.93	-2.46	2.61

Table B.3: $I = 1$ np phase shifts (in degrees) up to F-waves at N^{4}LO ($\Lambda = 500$ MeV).

T_{lab} (MeV)	$^1S_0$	$^3P_0$	$^3P_1$	$^1D_2$	$^3P_2$	$^3F_2$	ϵ_2	$^3F_3$	$^3F_4$
1	62.00	0.18	-0.11	0.00	0.02	0.00	0.00	0.00	0.00
5	63.47	1.66	-0.92	0.04	0.27	0.00	-0.05	0.00	0.00
10	59.72	3.72	-2.03	0.16	0.75	0.01	-0.19	-0.03	0.00
25	50.48	8.25	-4.79	0.68	2.66	0.09	-0.76	-0.20	0.02
50	39.83	10.69	-8.20	1.68	5.96	0.31	-1.62	-0.61	0.11
100	25.68	8.25	-13.44	3.68	10.76	0.78	-2.53	-1.35	0.49
150	15.78	3.63	-17.67	5.56	13.63	1.08	-2.76	-1.86	1.04
200	7.90	-1.37	-21.33	7.34	15.63	1.12	-2.64	-2.18	1.64
250	0.96	-6.75	-25.05	8.96	17.12	0.83	-2.35	-2.35	2.17
300	-5.57	-12.14	-29.23	9.96	17.95	0.25	-1.93	-2.34	2.55

Table B.4: $I = 0$ np phase shifts (in degrees) at N^{4}LO ($\Lambda = 500$ MeV).

T_{lab} (MeV)	$^1P_1$	$^3S_1$	$^3D_1$	ϵ_1	$^3D_2$	$^1F_3$	$^3D_3$	$^3G_3$	ϵ_3
1	-0.19	147.75	-0.01	0.11	0.01	0.00	0.00	0.00	0.00
5	-1.50	118.17	-0.19	0.68	0.22	-0.01	0.00	0.00	0.01
10	-3.06	102.61	-0.69	1.17	0.85	-0.07	0.00	0.00	0.08
25	-6.32	80.66	-2.83	1.79	3.71	-0.42	0.02	-0.05	0.56
50	-9.66	62.91	-6.48	2.03	8.82	-1.13	0.20	-0.26	1.62
100	-14.78	43.72	-12.20	2.09	16.51	-2.19	1.10	-0.94	3.54
150	-19.52	31.42	-16.34	2.33	21.08	-2.92	2.29	-1.76	4.95
200	-23.46	21.60	-19.55	2.99	23.89	-3.54	3.40	-2.57	5.90
250	-25.72	12.68	-22.01	4.09	25.21	-4.14	4.23	-3.24	6.40
300	-25.27	4.02	-23.38	5.34	24.41	-4.69	4.78	-3.65	6.39